A Centrifuge Decelerator and a Thermometer for Cold Polar Molecules

Xing WU

Technische Universität München

Max-Planck-Institut für Quantenoptik

A Centrifuge Decelerator and a Thermometer for Cold Polar Molecules

Xing Wu

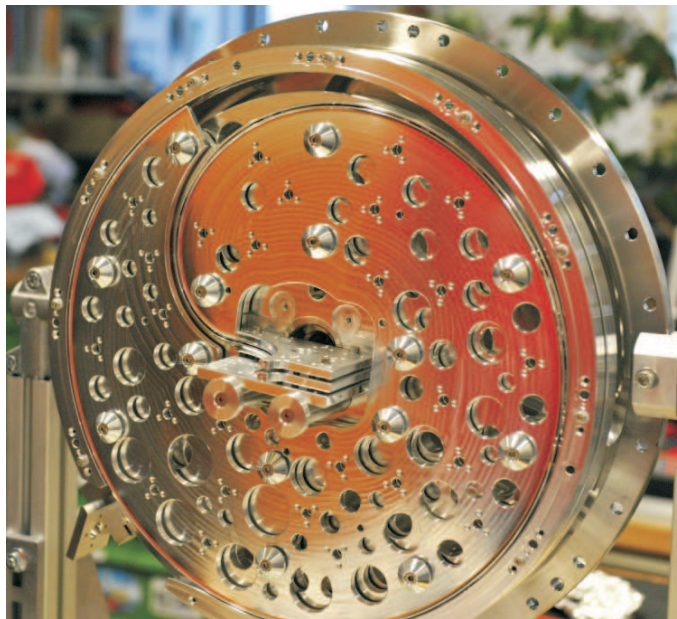Vollständiger Abdruck der von der Fakultät für Physik der Technischen Universität München zur Erlangung des akademischen Grades eines

Doktors der Naturwissenschaften (Dr. rer. nat.)

genehmigten Dissertation.

Vorsitzender :   Univ.-Prof. Dr. W. Zwerger

Prüfer der Dissertation : 1. Hon.-Prof. Dr. G. Rempe
                           2. Univ.-Prof. Dr. S. Paul

Die Dissertation wurde am 06.03.2017 bei der Technischen Universität München eingereicht und durch die Fakultät für Physik am 29.05.2017 angenommen.

Abstract

Molecules in the low temperature limit offer fascinating research perspectives in physics and chemistry, and molecule cooling and deceleration has developed into a research field of its own. The grand challenge today is to prepare dense samples with ample cold molecules.

Towards this end, we present an elegant solution to this problem by a non-conventional approach, employing the centrifugal force in a rotating frame to decelerate molecules to a standstill. The centrifuge deceleration is a generic method since its principle is not associated with any specific internal structure of the molecules. Moreover, electrostatic guiding of molecules is applied throughout the deceleration process, which enables for the first time the deceleration of continuous molecular beams to achieve unprecedented high fluxes of slow molecules. In a proof-of-principle experiment, we demonstrate fluxes of $\sim 10^9$ molecules/s and densities of $\sim 10^8$ molecules/cm^3 below $k_B \cdot 1\,\mathrm{K}$ in the laboratory frame, originated from a room-temperature effusive beam source. The efficiency of this decelerator is measured to be up to 20%, outperforming all the existing molecular deceleration methods. The generality of this method is demonstrated by the deceleration of several polyatomic molecular species, CH_3F, CF_3H, and CF_3CCH. In addition to presenting the basic principle and the results, we also describe thoroughly in this thesis the design of the centrifuge decelerator, optimized through Monte-Carlo trajectory simulations, and the technical assembly.

The second focus of this thesis is on the development and implementation of a simple and robust internal-state thermometry method for cold polyatomic molecules. The method is based on the combination of resonant radio-frequency depletion spectroscopy and Monte Carlo trajectory simulations. The radio-frequency depletion spectroscopy is capable of addressing 100% of the rotational states populated by the cold polyatomic molecules, as well as resolving their hyperfine states. With this tool, various aspects of cryogenic buffer-gas cooling used as a source of internally cold molecules are characterized. The properties of the cold molecular beams obtained at different buffer-gas temperature, densities, and cooling regimes, are analyzed. The cooling processes for different polyatomic molecules are compared. These studies reveal also two interesting phenomena in the buffer-gas cooling process. Firstly, evidence is provided that molecular rotational degrees of freedom can thermalize more efficiently than their translational ones. Secondly, the measurements provide indications for dependence of the collisional relaxation rate on the rotational states of the molecules.

Contents

Chapter 1

Introduction

Getting a deeper insight into various subtle properties of matter requires addressing its individual constituents and their individual quantum states. This can be achieved by reducing the temperature of the studied system. Microscopically, the degree to which a physical system is under control can be quantified by its entropy, $S = k_B \, ln\Omega$ where Ω is the number of relevant states. A reduction of entropy, hence a better control, is accompanied by the extraction of thermal energy from the system. Thermodynamically, this is described by $dS = \delta Q/T$ [1]. As a simple illustration, when a system is in its ground state, the change in entropy for an excitation to the next level, with equal probability of occupying both states, is associated with a thermal energy $k_B T \, ln2$. At a sufficiently low temperature, this amount of thermal energy can no longer compensate the energy spacing between the two levels, hence the system is frozen to its ground state.

Achieving lower temperatures has made tremendous impact on our understanding of various physical systems.

For individual particles, the decrease of thermal fluctuations enables both more precise observations of their structures and manipulation of their states. A temperature reduction in many organic molecules from $300\,\mathrm{K}$ to $10\,\mathrm{K}$ drastically simplifies their spectra and reveals their structures in detail [2]. In the ultracold regime, the atomic states can be controlled so precisely that it enables e.g. the non-destructive detection of an optical photon [3] with a single atom in an optical cavity.

For two-particle systems, the interactions are governed by quantum effects at low temperatures [4]. Collisions between two particles can be described by only one or a few partial wave components. Chemical reactions are usually dominated by the tunneling effect at the energy barrier. Moreover, various types of resonances in the collision or chemical reaction processes previously buried under thermal averaging can be resolved with well-controlled kinetic-energy states.

Also, for many-particle systems, their collective behaviors also exhibit unique phenomena at low temperatures. Spontaneous magnetization happens below the Curie temperature because the thermal fluctuation of a spin orientation can no longer overcome the interaction energy from all nearby spins. The other well-

known examples are the superconductivity, the superfluidity, and the Bose-Einstein-condensation. In all these three cases, the relevant 'particles' are cooled to a condensate in their motional ground state [5].

With this in mind, we would like to extend the study of cold and ultracold matter into the realm of polar molecules. Polar molecules differ from the well-studied cold atoms in several aspects, and bring forth a manifold of applications [6, 7]. First of all, their intrinsic electric dipole moment offers a long-ranged and anisotropic interaction which is either absent or is orders-of-magnitude weaker for ground-state atoms. Also, the uniqueness of possessing a rich structure including electronic, vibrational, rotational, and torsional[1] degrees of freedom, renders molecules an excellent platform for studying various problems, e.g., the chirality of matter [8], the proton-to-electron mass ratio [9], and the shape of electrons [10]. Moreover, many polar molecules carry great importance in the field of chemistry, biology, and astrophysics, which are simply unrivaled by the alkali, alkaline-earth, or several other rare-earth atoms that have been cooled to the ultracold regime. These will be discussed in detail in Section 1.1.

The advantage for molecules of having rich internal structures, however, comes with a price. It is hard to find a closed transition-cycle in a molecule, especially a polyatomic one, to implement laser cooling, which has been a workhorse for creating ultracold atoms [11]. Over the last one and a half decades, a handful of very diverse techniques have been invented to produce molecular ensembles at lower temperatures or smaller kinetic energy. An overview will be given in Section 1.2. These methods, however, generally have not produced cold molecules at a high density. In this thesis, a new method is demonstrated, which generates cold molecules at unprecedented rates, outperforming all existing methods by orders of magnitude. The structure of this thesis will be introduced in Section 1.3.

1.1 Application of cold molecules

1.1.1 Cold collisions and electric dipole interactions

Collisions and chemical reactions between molecules exhibit quantum properties at low temperatures. For example, methyl fluoride (CH_3F, $m = 34\,u$) at $1\,K$ temperature has a mean velocity of $22\,m/s$ and a de Broglie wave-length of $5\,Å$, which exceeds the size of the molecule (e.g. the F-H distance is only $2\,Å$). Thus, the chemical reaction in this case will be governed by the wave-like properties of the molecules. When the relative kinetic energy between two colliding partners is close to the magnitude of the potential barrier, quasi-bound states can form via tunneling. This introduces resonance structures in the scattering cross section. Loreau et al. [12] has predicted

_____

[1] resulting from the internal rotation of a function group within a molecule, e.g., the internal rotational of the -OH group with respect to the -CH_3 in methanol molecules.

shape resonances in ND_3-He and NH_3-He systems at collision energy in the range of $1\,K$ and $6\,K$.

Another implication of being cold is that the relative kinetic energy has a narrower distribution, which allows resolving these energy-dependent collision resonances. An elegant demonstration is the experimental observation of resonances in Penning ionization by Henson et al. [13]. In this experiment, several resonances in the $He^* + M \leftrightarrow He + M^+ + e^-$ reaction, where He^* is helium in the metastable $(2\,^3S)$ state and M is H_2 or Ar, have been resolved in the range from $10\,K$ to $10\,mK$.

The intrinsic electric dipole moment possessed by molecules also greatly enhances their interaction strength. The electric dipole interaction is three orders of magnitude stronger than the magnetic interactions. For molecules with a dipole moment $d \sim 1\,D$, the order of magnitude of the dipolar interaction length a towards the quantum limit can be approximated by equating the dipole interaction energy with the centrifugal energy [14], which gives $a \sim d^2 m/(4\pi\epsilon_0\hbar^2) \sim 10^{-6}\,m$. Such a huge interaction length opens up new possibilities in research [15].

1.1.2 High-precision measurements

High-precision spectroscopy not only reveals the structures of particles in great detail, but also turns into a sensitive ruler for verifying the tiny effects predicted by fundamental laws of physics. The rich internal structure of molecules provides great opportunities for such measurements.

One example is the search for the electron electric dipole moment (eEDM), d_e. A measurable eEDM requires a violation of the time reversal symmetry [16]. While the Standard Model of particle physics predicts a value of $< 10^{-38}$ e·cm for eEDM which is too small to be measured at the moment, various extensions to the Standard Model predict orders-of-magnitude higher values. For example, the supersymmetry model predicts an eEDM in the range of 10^{-27}-10^{-30} e·cm. Thus, a precise measurement of the value of eEDM provides a test for physics beyond the Standard Model.

The value of d_e can be measured via the energy shift $U = \vec{d_e} \cdot \vec{\mathcal{E}}$ where $\vec{\mathcal{E}}$ is the electric-field. Thus, molecules with internal effective $\vec{\mathcal{E}}$ up to a million times stronger than the static E-field achievable in any laboratory offer an ideal platform to probe d_e with extremely high sensitivity [16]. In addition, by choosing a particular molecular state, that is insensitive to the ambient noise, for the EDM measurement, it allows a suppression of systematic errors [17, 18]. A recent experiment with ThO molecules makes use of both advantages mentioned above, and provides an upper limit of $|d_e| < 8.7 \times 10^{-29}$ e·cm [19].

Another example is the measurement of temporal variation of proton-to-electron mass ratio, $\mu = m_p/m_e$. A spatiotemporal variation of the constants of nature has not been ruled out, or have even been predicted by theories extending the Standard Model [20]. A variation in μ would result in different amount of shifts in various types of energy states, e.g. rotational, vibrational, or electronic ones, as their energy levels have different dependence on μ. Therefore, by measuring transition frequen-

cies between two types of energy states which are close to accidental degeneracy, the relative shift in μ can be probed with enhanced sensitivity [9]. The advantage with molecules is that their complex internal structures provides great flexibility in choosing such transitions. For example, Ubachs and Bethlem *et al.* have investigated the variation of μ using $\sim 10\,\text{GHz}$ transitions between near accidentally degenerate rotational and torsional states of methanol [21]. These transitions can also be observed by radio-telescope from distant objects in the Universe, and this allows a comparison between laboratory measurements and radio-astronomy data.

1.1.3   Astro-physics and chemistry

With the development of radio telescopes, almost 200 molecular species have been detected in the interstellar space. Among them, H_2 has the largest abundance, followed by CO, NH_3, H_2O, and H_2CO, etc. [22]. These molecules form cold clouds in space with temperatures of $\sim 10\,\text{K}$ and densities of 10^3-$10^6\,\text{cm}^3$. These cold clouds undergo various processes and eventually collapse under gravitation to form protostars [23]. Thus, the interaction and chemistry among these molecules at a few Kelvin are of great interest for understanding the clouds evolution and star formation. In addition, understanding the spectra of [24] and the chemical reactions between [25] these species at cold temperatures are vital to understanding the formations of even bigger molecules with carbon, oxygen, nitrogen, or sulfur constituents in space. The laboratory studies on cold collisions and chemistry between these molecules could provide scattering cross sections and reaction rates that are difficult to obtain from radio-telescope observations, and hence are extremely valuable in astrophysics and chemistry.

1.2   Methods for the production of cold molecules

Various methods have been invented to circumvent the difficulty in cooling molecules. Notably, the 'indirect cooling' methods of creating ultracold molecules from alkali atoms using Feshbach resonances or photoassociations, have reached near quantum degenerate states [26, 27]. These methods take advantage of the well-developed atom-cooling schemes, assemble the ultracold atoms into ultracold molecules, and then transfer the population into the rovibrational ground state. However, these techniques are so far limited to diatomic molecules with alkali-atom constituents only. In the following, I will focus on available direct cooling methods.

Deceleration methods

A large variety of methods exist in the 'direct' production of cold molecules. For example, Stark decelerators were developed to slow down polar molecules, using the interaction between time-varying electric fields and the electric dipole moment of the molecules [28]. They can deliver molecular packets below $1\,\text{K}$ at an adjustable

final velocity down to $0\,\mathrm{m/s}$. However, due to the pulse-mode operation, the duty cycle of a Stark decelerator is low, and the density of the molecular beam obtained reaches only $10^5 \sim 10^7\,\mathrm{cm}^{-3}$. The magnetic counterpart of the Stark decelerator is the coil-gun experiment [29]. Another general approach to produce cold and slow molecules is the counter-rotating nozzle method [30, 31]. In this scheme, the super-sonic nozzle is mounted on a rotating rod, and sprays in the opposite direction of rotation. The molecules ejected from the nozzle are internally cooled down by adiabatic expansion [32]. Their forward velocities in the laboratory frame are canceled by the periphery velocity of the counter-rotating nozzle. This method, however, suffers from a low duty cycle as well. Moreover, the minimal velocities achievable are limited since if the molecules were too slow in the laboratory frame, their passway would be blocked by the incoming nozzle from the next round of rotation.

Laser and optoelectrical cooling

In addition to the above deceleration techniques, two 'active' cooling methods which compress the phase space density of the ensembles have been developed. One of them is the direct laser cooling, proposed by Di Rosa [33]. The experimental demonstrations have been carried out by DeMille *et al.* [34], Ye *et al.* [35], Hinds *et al.* [36], and Doyle *et al.* [37], on a handful of specially chosen diatomic radicals (e.g. SrF, YO, and CaF). The application of this method requires the very stringent condition that the molecules must have very favorable Frank-Condon factors. This minimizes the number of 'wrong' vibrational levels the molecules would populate after the spontaneous decay, hence reduces the number of repumping lasers necessary to close the cooling cycle. With this approach, the first molecular magneto-optical trap (MOT) has been realized [38], producing ~ 1000 SrF molecules at $\sim 400\,\mu\mathrm{K}$ [39].

Another approach is the optoelectrical Sisyphus cooling method developed by M. Zeppenfeld *et al.* [40], which extends cooling to also polyatomic molecules. This method essentially relies on an external electric field to remove the kinetic energy of molecules, and uses an infrared laser coupling to the excited vibrational levels to extract the entropy [41]. The number of rotational states populated after the spontaneous decay is limited by the selection rules of rovibrational transitions. The population landing in the very few other rotational levels of the ground state can be coupled to the 'correct' rotational level through microwave transitions. With only a single infrared laser used, $\sim 3 \times 10^5$ H_2CO molecules have been cooled to $\sim 400\,\mu\mathrm{K}$ with this method [42].

Both of these methods, however, require pre-cooled molecular samples to start the cooling process. On the one hand, in the laser cooling experiments, the diatomic radicals are typically produced by laser ablation which results in a temperature of $\sim 10^3\,\mathrm{K}$. To obtain sufficiently low kinetic energy and high internal-state purity for loading into a MOT, these molecules are first cooled in a buffer-gas cell [43], which helps to reduce the molecular temperature to $\sim 1\,\mathrm{K}$. On the other hand, in the optoelectrical cooling experiment, the polyatomic molecules need first loading into
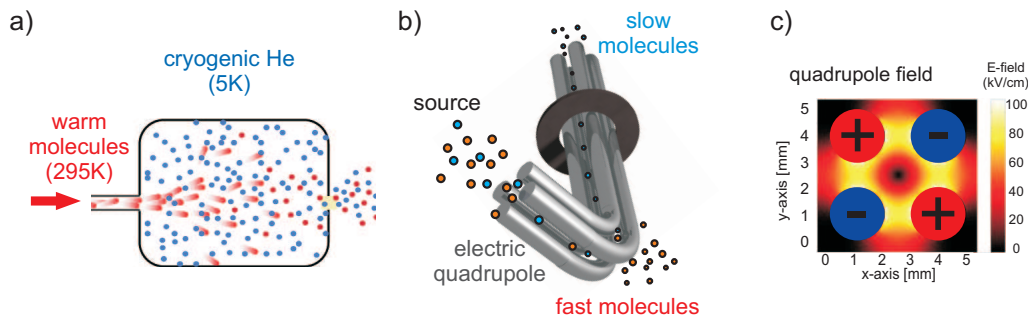
Figure 1.1: _Illustrations of different methods for production of cold molecules. (a) Buffer-gas cooling. (b) Electrostatic guiding and filtering. (c) Cross section of an electric quadrupole guide_

an electrostatic trap with typically $\sim 1\,\text{K}$ trap depth [44]. This is realized with the electrostatic filtering technique [45]. A brief overview of the buffer-gas cooling and electrostatic filtering is given in the following subsections.

1.2.1 Buffer-gas cooling

One powerful technique which has grown increasingly popular for molecule cooling, and which is also one of the focal points of this thesis is the buffer-gas cooling method [43]. Helium (or neon) gas is first cooled down in a cryogenic cell to the temperature of the cell wall (Fig.1.1 (a)). The molecules are then injected into the buffer-gas cell via a capillary or laser ablation. Collisions with the buffer-gas atoms lead to thermalization of the molecules to the cell temperature. This cooling method possesses three main advantages. Firstly, it is a generic method. As long as the molecules can be introduced into the cryogenic cell, via laser ablation or through a warm capillary, it can be cooled with the buffer-gas cooling technique. Secondly, this method can deliver huge output densities and fluxes of cold molecules. Output intensities up to $10^{13}\,\text{molecules}\,\text{s}^{-1}\text{cm}^{-2}$ have been achieved in different buffer-gas set-ups [46, 47]. Thirdly, both the translational and the internal degrees of freedom of molecules are cooled via elastic and inelastic collisions with the buffer-gas atoms [48]. Since the rotational energy spacings of many polyatomic molecules are $\sim 1\,\text{K}$, they can be cooled to the lowest rotational levels. The disadvantage of this method is however, that since a certain amount of buffer-gas density is necessary for a sufficient thermalization of molecules, this inherently introduces collisions in the vicinity of the cell output which accelerates the slowest molecules [49]. Thus, the velocity distributions at the output are shifted towards higher values.

1.2.2 Electrostatic Guiding and Filtering

Another technique which has been applied through out this thesis is quadrupole electrostatic filtering and guiding of polar molecules [45], as illustrated in Fig.1.1 (b). This method relies on the fact that there is a small fraction of molecules in

the lower velocity tail of a Boltzmann distribution. To filter them out, the Stark interaction between their electric dipole moment and the static field of the electric guide is employed. Molecules in low-field-seeking states can be confined in the field minimum along the quadrupole guide (Fig.1.1 (c)), provided their transverse kinetic energy does not exceed the trap depth. For a typical dipole moment of $\sim 1\,\mathrm{D}$ and a laboratory electric field strength of $\sim 100\,\mathrm{kV/cm}$, a trap depth of $\sim 1\,\mathrm{K}$ can be achieved. The maximal velocity that can be confined is referred to as the cutoff velocity in the rest of the thesis. The filtering of the longitudinal velocity of molecules is realized with a $90°$ bend along the guide (Fig.1.1 (b)). Molecules can make it through the bend if the Stark interaction provides a sufficient restoring force to overcome the centrifugal force [45].

1.3   About this Thesis

Despite the impressive progress in producing cold molecules witnessed in the last one and a half decades, a number of challenges still remain in this field. In this thesis, two of the long-standing problems will be addressed. Firstly, a comprehensive thermometry of cold polyatomic molecules, on which it is difficult to perform state-resolved detections with lasers, is demonstrated. Secondly, a centrifuge decelerator which outperforms all existing molecular deceleration methods in efficiency and output intensity is presented.

Chapter 2 presents a novel internal-state detection scheme which employs a resonant radio frequency depletion spectroscopy. This method does not involve optical transitions and is demonstrated with different polyatomic species. This method applies not only to the rotational-state detection, but also resolves the hyperfine splittings. In combination with a home-developed full Monte-Carlo trajectory simulation package, a comprehensive thermometry of polyatomic molecules is performed based on this detection technique.

Chapter 3 discusses the principle and design of a non-conventional molecular deceleration scheme. This method relies on a spinning electrostatic guide and employs the centrifugal force in the rotating frame to decelerate molecules to a standstill. As the concept of deceleration with centrifugal potential is rather general, this method works not only for molecules, but could also be extended to atoms and even neutrons. The design and assembly of this centrifuge decelerator is presented in detail.

Chapter 3 gives the proof-of-principle demonstration of the centrifuge deceleration. The signals obtained during the very first run are presented. Deceleration results for various polyatomic species, CH_3F, CF_3H, and CF_3CCH, are discussed. The continuity of the deceleration output is also demonstrated. The efficiency of the centrifuge decelerator is compared with the prediction of Monte-Carlo trajectory simulations.

Chapter 5 summarizes the work presented in this thesis and give an outlook. Especially, the combination of the buffer-gas cooling and the centrifuge deceleration,

the two main topics of this thesis, has been realized during the final phase of this thesis. The densities of slow molecules obtained from this combined set-up is so high that it has enabled the first observation of cold dipolar collisions between polyatomic molecules.

Chapter 2

Internal-state detection and thermometry of cold molecules

Cryogenic buffer-gas cooling has proven to be a very general and powerful method to produce internally and translationally cold molecules [43, 46, 50]. It has been applied to the cooling of various polyatomic species [51, 52], achieving molecular temperatures of the order of $\sim 1\,\mathrm{K}$ at much lower beam velocities compared to those generated by cooling via supersonic beam expansion [32]. In view of the great potential of buffer-gas cooling as a method for production of cold and slow polyatomic molecules for numerous experiments and applications, it is of paramount importance that the so-produced to be characterized. A general and robust method for probing the internal states and performing internal-state thermometry of polyatomic molecules, however, has been missing. The main challenge lies in the complexity of these molecules' structures, which restricts the application of the conventional methods e.g. light-induced fluorescence (LIF) and resonance-enhanced multi-photon ionization (REMPI). On the one hand, the LIF method would suffer from low photon scattering rate due to the lack of cycling transitions for polyatomic molecules. Unlike the alkali atoms or some of the diatomic radicals with good Frank-Condon factors [33, 53] which can scatter $\sim 10^2$ to 10^4 photons before decaying to the wrong levels, most polyatomic molecules can scatter at best 1 photon per particle. Moreover, many of the states in polyatomic molecules even have $\ll 1$ quantum yield due to non-radiative decays. On the other hand, the REMPI method would be limited by pre-dissociation of most polyatomic species. Pre-dissociation occurs when either the electronically excited level happen to be a repulsive state, or the the vibronic level in the excited state happen to cross with a repulsive state. Such crossings are more likely to happen on a multidimensional potential energy surface of polyatomic molecules than on the two dimensional potential energy curves of diatomic species. In addition, the transitions to the first electronically excited state for most polyatomic molecules are in the ultra-violet (UV) or deep UV. To realize a linewidth of $< 1\,\mathrm{GHz}$ (corresponding to the typical rotational constants of polyatomic molecules) of these UV lasers is technically challenging.

We have developed a new method for state detection, which has been applied to perform a full characterization of the properties of buffer-gas-cooled molecular beams, and, on this basis, to provide various insights into buffer-gas cooling [54]. The state detection is based on resonant radio-frequency (RF) depletion spectroscopy in a parallel-plate capacitor, which not only reveals the rotational-state distribution, but also resolves the hyperfine structures of the cold polyatomic molecules. To perform a thermometry of the buffer-gas-cooled molecular beams, the state detection method is combined with three other components. Firstly, we extract cold molecules from a buffer-gas cell by electrostatic guiding in a quadrupole guide [46]. Secondly, time-of-flight measurements are used to derive the longitudinal velocity distribution of the molecules at the end of the guide [55]. Thirdly, Monte-Carlo trajectory simulations of the electrostatic guiding allow for the properties of the molecules directly after the buffer-gas cell to be inferred from the signal at the end of the guide.

With this tool box, we have achieved the following results. We demonstrate rotationally resolving 100% of the population in the guided beams emerging from our cryogenic buffer-gas source, operated in either the effusive [49, 50] or the supersonic [56] regime. We have applied this method to different species of polyatomic symmetric-top polar molecules, fluoromethane, CH_3F, and 3,3,3-trifluoropropyne, CF_3CCH, and have compared their cooling processes. We provide clear evidence of the efficient control over the internal cooling of the guided molecular beams through varying the buffer-gas-cell temperature and the buffer-gas density, demonstrating the possibility of cooling far below the cell temperature in the supersonic regime. The detailed study of the buffer-gas cooling reveals two interesting phenomena. First, comparing the rotational with the translational temperature, we provide evidence that rotational cooling takes place more efficiently than translational cooling for the CH_3F-He system in the low He density regime. Second, the measurements provide indications of the dependence of the collisional relaxation rate on the rotational states of the molecules.

This chapter is structured as follows. Section 2.1 reviews the two different regimes of cryogenic buffer-gas cooling. Section 2.2 summarizes the relevant properties of the symmetric-top molecules studied in this work. Section 2.3 mentions briefly the results of electrostatic filtering. In Section 2.4 we explain the principle of our method for rotational-state detection of guided molecules, followed by the description of the experimental set-up in Section 2.5. The discussion of the line-assignment and diagnostics is given in Section 2.6. The characterization and analysis of the radio-frequency depletion measurements of rotational states and hyperfine states are described in Section 2.7 and Section 2.8, respectively. The Monte Carlo trajectory simulations used to calculate the guiding efficiencies for all relevant rotational states are described in Section 2.9. Finally, in Section 2.10 we present the results from the comprehensive characterization of our buffer-gas source. There we analyze the cell's output for different operating regimes and for different molecular species, and draw inferences on the cooling mechanisms in the buffer-gas cell.
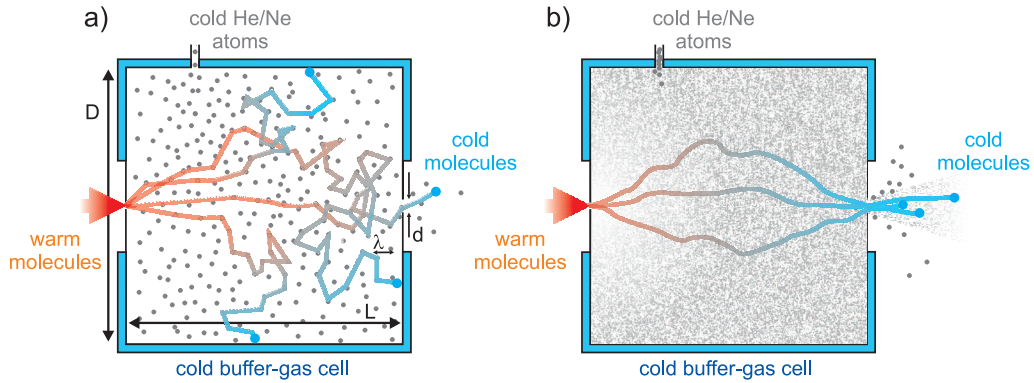
Figure 2.1: *Schematics of (a) the effusive regime, and (b) the hydrodynamic regime in a buffer-gas cell. D, L, and d denote the diameter and length of the cell, and the diameter of the nozzle, respectively. λ represents the mean free path for collisions between molecules and buffer-gas atoms. This figure is adapted from [58].*

2.1 Two regimes of buffer-gas cooling

This section gives an overview of the two different regimes of the cryogenic buffer-gas cooling, namely the effusive and the hydrodynamic regime. Due to the distinct gas dynamics in the cell, both the molecular extraction efficiency from the buffer-gas cell and the final molecular temperature after the cooling are different between the two regimes. In the following only an intuitive picture of the buffer-gas dynamics is presented, and the main conclusions are outlined. For further details, the readers are referred to D. Patterson's and C. Sommer's Ph.D theses [48, 57].

Although the principle of cryogenic buffer-gas cooling is very basic (see Sec. 1.2.1), the extraction of the cold molecules out of the cryogenic environment is less straight-forward. Generally molecules have very low vapor pressure at $\sim$ 5-20 K, and the vast majority of them end up freezing on the inner surface of the cell. Depending on the particle densities in the cell, different gas dynamics can ensue, as follows:

- **The effusive regime**: in the low density limit with typically a few $10^{14}\,\mathrm{cm}^{-3}$ buffer-gas atoms in the cell, molecules undergo primarily random walk, as illustrated in Fig.2.1 (a). Through the process of diffusion, the molecules either leave the cell through the exit hole or freeze out on the inner surface of the cell. The cell extraction efficiency is approximated by the ratio of the area of the nozzle and the area of the inner surface. For our setup, the nozzle dimension $d \sim 2\,\mathrm{mm}$, and the cell dimension L (or D)$\sim 2\,\mathrm{cm}$, hence the extraction efficiency $\sim \frac{d^2}{6L^2} \sim 10^{-3}$.

- **The hydrodynamic regime**: in the high density limit with typically a few $10^{16}\,\mathrm{cm}^{-3}$ buffer-gas in the cell, the collision mean free path λ is much smaller than the nozzle size d, and the large pressure gradient across the nozzle creates a macroscopic flow. In this case, molecules are entrained in the buffer-gas

flow and leave the cell before they diffuse to the cell wall, as illustrated in Fig.2.1 (b). The cell extraction efficiency approaches unity for high buffer-gas densities.

It should be mentioned that the hydrodynamic enhancement of the cell extraction efficiency only holds if no vortices build up, which could trap molecules in the cell. When such vortices are formed in the cell, cold molecules could spend longer time circulating and eventually may diffuse to the cell wall, as suggested by the work from Bulleid, et al. [59]. The formation of vortices depends not only on the gas density and cell temperature, but also on the geometry of the cell. Hence, the prediction of vortex formation requires comprehensive numerical fluid dynamics simulations.

The different gas dynamics also results in different final temperatures of the molecules. In the effusive limit, molecules are expected to thermalize eventually to the temperature of the cell, $T_{mol} = T_{cell}$, in both their translational and rotational degrees of freedom. The mean velocity of the extracted molecular beams is $\approx \sqrt{3k_B T_{cell}/m_{mol}}$, where k_B is the Boltzmann constant and m_{mol} is the molecular mass. In comparison, molecules can be cooled to much below T_{cell} in the hydrodynamic limit. Due to the large pressure gradient in the vicinity of the nozzle, particles undergo adiabatic expansion, in which they convert their internal energy into kinetic energy [32]. In this process, particles get colder in the co-moving frame but move forward faster in the lab frame. In the very high density limit, the gas mixture expands to a supersonic beam after leaving the cell. The final temperature reached in this limit is given by [32]

$$\frac{T_{mol}}{T_{cell}} = \frac{1}{1 + \frac{1}{2}\left(\gamma - 1\right)\mathcal{M}^2}, \tag{2.1}$$

where γ is the heat-capacity ratio for the buffer gas with a value of $5/3$ for monatomic gases used here, and $\mathcal{M}$ is the Mach number defined by the ratio between the flow velocity v_f and the local speed of sound v_s. From Eq.2.1 and the definition of $\mathcal{M}$, v_f after the adiabatic expansion can be obtained,

$$v_f = \mathcal{M}\,v_s = \mathcal{M}\,\sqrt{\gamma\frac{k_B T_{mol}}{m}} = \sqrt{\frac{\gamma\mathcal{M}^2}{2 + (\gamma - 1)\mathcal{M}^2}}\sqrt{\frac{2k_B T_{cell}}{m}}, \tag{2.2}$$

where m is the mass of a buffer-gas atom. The terminal velocity of the flow at the limit of $\mathcal{M} \gg 1$ after the supersonic expansion is given by,

$$v_{f,supersonic} \approx \lim_{\mathcal{M}\to\infty} v_f = \sqrt{\frac{5}{2}}\sqrt{\frac{2k_B T_{cell}}{m}} \approx 1.58\sqrt{\frac{2k_B T_{cell}}{m}}, \tag{2.3}$$

This last step gives the maximum flow velocity for a monatomic gas under supersonic expansion. A more rigorous derivation can be found in [60].

2.2 The symmetric-top molecule

Before starting the explanation of our method for the rotational-state detection, we shall give a brief overview of the relevant properties of symmetric-top molecules, which are used in the current study. For the detailed description of symmetric-top molecules, one can refer to different standard literature, e.g. Townes and Schawlow [61]. The rotational states of symmetric-tops can be fully described by three quantum numbers, the total angular momentum, J, its projection on the molecule's symmetry axis, K, ($K = -J, ..., J$), and its projection on a laboratory-fixed axis, M, ($M = -J, ..., J$). Hereinafter the rotational states will be designated as $|J, K, M\rangle$ or $|J, K\rangle$, depending on the need to specify the quantum number M.

In a field-free region, the energy of symmetric-tops in the rigid-rotor approximation is $E_{J,K} = h[BJ(J + 1) + (A - B)K^2]$, where h is Planck's constant, and A and B are the rotational constants of a symmetric-top molecule. For $|J, K\rangle$ states with $K \neq 0$, they are degenerate with the $|J, -K\rangle$ states. This gives rise to linear Stark-shifts in the presence of an external electric field. The external electric field splits every $|J, K\rangle$ state (Stark effect) into $2J + 1$ M-sublevels, corresponding to all possible projections of $\mathbf{J}$ on the electric-field axis. The first-order Stark splitting is given by the expression

$$E^{(1)} = -d\mathcal{E}\frac{KM}{J(J + 1)}, \qquad (2.4)$$

where d and $\mathcal{E}$ stand for the permanent electric dipole moment of the molecule and the electric-field strength, respectively. Sublevels with a positive Stark shift are referred to as low-field-seeking states (states that can be guided). Since states $|J, -K, M\rangle$ are degenerate with states $|J, K, -M\rangle$ under inversion symmetry, we ignore hereinafter the sign of K and adopt the convention that states with positive M are low-field-seeking. However, when calculating the statistics of state-distribution, this double contribution is considered. An example of the Stark effect is presented in Figure 2.2(a) for the $|1, 1\rangle$ and $|2, 1\rangle$ states of CH_3F.

For $|JK\rangle$ states with $K = 0$, the first-order Stark splitting is zero. In this case, low-field-seeking states due to the second-order (quadratic) Stark shift exist, if they satisfy the condition $J(J + 1) > 3M^2$, which derives from the expression for the quadratic Stark shift at $K = 0$ [61],

$$E_{K=0}^{(2)} = -\frac{d^2\mathcal{E}^2}{2hBJ(J + 1)} \left[\frac{3M^2 - J(J + 1)}{(2J - 1)(2J + 3)}\right]. \qquad (2.5)$$

This is deduced from the general expression of $E^{(2)}$,

$$E^{(2)} = -\frac{d^2\mathcal{E}^2}{2hB} \left\{\frac{(J^2 - K^2)(J^2 - M^2)}{J^3(2J - 1)(2J + 1)} - \frac{[(J + 1)^2 - K^2][(J + 1)^2 - M^2]}{(J + 1)^3(2J + 1)(2J + 3)}\right\}. \qquad (2.6)$$

Clearly, the quantum numbers M and K are symmetric in the expression of $E^{(2)}$. Thus, the states with $M = 0$ can also be low-field-seeking, provided that $J(J + 1) > 3K^2$.

2.3 Electrostatic filtering

Following the linear and quadratic Stark shift discussed in Sec. 2.2, we now summarize the electrostatic filtering results. In Sec. 1.2.2, we have briefly mentioned the electric quadrupole guiding and filtering. In the transverse direction of the guide, the cut-off velocity of molecules is given by $v_{t,cut} = \sqrt{2E_{max}/m_{mol}}$ when the transverse kinetic energy is equal to the trap depth, where E_{max} is the maximal Stark shift, and m_{mol} is the molecular mass. The filtering of the longitudinal velocity of molecules is realized with a 90° bend along the guide. The maximal longitudinal velocity of the molecules is obtained when the Stark interaction provides a restoring force $\approx E_{max}/r$ equal to the centrifugal force at the bend $m_{mol}v_f^2/R$, where r is the distance from the guide center to the electrode surface, v_f is the forward velocity, and R is the bend radius. The cut-off velocity in the longitudinal direction is then given by [49], $v_{l,max} = \sqrt{E_{max}R/(rm_{mol})} = \sqrt{R/(2r)}v_{t,cut}$.

2.4 Method

Having briefly reviewed both the cooling method (Sec. 2.1), the type of molecules subjected to the buffer-gas cooling (Sec. 2.2), and the electrostatic guiding and filtering, here we outline the method developed in this thesis for performing internal-state thermometry of the buffer-gas cooled molecules. The principle of rotational-state detection is based on state-selective addressing and elimination of molecules from a guided population by applying an RF field resonant to the DC Stark splitting in a homogeneous field. This leads to a depletion of the measured signal and reveals the relative state population.

The detailed scheme is illustrated in Figure 2.2. Molecules emerging from the cryogenic source populate different rotational states $|J, K\rangle$. Only molecules in low-field-seeking M-sublevels (red lines in Figure 2.2(a)), however, are confined in the guide. Subsequently, the guide is interrupted by a parallel-plate capacitor creating a homogeneous offset electric field. At low field, this causes equidistant Stark splitting of the M-sublevels for a given $|J, K\rangle, K \neq 0$ state. The magnitude of the splitting is unique for most of the low-lying $|J, K\rangle$ states for a given offset field (see Figure 2.2(a)). This allows for $|J, K\rangle$ states to be addressed individually. To address a particular the rotational state, an RF field resonant to the Stark splitting between its M-sublevels is applied to the capacitor, and transfers the molecules into different M-sublevels. Those molecules which land in non-guidable states (blue lines in Figure 2.2(a)) are lost from the guide after the capacitor, leading to a depletion signal on the detector.

To know accurately the ratio between the depletion signal and population between the addressed state, it is necessary to achieve a good control over the resulting M-substate distribution. The approach we take is to broaden the RF signal with white noise and hence eliminate coherent effects in the population transfer process. Thereby we ensure molecules are equally redistributed among all the M-sublevels
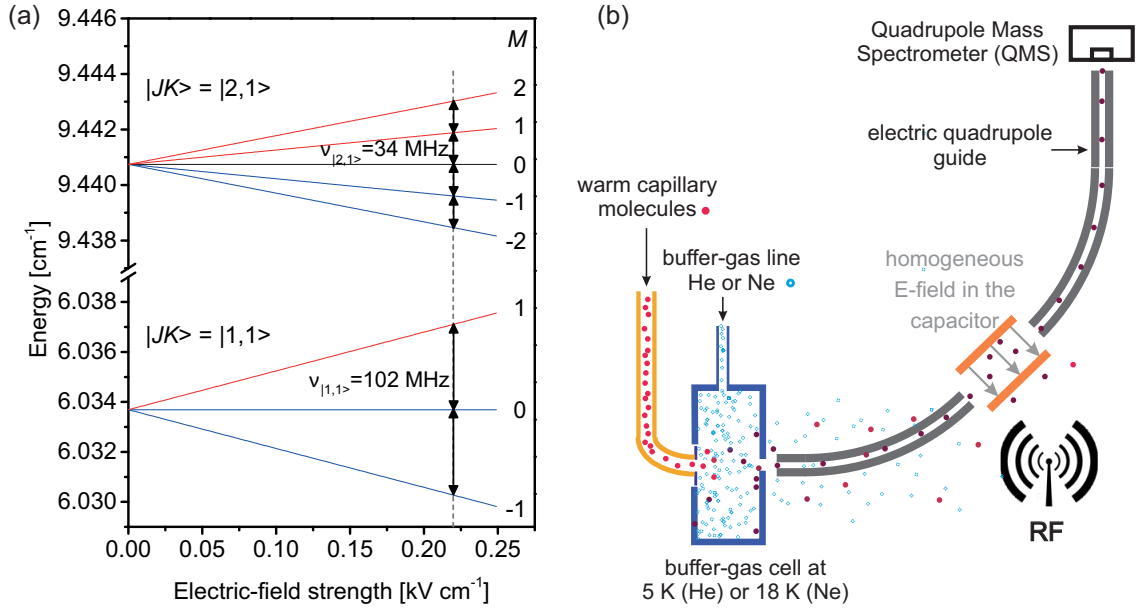
Figure 2.2: *(a) Stark splittings as a function of the applied electric field for two rotational states of* CH_3F, $|1,1\rangle$ *and* $|2,1\rangle$: *red lines show guidable sublevels, and blue lines show non-guidable ones. The* $|2,1,0\rangle$ *state is weakly guidable due to its second-order Stark shift. The vertical dashed line designates the applied homogeneous electric field (*$220\,\mathrm{V\,cm^{-1}}$*) used in the radio-frequency scans shown in Figure 2.7(a). The arrows show the magnitude of the Stark splitting corresponding to the applied electric field. (b) Scheme of the experimental set-up.*

within the given $|J, K\rangle$ rotational state (Figure 2.2(a)), when the state transfer is power-saturated. To a first approximation, the depletion ratio in this case is given by the fraction of molecules converted from guidable to non-guidable states, and this is the ratio between the number of non-guidable M-sublevels and the total number of M-sublevels, i.e., $\frac{J+1}{2J+1}$ for a linear Stark shift. The fraction of guided molecules populating the probed rotational state is therefore obtained by dividing the magnitude of the saturated depletion by this ratio.

This simple depletion ratio mentioned above is obtained under the assumption that all low-field-seeking M-sublevels have the equal guiding efficiency in the quadrupole guide. A more realistic scenario is however that a guidable state with a smaller M-value typically has a weaker Stark shift, hence a lower guiding efficiency than a guidable state with larger M. Therefore, it also contributes to the depletion signals when population is transferred from a low-field-seeking level with larger M-value to the ones which are still guidable but with smaller M-values. Thus the simplified depletion ratio needs to be corrected including the subtle effects of guiding efficiency for different M-sublevels. This correction is described in detail in Section 2.9.

2.5 Experimental Set-up

The experimental set-up is sketched in Figure 2.2(b). In our experiment, molecules and buffer-gases come from lecture bottles. The buffer-gas cooling takes place in a cryogenic cell where a continuous flow of polyatomic polar molecules is mixed with a continuous flow of helium or neon at cryogenic temperatures of 5 K or 18 K, respectively. The exact cell temperature can be monitored by diode sensors and controlled by an electric heating block. The gas inflow is monitored by capacitance gauges (CMR series, Pfeiffer Vacuum) and regulated by needle valves (UDV 040, Pfeiffer Vacuum) along the corresponding gas lines. In the later development, these have been replaced by Alicat flow meters and controllers. After the cold molecules leave the cell, they are captured by a quadrupole guide, which delivers them to a detector or to further experiments. The experimental set-up is an upgraded version of the set-up described previously [55] to enable RF depletion spectroscopy on the guided molecules.

Our buffer-gas set-up can be operated in both the effusive and the hydrodynamic regimes, which require different geometries. For the effusive regime, the guide is distanced about 2 mm from the cell nozzle. In the case of the hydrodynamic regime, that spacing is about 20 mm to allow enough distance for the supersonic beam formation. The cell exit aperture used in our experiments has a diameter of 2 mm. The maximum electric field that can be achieved between the guiding electrodes is about $100 \, \text{kV} \, \text{cm}^{-1}$. The guides before and after the capacitor region are both 20 cm in radius and are bent by 45°. We use a quadrupole mass spectrometer (QMS, Model No. Pfeiffer QMA410) to detect the molecules after they leave the guide.

The capacitor for driving RF transitions is made of two parallel ($2 \, \text{cm} \times 2.7 \, \text{cm}$) plates with a 2.75 mm spacing between them. A bias voltage from $\sim 10 \, \text{V}$ up to $\sim 1 \, \text{kV}$ is applied to the capacitor, providing a homogeneous electrostatic field between the plates. The capacitor is separated from the two guide segments by gaps of 1 mm.

The plates are made from plain FR-4 printed circuit boards (PCB) of 1.5 mm thickness. High-vacuum test has shown that this FR-4 PCB of several cm^2 is compatible with down to 10^{-8} mbar vacuum at a nominal pumping speed of *c.a.* 700 l/s (HiCube 700 Classic, Pfeiffer Vacuum). The RF power connection from the SMA coaxial cable to the PCB was soldered with ultra high vacuum compatible material (UHV Solder, Allectra). During the actual experiment, the pumping speed from the cryogenic charcoal surface is $\sim 3 \times 10^3$ l/s [48], hence the outgassing problem of this homemade structure is negligible. One of the plates is a plain board, whereas the other one features a T-shaped microstrip (see Figure 2.3) used to apply the RF field. This structure was homemade with a milling machine specialized for circuit board prototyping (ProtoMat S63, LPKF). The T-shaped microstrip is connected to the core of the SMA cable carrying the RF signal. The outer flat surface of this plate is connected to the grounding shield of the SMA cable. As the top edge of the T-shape is aligned with the molecules' flow axis, the RF field is expected to
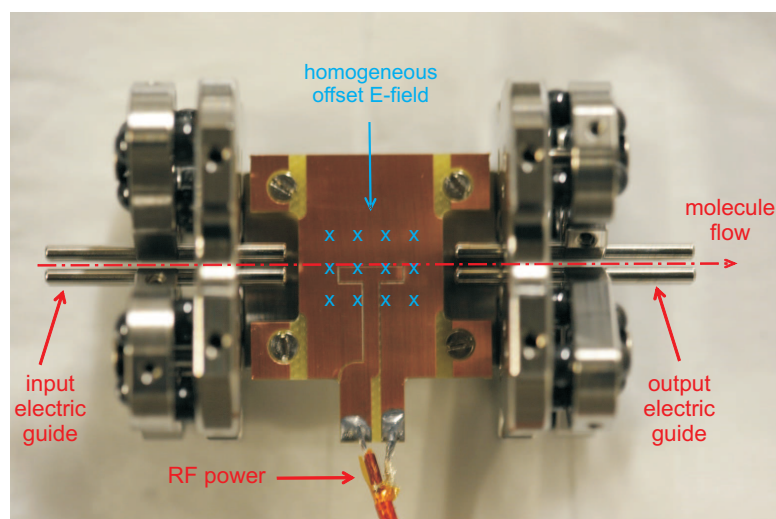
Figure 2.3: *Topview of one of the parallel capacitor plates which features a T-shaped microstrip. The RF power is connected to the T-shaped structure. The metal rods at the two sides are the input and output quadrupole guide, which are fixed by the stainless steel holders. The blue crosses indicate the direction of the homogeneous offset E-field which is used to polarize the molecular orientation.*
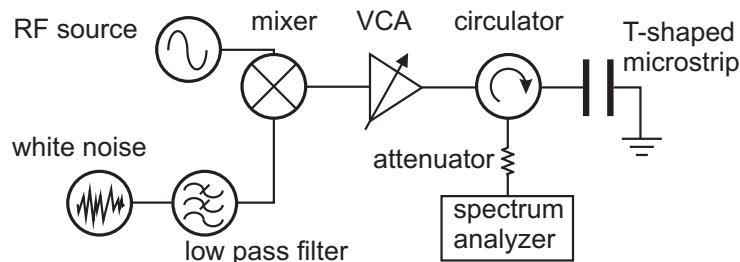
Figure 2.4: *Schematic of the RF connection.*

be predominantly perpendicular to the homogeneous field in the molecules' transit region. This configuration enables driving of $\Delta M = \pm 1$ transitions.

The scheme of the RF circuit outside the vacuum chamber is shown in Figure 2.4. The RF source is an AnaPico APSIN3000 signal generator, operating in the range from 9 kHz to 3 GHz. When coherent effects in the RF transition need to be eliminated, the RF signal is mixed with white noise which is generated by an Agilent 33220A arbitrary waveform generator and filtered by a 2.5 MHz low-pass filter. The power of the frequency-broadened signal is regulated via a voltage-variable attenuator followed by a fixed amplifier. Before the RF power is sent to the T-shape in the vacuum, it passes through a circulator which prevents the reflected power from entering the amplifier and directs it into a spectrum analyzer after attenuation for monitoring. The RF cable inside vacuum is a UHV-compatible SMA cable.

2.6 Line assignment and diagnostics

Before quantitatively studying the results of the resonant radio frequency deple-
tion measurements, we need to identify all the observed lines, and diagnose any
unexpected spectral features. According to the principle discussed in Sec. 2.4, the
assignment of real lines should be straightforward. For a molecule with a permanent
electric dipole moment d and an offset electric-field strength $\mathcal{E}$, any of its $|JK\rangle$ states
with linear Stark-shifts would give rise to a depletion line at $h\nu = -d\mathcal{E}K/[J(J+1)]$.
The line assignment in Figure 2.7 is based on this simple rule.

In addition, some unexpected depletion lines were also observed in the initial
spectrum, which turned out to be independent of any particular molecular transi-
tions. Our speculation is that this non-resonant depletions might originate from the
excessive RF power deposited into the molecular passage region, when the frequency
accidentally hits the resonance of the RF circuit inside the vacuum. In fact, we have
eventually found out that by grounding one SMA connection inside the vacuum,
or by re-arranging the RF cables and connection inside the vacuum, we could shift
these lines to outside the spectral window of the measurement.

Here, an example of such 'fake' transitions, and how we performed the diag-
nostics are summarized. During the early stage of the experiment where CH_3F
($d = 1.85\,D$) was used, and $30\,V$ was applied across the capacitor (corresponding
to $\mathcal{E} \approx 110\,V/cm$), an unexpected depletion line at $40\,MHz$ was observed. This
line does not correspond to any rotational state. In addition, by grounding both
parallel plates of the capacitor, this line shifted to about $37.5\,MHz$. By changing
the molecule species from CH_3F to ND_3 and CF_3H which possess different values of
d and neither is expected to have lines at around $40\,MHz$, this dip in the spectrum
was always present. At the same time, a feature at $40\,MHz$ also appeared on the
spectrum analyzer monitoring the RF power reflected from the T-shape (see Fig-
ure 2.5). It also shifted to $37.5\,MHz$ on the spectrum analyzer when grounding both
capacitor plates. These imply the feature does not depend on the molecular species,
but probably on the instruments.

To track where this reduction of molecular signal occurred, we applied a pulsed
RF power (with $2\,ms$ pulse-width) to perform time-of-flight (TOF) measurement
with CF_3H. As shown in Figure 2.6, three separate measurements were performed
with the following parameters: 1) with $30\,V$ across the capacitor and $22.5\,MHz$ RF
corresponding to the $\Delta M = \pm 1$ transition for the $|3,3\rangle$ state (real transition); 2)
with $30\,V$ across the capacitor and $40\,MHz$ RF ('fake' transition); 3) with grounding
the capacitor plates and $37.5\,MHz$ RF (shifted 'fake' transition). The three traces
have been rescaled vertically to match their amplitudes. The RF pulses were applied
at $0\,ms$ and the horizontal scale shows the time-of-flight response of the depletion.
For the real transition (Measurement 1), the depletion started at about $7.5\,ms$. This
was expected because the molecules were moving at a peak velocity of $180\,m/s$, and
the distance from the capacitor plates to the detector was about $1.3\,m$. The traces
of the two 'fake' dips overlap approximately with the trace from the real transition.
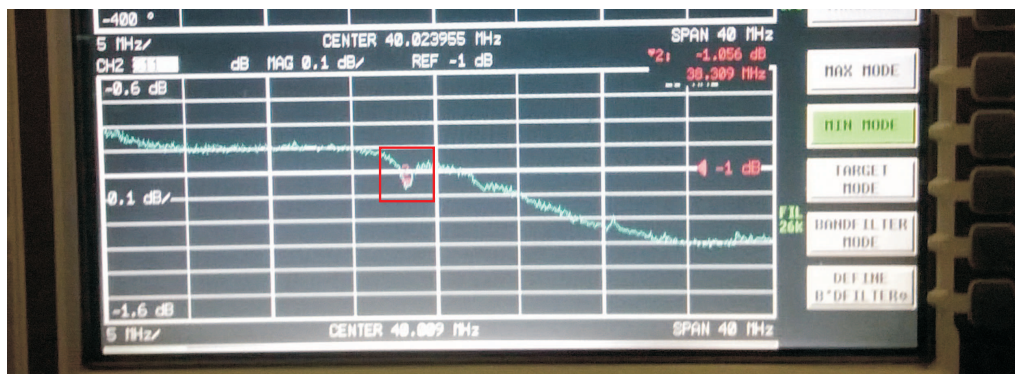
Figure 2.5: *Snapshot of the Spectrum Analyzer monitoring the reflected RF power from the setups in the vacuum chamber. The red box highlights the dip in the spectrum at 40 MHz.*
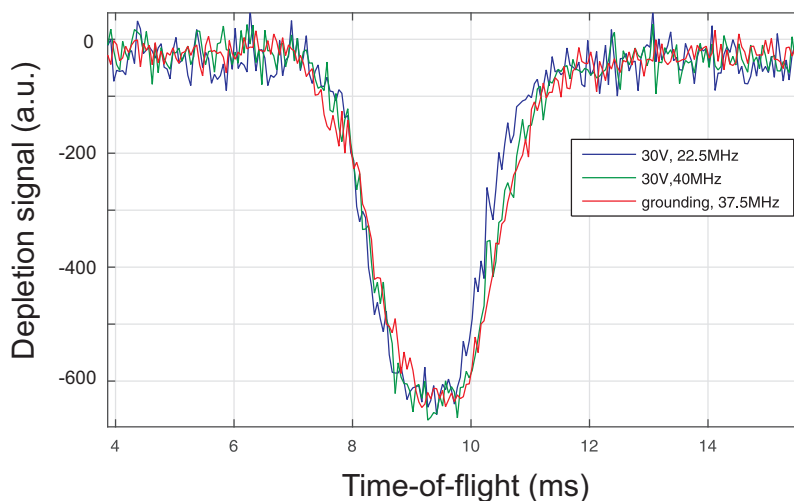
Figure 2.6: *Tracing the location of molecule depletion with time-of-flight method. The blue line results from a real transition of the CH_3F molecules applied, while the green and the red lines are from the 'fake' transitions.*

This same temporal response implies the 'fake' depletion around 40 MHz indeed happens in the capacitor region.

This non-resonant ('fake') depletion of molecules as well as the dip of the reflected power on the spectrum analyzer could be simultaneously eliminated from the spectrum by grounding one SMA connection inside the vacuum.

2.7 Resonant radio frequency depletion measurements

In this Section we present the characterization and the analysis of radio-frequency depletion measurements of buffer-gas-cooled and electrically guided molecules, and
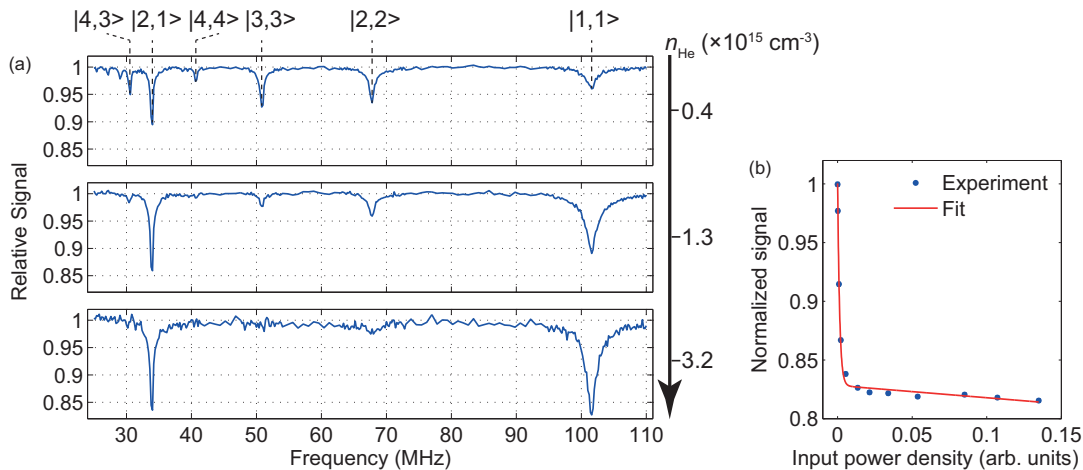
Figure 2.7: *(a) RF depletion spectra of* CH$_3$F *for different He densities in the buffer-gas cell ($T_{\text{cell}} = 6.7\,$K). The most prominent dips are assigned to the corresponding $|J, K\rangle$ rotational states. (b) Depletion saturation measurement for the $|1, 1\rangle$ state of* CH$_3$F*. The fit to the experimental points is a sum of an exponential and a linear power dependence (For details, see text).*

the derivation of their rotational-state distribution based on these measurements. Results from both the effusive and the hydrodynamic regimes are shown.

2.7.1 Effusive regime

Figure 2.7(a) shows the relative count rate of guided cold fluoromethane, CH$_3$F, as a function of the applied RF frequency, in the effusive regime of buffer-gas cooling. The buffer-gas densities in the cell are 3.7×10^{14}cm^{-3}, 1.3×10^{15}cm^{-3}, and 3.2×10^{15}cm^{-3}, and the cell temperature is $6.7\,$K. The applied homogeneous electric field of $220\,$Vcm^{-1} was the same for all three scans. The linear Stark splittings for different $|J, K\rangle$ rotational states of fluoromethane have been calculated for the applied homogeneous electric field, and, on this basis, the observed features in the depletion spectrum have been assigned. The assignments of the most prominent dips are shown in the figure. The broadening of the lines is attributed to the inhomogeneity of the electric field, which leads to a linewidth proportional to the scanning frequency.

Figure 2.7(a) shows a clear change in the dip pattern and in the relative dip depth as the buffer-gas density is changed. Increasing the buffer gas density in the cell increases the number of collisions and therefore leads to a lower rotational temperature. This effect is clearly visible, as the depletion signal corresponding to the low-lying rotational states $|1, 1\rangle$ and $|2, 1\rangle$ increases, while the signal from the other states of higher rotational energy decreases, and eventually vanishes.

The magnitude of the depletion signal depends not only on the thermal population of the probed state, but also on the applied RF power. To eliminate this effect, we performed RF power scans for each $|J, K\rangle$ rotational state to obtain its

State $\vert JK \rangle$	Depletion (%)	Nominal DR	Simulated DR (%)	Population (%)
$\vert 1,1 \rangle$	16.96 (0.14)	2/3	66.7	25.4 (0.2)
$\vert 2,1 \rangle$ [$\vert 3,2 \rangle$]	19.07 (0.11)	3/5 [4/7]	57.3 [58.8]	32.8 (0.2)
$\vert 3,1 \rangle$	5.08 (0.12)	4/7	54.3	9.4 (0.2)
$\vert 4,1 \rangle$	1.02 (0.13)	5/9	55.6	1.8 (0.2)
$\vert 2,2 \rangle$	1.88 (0.11)	3/5	62.2	3.0 (0.2)
$\vert 1,0 \rangle$	12.32 (0.15)	2/3	66.7	18.5 (0.2)
$\vert 2,0 \rangle$	5.6 (0.4)	2/3	66.0	8.5 (0.6)
Total	62.6 (0.5)			**99.4 (0.8)**

Table 2.1: *Experimental relative populations of the $\vert J, K \rangle$ rotational states of* CH_3F, *derived from saturated depletion signals measured for each of the rotational states at* $T_{cell} = 6.4\,K$ *and* $n_{He} = 1.6 \times 10^{15}\,cm^{-3}$. *Nominal and simulated depletion ratios (DR), are defined and explained in the text. The values in parentheses of the depletion and the population columns are the statistical errors. The $\vert 3, 2 \rangle$ state in the square brackets in the second row shares the same Stark splitting with the $\vert 2, 1 \rangle$ state, and its contribution to the depletion signal is also taken into account. The corresponding depletion ratios for the $\vert 3, 2 \rangle$ state are also given in square brackets in the third and fourth column.*

power-saturated depletion level. Coherent effects, which lead to Rabi oscillations between the M-sublevels and therefore hinder an equal redistribution of population among all M-sublevels, were eliminated by broadening the RF signal to 5 MHz with white noise as explained in Sec. 2.5 (the white noise is not applied in the frequency scan in Figure 2.7(a)). An example of an RF power scan is shown in Figure 2.7(b) for the $\vert 1, 1 \rangle$ state of CH_3F, where the relative signal is plotted as a function of the applied RF power spectral density. The data were fitted with a sum of an exponential and a linear function. The exponential term is attributed to resonant driving of the transition of interest, while the linear decay term is attributed to off-resonant driving of transitions in other states taking place in the non-homogeneous-field regions near the quadrupole guide, as well as to transitions driven by higher harmonics produced by the RF amplifier that are not perfectly filtered out. The sought value of the saturated depletion for each of the considered rotational states is taken to be the amplitude of the exponential function. For CH_3F we have performed saturation scans only for states with $J \leq 4$, as these states account for $> 99.7\%$ population below 10 K according to a Boltzmann distribution.

Results from the RF depletion measurements of CH_3F for $T_{cell} = 6.4\,K$ and $n_{He} = 1.6 \times 10^{15}\,cm^{-3}$ are shown in Table 2.1. The values listed in the second column show the measured depletion signal for a given rotational state $\vert JK \rangle$ from the RF depletion scans. The nominal depletion ratio, $\frac{J+1}{2J+1}$ (discussed in Section 2.4),
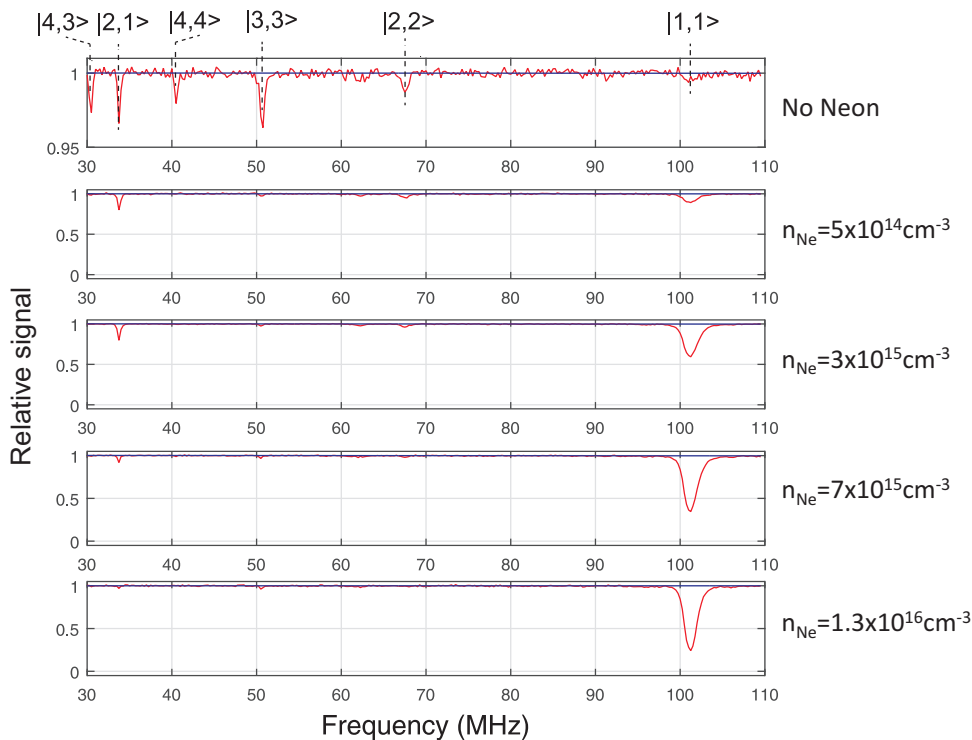
Figure 2.8: *RF depletion spectra of CH_3F for different Ne densities in the hydrodynamic regime. The buffer-gas cell is operated at about $17\,K$. All the depletion dips are assigned to the corresponding $|J, K\rangle$ states. As in the experiment shown in Figure 2.7(a), the $5\,MHz$ white noise was not applied in the radio frequency scan.*

is listed in the third column. The more accurate simulated depletion ratio obtained from the trajectory simulations described in detail in the next Section is listed in the fourth column of Table 2.1. The relative population of each of the rotational states $|JK\rangle$ present in the guided beam can be deduced from the ratio of the measured depletion signal and the simulated depletion ratio. Note that the sum of the state populations is $\sim 100\,\%$, indicating our ability to account for the entire population of rotational states of CH_3F present in the guided beam.

2.7.2 Hydrodynamic regime

Section 2.7.1 demonstrates that our detection method is capable of resolving 100% of the population in the guide, here we show further that by operating the buffer-gas cell with neon atoms in the hydrodynamic regime (see Sec. 2.1), almost the entire guided population can be obtained in a single rotational state. When the buffer-gas density in the cell is increased to a level where the collision mean-free-path at the nozzle is much smaller than the nozzle dimension, adiabatic expansion at the nozzle vicinity takes place. This cools down further both the translational and the

rotational degrees of freedom of the molecules. As shown in Figure 2.8, when the buffer-gas density was increased to above $10^{16}\,cm^{-3}$, about all the guided population was found eventually in the lowest guidable rotational state, the $|1,1\rangle$ state. Since only the $M = 1$ sublevel of the $|1,1\rangle$ state has positive Stark-shift, almost all the population in the guide then is effectively in the single $|J, K, M\rangle$ state. It will be shown later in Sec. 2.10.4 that the rotational temperature for the supersonically cooled CH_3F beam is $(2.1 \pm 0.1)\,K$.

2.8 Resolving hyperfine splittings of polyatomic molecules

After demonstrating the production of cold polar molecules in a single $|J, K, M\rangle$ state (see Sec. 2.7.2), we would like to check whether our resonant RF depletion method is capable of resolving also the hyperfine splittings. In this section, we show the ability of our method to resolve the hyperfine structure of ND_3 resulting from the nuclear quadrupole coupling of the nitrogen atom.

2.8.1 Theoretical review

To understand the experimental results, we set out first with a brief review of the theory of molecular hyperfine structures. A thorough theoretical treatment on this topic have existed since the 1950s, and the readers should refer to [62] for more details. To summarize the relevant results, the Hamiltonian for the hyperfine interaction includes two terms,

$$\mathcal{H}_{hyp} = \mathcal{H}_{MHS} + \mathcal{H}_Q. \tag{2.7}$$

The first term is the nuclear magnetic coupling, $\mathcal{H}_{MHS} = b\vec{I}\cdot\vec{S} + cI_Z S_Z + C_I \vec{N}\cdot\vec{I}$, where b, c, and C_I are the nuclear coupling constants, $\vec{I}$ is the nuclear spin, I_Z (S_Z) is the projection of $\vec{I}$ ($\vec{S}$) on the quantization axis. However, for a closed-shell molecules (typically chemically stable) e.g. ND_3, or CH_3F, etc., their electron spins pair up and leave $S = 0$, Thus, we are left with only the last term $C_I \vec{N} \cdot \vec{I}$, the nuclear spin-rotational coupling, which is fairly weak.

The second term, $\mathcal{H}_Q$ is the interaction of the intra-molecular field gradient with the electric quadrupole moments of the nuclei. This is the strongest interaction, provided the nuclear quadrupole moment exists, which is the case for all nuclei with spins ≥ 1. Whereas nuclei with spins 0 or 1/2 are spherically symmetric, and consequently do not possess a quadrupole moment [62]. To sum up the results, the following expression can be obtained after a lengthy derivation,

$$\mathcal{H}_Q = \frac{eQq_J}{2J(2J-1)I(2I-1)}\left[3(\vec{I}\cdot\vec{J})^2 + \frac{3}{2}\vec{I}\cdot\vec{J} - \vec{I}^2\vec{J}^2\right]. \tag{2.8}$$

Here, e is the elementary electric charge. Q is a scalar with the units of area called the quadrupole coupling constant, and is related to the intrinsic quadrupole moment

F	2	1	0
C	2	-2	-4
C(C+1)	6	2	12

Table 2.2: *The corresponding values of C and $C(C + 1)$ for each F, in the case of $I = 1$ and $J = 1$.*

of the nuclei Q^* by $Q = \frac{2I-1}{2(I+1)}Q^*$. q_J is the electric-field gradient along the space-fixed Z axis averaged over the states $M_J = J$, $q_J = \left\langle J, J \left| \frac{\partial^2 V}{\partial Z^2} \right| J, J \right\rangle$. In a field-free region, $\vec{J}$ and $\vec{I}$ directly couple to form $\vec{F} = \vec{J} + \vec{I}$, hence

$$\vec{I} \cdot \vec{J} = 1/2(\vec{F}^2 - \vec{J}^2 - \vec{I}^2). \tag{2.9}$$

Substituting Eq. 2.9 into Eq. 2.8 and knowing the basic results of the angular momentum operator, we get the eigenvalues of $\mathcal{H}_Q$,

$$E_Q = \frac{eQq_J}{2J(2J - 1)I(2I - 1)} \left[\frac{3}{4}C(C + 1) - J(J + 1)I(I + 1) \right], \tag{2.10}$$

where

$$C = F(F + 1) - J(J + 1) - I(I + 1). \tag{2.11}$$

2.8.2 Experimental demonstration

Before explaining the measured hyperfine spectrum, we summarize the relevant properties of the molecule used in the experiment, ND_3. Firstly, the rotational constant of ND_3 is $5.1\,cm^{-1}$, much larger compared to that of CH_3F ($0.85\,cm^{-1}$) used in the rotational-state detection measurement (Sec. 2.7). This ensures that in both the effusive regime or the hydrodynamic regime of the buffer-gas cooling, the guided population of this molecule is predominantly in its lowest guidable state, the $|1, 1, 1\rangle$ state. Secondly, ND_3 has an inversion splitting of around $1.59\,GHz$. In a simplified classical picture, this is the frequency at which the nitrogen atom oscillates between the two sides of the plane formed by the three deuterium atoms. In the quantum mechanical description, this is the energy splitting between the two parity states $|+\rangle$ and $|-\rangle$, formed by a symmetric and an anti-symmetric superposition of the $|L\rangle$ and the $|R\rangle$ states, respectively. The $|L\rangle$ ($|R\rangle$) state corresponds to the N atom located at the left (right) side of the plane formed by the three D atoms. The hyperfine structure we have resolved is on top of this transition between the $|+\rangle$ and $|-\rangle$ states. Thirdly, the nuclear spin of the nitrogen-14 atom in ND_3 has spin $I = 1$, hence gives rise to the nuclear quadrupole coupling discussed in Sec. 2.8.1. Since $J = 1$ as mentioned earlier, F can be 2, 1, or 0. The relation between C and F given by Eq. 2.11 is summarized in Table 2.2. The frequency shifts to the transition between the two inversion-doublets, resulting from this hyperfine interaction can be derived from Eq. 2.10 and are summarized in Table 2.3.

F	2	1	0
2	0	-4Δ	6Δ
1	4Δ	0	10Δ
0	-6Δ	-10Δ	0

Table 2.3: *The frequency shifts to the transition between the inversion-doublets due to the hyperfine interaction from the nuclear quadrupole coupling of the nitrogen atom in ND_3. The first row and first column show the hyperfine quantum number of the initial and the final state, respectively. Each element of the matrix gives the frequency shift of the corresponding transition. $\Delta = \frac{3}{8}eQq_J$ according to Eq. 2.10.*
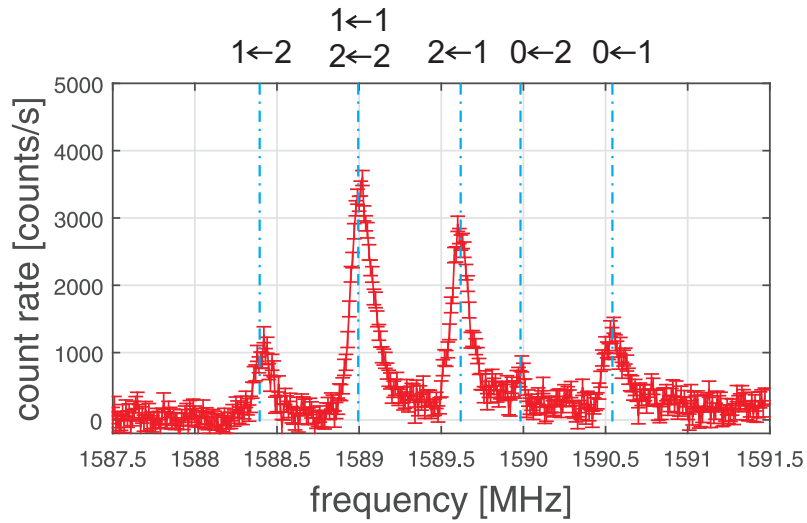

Figure 2.9: *Resolving the hyperfine structure in the transition for the about 1.6 GHz inversion splitting of ND_3. The blue dashed lines indicate the theoretical value of the hyperfine lines [63].*

The experimental conditions are presented in the following. The buffer-gas cell was operated at 17 K. Neon was used as buffer-gas with an input flow rate of 10 sccm, well in the hydrodynamic regime. ND_3 input line was kept at 215 K, and the flow rate was kept low, 0.005 sccm. The two parallel capacitor plates were both grounded, so the molecules passed through a field-free region between the plates. An RF signal around 1589 MHz was applied to the T-shaped structure on one of the capacitor plates. The frequency was scanned without applying white noise. The obtained depletion spectrum is shown in Figure 2.9, with the assignment of $F' \leftarrow F$ for each line labeled on top of the figure, where F' is the hyperfine quantum number of the final state.

A careful comparison between the spectrum shown in Figure 2.9 and the calculation shown in Table 2.3 provides insights into the hyperfine transitions. Based on the values listed in Table 2.3, 7 lines would be expected. However, maximally only 5 of the lines were observed in the spectrum. The reason is that the $F = 0$ level of the

$|1,1\rangle$ state has almost zero Stark-shift [63], and hence is hardly guidable. The nearly supersonic velocity distribution of the ND_3 beam eliminates the molecules initially populating the $F = 0$ state very quickly from the guide before they reach the capacitor plates. Therefore, transitions for $F' = 1, 2 \leftarrow F = 0$ are not present, and the remaining 5 lines can be found in Figure 2.9. The line at 1589.0 MHz is stronger because it consists of two contributions, $F' = 1 \leftarrow F = 1$ and $F' = 2 \leftarrow F = 2$, both of which possess zero correction to the inversion splitting. On the contrary, the $F' = 0 \leftarrow F = 2$ line is extremely weak because it is a dipole forbidden transition. In addition, the spacing between the 5 lines should obey the ratio $2 : 2 : 1 : 2$ from left to right, based on the values listed in Table 2.3. This agrees fairly well with the observation in Figure 2.9.

The line-width in Figure 2.9 is limited by the time-of-flight broadening. For a molecular beam moving at about 200 m/s (in the hydrodynamic regime), and a size of ~ 1 cm RF interaction region, the interaction time is $\sim 50\,\mu$s. This gives a TOF broadening of ~ 20 kHz. As a result, further improvements of this setup are necessary for observing higher order hyperfine interactions. The next nearest term is from the nuclear quadrupole coupling at the D atoms of ND_3, which possess also 1 nuclear spin each. The splitting produced by this interaction is $\lesssim 10$ kHz [63].

The easiest way to improve the line-width is to enlarge the interaction region. Given that the current setup was homemade on a simple PCB (see Figure 2.3), an extension of the capacitor plates along the molecular flow axis seems straightforward. One potential problem is that once the gap between the two electric guides become too large, the molecule signal would suffer from beam divergence in the free-flying region. This could be suppressed by including a horn-shaped molecular lens at the ends of the guides [41] for focusing and re-collecting the molecules. Alternatively, one can decelerate or translationally cool the molecular beams, as discussed thoroughly in Chapter 3 and 4.

2.9   Monte Carlo trajectory simulations

So far, we have only discussed the internal-state detection of molecules after the electric guiding. To characterize the buffer-gas source and to quantify the effect of buffer-gas cooling for different cell operating regimes, it is, however, necessary to determine the rotational-state and velocity distributions of the molecules upon emerging from the cryogenic buffer-gas cell. To retrieve this information from the measurements at the end of the guide, we have performed comprehensive Monte Carlo trajectory simulations, which yield the guiding efficiencies for the molecules in the quadrupole guide. In this section, we describe the basic principle and some crucial elements of the simulations.

The electric-field distribution along the entire molecule guide is calculated using the SIMION software package, and, on this basis, the molecular trajectories from the cell output to the QMS are simulated. In particular, this includes the two 20 cm-
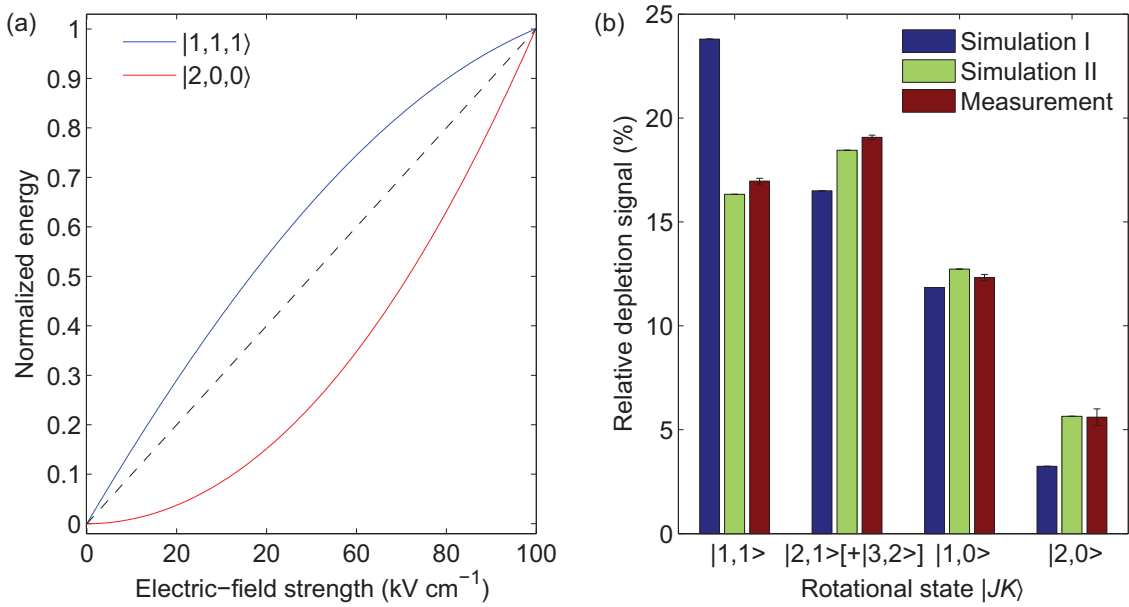
Figure 2.10: *(a) Normalized exact Stark-shift curves as a function of the electric field for states with different types of Stark-shift curvatures: convex ($|1, 1, 1\rangle$ rotational state of CH_3F) and concave ($|2, 0, 0\rangle$ rotational state of CH_3F). They were obtained based on diagonalizing the rigid-rotor Hamiltonian. The linear approximation to the Stark-shift curve is shown for comparison (black dashed line). (b) Demonstration of the necessity of using the exact Stark-shift curves: comparison between the relative depletion signals for simulation I, simulation II, and the measurement. The simulated depletion signals are taken at the fitted T_{rot}, with the fitting procedure explained in details in Section 2.10.1. The major difference between simulations I and II is that the former uses only linear approximations to the Stark curves while the latter uses the exact Stark curves. Very good agreement with the experimental results is obtained only for simulation II.*

radius 45-degree bends, the capacitor plates, and the divergence of the molecular beam between the end of the guide and the QMS, as shown in Figure 2.2(b). To determine the longitudinal velocity distributions, experiments and simulations are also performed for the case of a continuous guide, in which the capacitor plates are replaced by a straight piece of guide, as here the capacitor plates are not necessary. The effect of applying an RF field to the capacitor plates is simulated by evenly redistributing the population of a given $|J, K\rangle$ state across all of its M-sublevels in the middle of the capacitor. The ratio of the simulated signals with and without reshuffling the population across the M-sublevels gives the simulated depletion ratio.

In the following, we describe the initial conditions and the method for the trajectory simulations. The transverse spatial distribution of the molecules at the guide input is taken to be flat, and the transverse energy distribution is taken as the Boltzmann distribution ($\sim T_{cell}$) truncated by the transverse acceptance of the guide ($\sim 1K$ trap depth). The initial longitudinal velocity, $v_{\parallel}$, is varied, allowing

a guiding efficiency as a function of $v_\parallel$ to be extracted from the simulation. Dividing the measured $v_\parallel$-distribution after the guide by the corresponding guiding efficiencies yields the initial $v_\parallel$-distribution before the guide (see Figure 2.14(a)). Assuming this initial $v_\parallel$-distribution is the same for all internal states, we simulate the guiding efficiency for every relevant $|J, K, M\rangle$ state with the above-determined initial $v_\parallel$-distribution taken as an input. Once these state-dependent guiding efficiencies become available, we could recover the initial rotational-state distribution before the guide (see Figure 2.12(a)) from the depletion measurements described in Section 2.7. One subtlety here is that the simulations for the $v_\parallel$ distribution and for the rotational-state distribution need each other's results as their inputs. This interdependence can be resolved by realizing that the $v_\parallel$-dependent guiding efficiency is only weakly influenced by the state composition, and the two simulations can be performed iteratively. In practice, we start with a state distribution corresponding to the Boltzmann distribution at T_{cell} in order to determine the initial $v_\parallel$-distribution at the guide input. This in turn helps us calculate the theoretical depletion values for various states between the capacitor plates, assuming a Boltzmann distribution in the cell. By fitting the measured RF depletion data to the so-obtained theoretical values, we can determine the rotational temperature of the molecules exiting the cell. This last assumption of reaching a Boltzmann distribution in the cell at a fitted temperature is validated by the results shown in Section 2.10.1.

To achieve a good agreement between the simulated and the experimental results, a key requirement is to take into account the exact dependence of the Stark shift on the electric field, rather than using a linear or quadratic approximation. As shown in Figure 2.10(a), the Stark shift for certain states deviates strongly from a linear approximation for fields up to 100 kV/cm, as present in the experiment. Employing the exact Stark-shift curve dramatically improves the match between the measured and simulated depletion signal, as shown in Figure 2.10(b). In particular, including the exact Stark curve decreases the simulated depletion signal for states with a convex Stark shift and increases the simulated depletion signal for states with a concave one, with a less pronounced effect for states with a Stark shift more closely following a linear behavior, as might be expected.

Another useful development on the trajectory simulation is to simulate the trajectories in a three-dimensional quadrupole bend (Figure 2.11(a)) with only a two-dimensional electric field distribution (Figure 2.11(b)). Our simulation package is capable of taking both 3-D and 2-D electric field distributions. However, there are two problems with taking the 3-D electric field distribution of a bend quadrupole guide. Firstly, it is numerically costly to simulate a bend of large radius R at a high resolution (d grids per unit length). To have a higher resolution (i.e. higher value of d) is necessary to obtain a smoother spatial distribution of the electric-field and hence to avoid artifacts in the trajectory calculations. For simulating a bend with $R = 20\,\text{cm}$ (see Sec. 2.5) at $d = 50\,\text{grids/mm}$ is simulated, about 10^{10} grids are needed. This number scales with $\propto R^2 d^3$. Secondly, as visible in Figure 2.11(a), it is also very wasteful to have a great part of the empty geometry
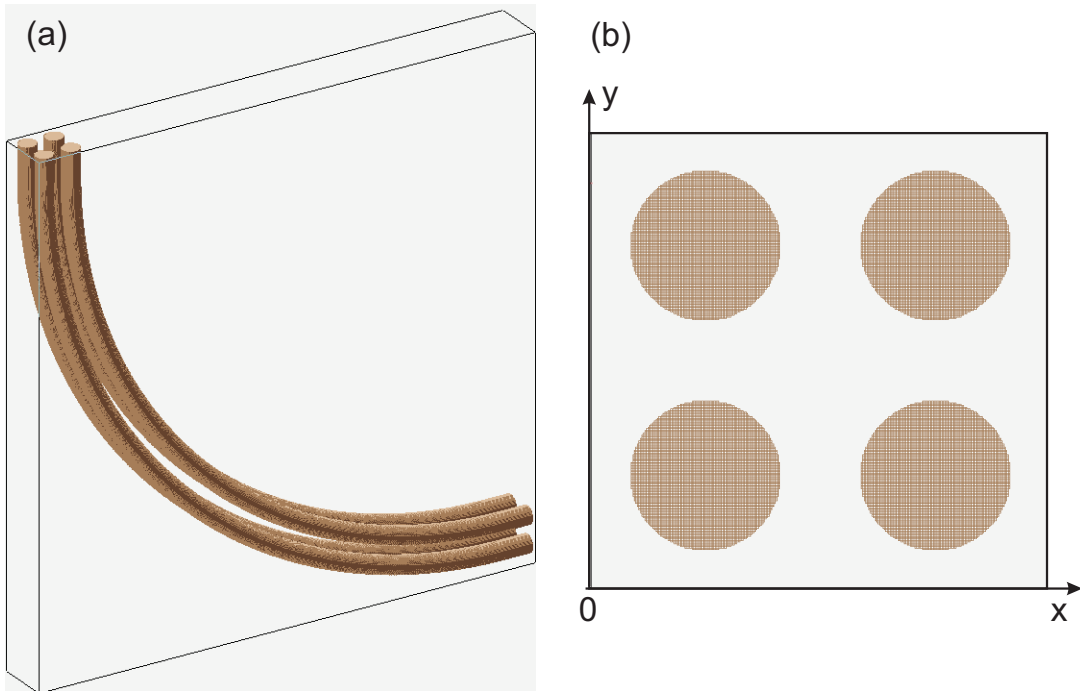
Figure 2.11: *Illustration of the geometry used to simulate a bent electric quadrupole guide. (a) Full geometry of a 90° bend, the quadrupole electrodes have a radius of $1\,mm$ and inter-electrode spacing of $1\,mm$. The radius of the bend in this illustration is only $5\,cm$. (b) A cross section of the bent quadrupole guide.*

outside the bend, which is not relevant for the trajectory calculation. Transforming the 3-D quadrupole bend into only a 2-D guide (Figure 2.11(b)) is possible due to the cylindrical symmetry of the bend. Subsequently, at each step of the trajectory simulation, only the electric-field distribution calculated from the 2-D structure (assuming translational symmetry) is stored in the memory. The potential energy $P.E$, of the molecule in the cylindrical coordinate system is

$$P.E.[x, y] = U[x, y] + \frac{1}{2}\frac{L^2}{\mathcal{R}^2}, \tag{2.12}$$

where the molecular mass is normalized, $P.E.[x, y]$ is the total potential energy distribution in the x-y coordinate system, $U[x, y]$ is the potential energy distribution for a straight electric quadrupole guide, L is the angular momentum of the molecule calculated from its initial position and velocity, and $\mathcal{R} = R + y_0 - y$ is the radial position in the cylindrical coordinate system with y_0 being the distance from the top boundary to the center of the quadrupole in Figure 2.11(b). The second term on the right-hand side of Eq. 2.12 is simply the centrifugal potential of the molecule inside the system. Making this transformation has saved an enormous amount of memory when performing the trajectory simulation.
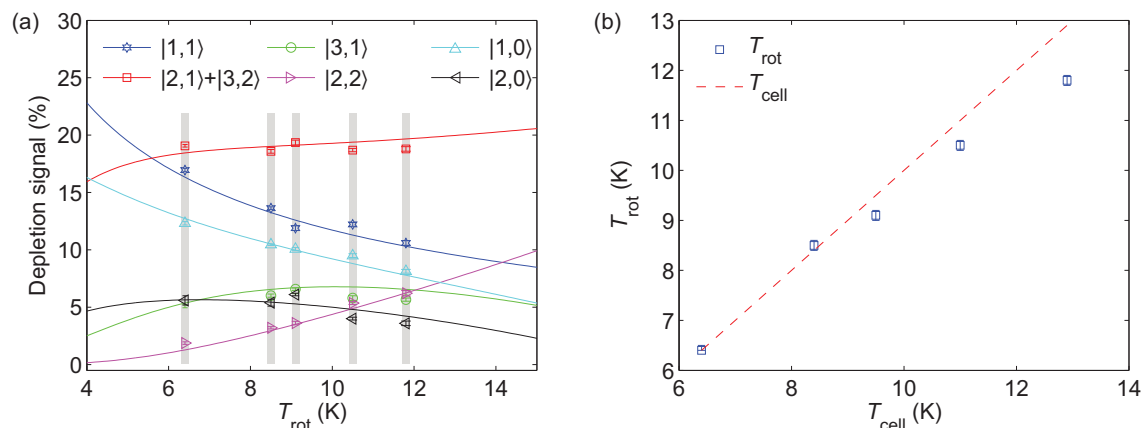
Figure 2.12: *(a) Measured depletion signals (data points) for different rotational states $|JK\rangle$ of CH_3F and different buffer-gas cell temperatures at a fixed He flux of $\Phi_{He} = 2 \times 10^{17}\,s^{-1}$ and simulated depletion signals (lines) for different rotational temperatures for different rotational states. The grey columns group sets of measurements performed at the same T_{cell}. Measurements at five different cell temperatures have been performed. The rotational temperature of the molecules leaving the buffer-gas cell was determined by columnwise simultaneous fitting of the measured depletion signals to the calculated curves. (b) Relation between the measured cell temperature, T_{cell}, and the fitted rotational temperature, T_{rot}, for CH_3F at a fixed helium flux.*

2.10   Analysis and discussion

Sections 2.7 and 2.9 have described the measurement and the simulation methods. In this Section we apply these tools for a comprehensive characterization of the buffer-gas-cooling process in the cryogenic cell. First, we explore in Sections 2.10.1 and 2.10.2 the influence of cell parameters on the buffer-gas cooling. Next, we investigate in Sections 2.10.3 and 2.10.4 the cooling of different molecular species and in the supersonic operating regime of the cell. At the end, in Sections 2.10.5 and 2.10.6 we discuss and draw conclusions on the cooling effect for different degrees of freedom and for different rotational states.

2.10.1   Rotational temperature vs. cell temperature

The first property we study is the dependence of the rotational temperature on the cell temperature. Here, we would like to address two questions: first, whether the rotational states of molecules obey a Boltzmann distribution in the cell; second, how T_{rot} compares to T_{cell}. Figure 2.12(a) shows the measured depletion (in percentage of the total signal) for different rotational states $|J, K\rangle$ of CH_3F for different cell temperatures, T_{cell}, along with their theoretical predictions (solid curves). The measurements were done at a fixed He flux of $\Phi_{He} = 2 \times 10^{17}\,s^{-1}$ (corresponding to a density of $n_{He} = 1.6 \times 10^{15}\,cm^{-3}$ at $T_{cell} = 6.4\,K$ for our cell geometry). The data for

each T_{cell} are grouped in a separate vertical column in Figure 2.12(a). The theory curves are based on the assumption of a Boltzmann distribution for the rotational states at the cell (as mentioned in Section 2.9), with T_{rot} being an independent variable on the horizontal axis. The guiding efficiencies are simulated using the method described in Section 2.9. In particular, we have included all 64 guidable $|JKM\rangle$ states of CH_3F (rotational constants $A = 155\,\text{GHz}$ and $B = 26\,\text{GHz}$), with rotational energies below $72\,\text{K}$. For a source at $10\,\text{K}$ those states account for $99.7\,\%$ of the thermal population. Note that T_{rot} is the only fit parameter in Figure 2.12(a), which sets the horizontal position of each column via a least-χ^2 fit to the theory curves. The good agreement between measurement and theory confirms the assumption that a Boltzmann distribution is reached for the rotational states in the cell, at the He flux applied in this particular measurement. Moreover, the plot in Figure 2.12(b) also shows a relatively good agreement between T_{rot} and T_{cell}. This, however, is not a universal effect, but rather a consequence of the applied He flux. In fact, as will be shown in the next section, by varying the He density in the cell, we also vary T_{rot}.

2.10.2 Rotational temperature vs. buffer-gas density

Next, we would like to discuss the relation between rotational temperature and the buffer-gas density in the cell. As already pointed out qualitatively (see Section 2.7), increasing the buffer-gas density in the cell increases the cooling capacity, and, consequently, results in a better cooling of the molecules. To quantify this effect, we determined the rotational temperature of CH_3F for different He densities ranging from $2.2 \times 10^{14}\text{cm}^{-3}$ to $7.1 \times 10^{15}\text{cm}^{-3}$ at a fixed cell temperature of $T_{\text{cell}} = 6.4\,\text{K}$. The dependence is plotted in Figure 2.13(a) (red squares). We observe cooling of rotational states to near the cell temperature for minimal He density below $1 \times 10^{15}\text{cm}^{-3}$ for our cell geometry. It is also particularly interesting to note that for buffer-gas densities above $2 \times 10^{15}\text{cm}^{-3}$, the rotational temperature of the CH_3F molecules leaving the cell is lower than the cell temperature. This evidences further cooling as a result of the adiabatic expansion of the gas upon streaming out of the cell [56, 64]. The higher the buffer-gas density, the stronger the effect of the adiabatic cooling. For a He density of $7.1 \times 10^{15}\text{cm}^{-3}$, the rotational temperature is determined to be $(4.2 \pm 0.1)\,\text{K}$.

2.10.3 Cooling of a heavier molecule

The dependence of the cooling process on the molecular species is also investigated. Here we cool the rotational degrees of freedom of a heavier molecule, 3,3,3-trifluoropropyne, CF_3CCH (mass $m = 94\,\text{u}$, rotational constants $A = 5.7\,\text{GHz}$ and $B = 2.8\,\text{GHz}$), and compare the results with those for CH_3F. The at least 10-fold decrease in energy spacing ($\propto A$, B) for CF_3CCH compared to that of CH_3F not only greatly reduces the signal per state in the measurement, but also requires more
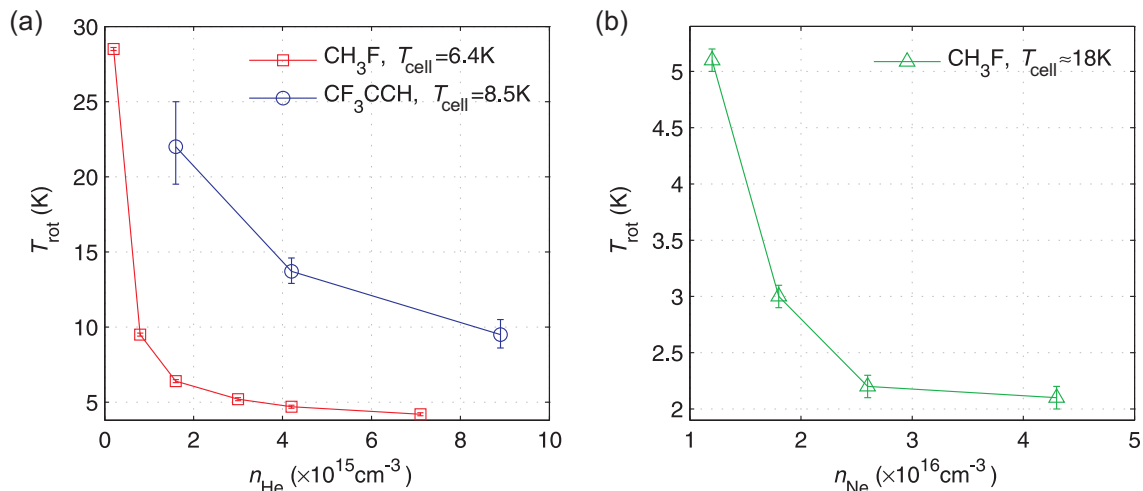
Figure 2.13: *(a) Rotational temperatures of two molecular species,* CH_3F *and* CF_3CCH, *as a function of the He buffer-gas density in a cell operated in the boosted regime. The cell temperatures were kept constant,* $6.4\,K$ *and* $8.5\,K$, *for* CH_3F *and* CF_3CCH, *respectively. (b) Rotational temperature of* CH_3F *as a function of the Ne buffer gas in a cell operated in the supersonic regime. The cell temperature was kept fixed at* $18\,K$.

energy levels to be included in the simulation. In this case we have performed trajectory simulations including the exact Stark curves for all 2869 guidable $|JKM\rangle$ levels below 72 K (corresponding to 99.7% thermal population at 10 K). We have derived the rotational temperature of CF_3CCH for different He densities in a similar range as for CH_3F, from $1.6 \times 10^{15}\mathrm{cm}^{-3}$ to $8.9 \times 10^{15}\mathrm{cm}^{-3}$, and for a fixed buffer-gas cell temperature of $T_{\mathrm{cell}} = 8.5\,K$, as shown in Figure 2.13(a) (blue circles). The higher cell temperature in this case results from the maintained higher temperature of the molecule feed line, as CF_3CCH has a considerably higher freezing point than CH_3F. The trend of better cooling for higher buffer-gas densities is clearly observed. Nevertheless, even for the largest He density applied here, the rotational temperature remains slightly above the cell temperature, i.e., the molecules are not fully thermalized. Various effects play a role in determining the thermalization rate. A possible reason for the worse cooling of the rotational degrees of freedom for CF_3CCH compared to CH_3F for similar buffer-gas densities includes the larger density of rotational states populated by CF_3CCH requiring more collisions to thermalize.

2.10.4 Rotational temperatures in the supersonic regime

In Sec. 2.7.2 we discussed buffer-gas cooling in the supersonic regime qualitatively. Here, our simulation toolbox provides a quantitative study on the rotational temperature of the CH_3F cooled in the supersonic regime. The supersonic beams are formed when a large number of collisions take place near the cell nozzle during expansion into a vacuum. During this process, the particles convert their internal
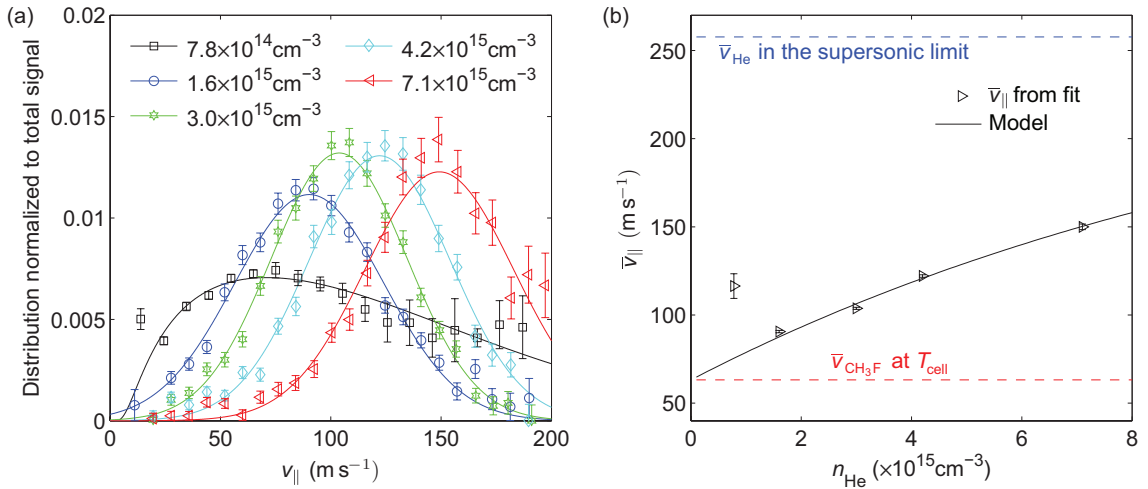
Figure 2.14: *(a) Derived longitudinal velocity distribution for* CH_3F *at the input of the guide for* $T_{cell} = 6.4\,K$ *and different He densities, along with their fits. (b) Mean longitudinal velocity,* $\bar{v}_{\parallel}$, *from the fits as a function of the corresponding* n_{He}. *The solid curve is based on a momentum transfer model described in the text.*

energy into a kinetic one whereby they get colder [32]. In this case, we used Ne as a buffer gas since at $T_{cell} = 18\,K$ it has a supersonic flow speed below $200\,\mathrm{m\,s^{-1}}$, lower compared to the supersonic flow velocity of He at $6\,K$, which makes guiding feasible. The other benefit of using Ne is the better pumping of the background gas. The dependence of the measured rotational temperature, T_{rot}, as a function of the buffer-gas density is shown in Figure 2.13(b). Here we demonstrate that the supersonic expansion leads to a reduction of the rotational temperature by almost an order of magnitude below the cell temperature, allowing us to cool molecules down to $(2.1 \pm 0.1)\,K$.

2.10.5   Rotational vs. translational temperatures

Our toolbox is able to characterize not only the rotational-state distribution of the molecules emerging from the cell, but also their longitudinal velocity distribution ($v_{\parallel}$-distribution). This enables the measurement of the translational temperature, and its comparison to the rotational one. The procedure of deducing the $v_{\parallel}$-distributions at the cell output is explained in Section 2.9. Figure 2.14(a) shows the $v_{\parallel}$-distributions of CH_3F for the same cell parameters as those used in the T_{rot} measurement in Section 2.10.2. The solid curves in Figure 2.14(a) are fits to the distributions. Gaussian fits centred at peak velocities have been applied to all but the lowest-density distribution ($n_{He} = 7.8 \times 10^{14}\,\mathrm{cm^{-3}}$). The latter has been fitted with a Maxwell distribution corrected for the boosting effect [49]. The use of a different fit function is substantiated by the quantitative model below.

To further analyze the changes in the $v_{\parallel}$-distribution, we plot in Figure 2.14(b)

the mean longitudinal velocity, $\bar{v}_\parallel$, as a function of n_{He}. The value of $\bar{v}_\parallel$ is extracted from the fits in Figure 2.14(a). Its increase at higher n_{He} is understood to result from collisions between molecules and He atoms in the vicinity of the nozzle [50]. The lighter He atoms move at a higher speed and kick the heavier molecules from behind whereby the molecules get accelerated in the forward direction. To quantify this effect, we have built the following model based on the momentum transfer for elastic collisions. From conservation of energy and momentum, the change in the molecules' velocity per head-on collision is $\Delta v_\parallel = \beta(v_{He} - v_\parallel)$, where $\beta = \frac{2m_{He}}{m_{mol}+m_{He}}$ with $m_{mol(He)}$ being the mass of the molecule (He atom), and v_{He} is the longitudinal velocity of the He atom. As the He density in the nozzle region is typically much higher than the molecule density, we assume v_{He} to be constant and approaching the supersonic velocity, which sets the upper bound for the mean velocity of He in the limit of high density [32]. This leads to $v_\parallel(l) = \bar{v}_{He} - (\bar{v}_{He} - v_0)exp(-\beta l)$, where l is the number of head-on collisions in the molecular-beam direction, $\bar{v}_{He}$ is the centre velocity of a He supersonic beam at T_{cell}, and v_0 is the initial longitudinal velocity of the molecules. l is related to n_{He} by $l = dg\sigma n_{He}$, where $d = 2$mm is the nozzle diameter setting a rough estimate of the distance where collisions take place, σ is the CH_3F-He elastic collision cross-section, and g is a proportionality factor on the order of unity taking into account the fact that only collisions in the direction normal to the nozzle plane contribute to the change in $v_\parallel$. Assuming the molecules have translationally thermalized to T_{cell} before arriving at the nozzle, and hence v_0 is approximately their thermal mean velocity at T_{cell}, our model (the solid curve in Figure 2.14(b)) describes very well the dependence of $\bar{v}_\parallel$ with respect to n_{He} with the exception of the lowest-density point. The only fit parameter in the model is $g\sigma = 2.0 \times 10^{-15}\,cm^2$, which agrees within one order-of-magnitude with the typical CH_3F-He collision cross-section at this temperature range [65]. Moreover, the fact that the lowest-density data stays above the model curve shows that the translational degree of freedom of molecules is not yet thermalized to T_{cell} at this point, in line with the finding in the T_{rot} measurement at low He densities (see Section 2.10.2). This also justifies using a different fit function for the lowest-density $v_\parallel$-distribution (Figure 2.14(a)).

In the following we discuss the translational temperature of molecules, T_{tr}, and compare it to the rotational one. While the width of a Gaussian fit to the $v_\parallel$-distribution defines T_{tr} in the high-density limit, where molecular beams approach the supersonic regime, it provides only a lower bound to T_{tr} in the low-density limit where a Maxwellian distribution describes $v_\parallel$ better, as shown in Figure 2.14(a). Thus we assign a lower bound to T_{tr} of $15.7 \pm 1.7\,K$ for the distribution at $n_{He} = 7.8 \times 10^{14}\,cm^{-3}$ based on its width, while its mean kinetic energy corresponds to $28 \pm 3\,K$. In comparison, T_{rot} at this density is found to be $9.5 \pm 0.1\,K$ (the second point in Figure 2.13), which is clearly lower than the value of T_{tr}. Having a colder T_{rot} than T_{tr} might not be surprising for the given system because of the large mass imbalance between CH_3F and He, which makes cooling of the centre of mass motion inefficient. On the other hand, the $v_\parallel$-distribution for the highest density in
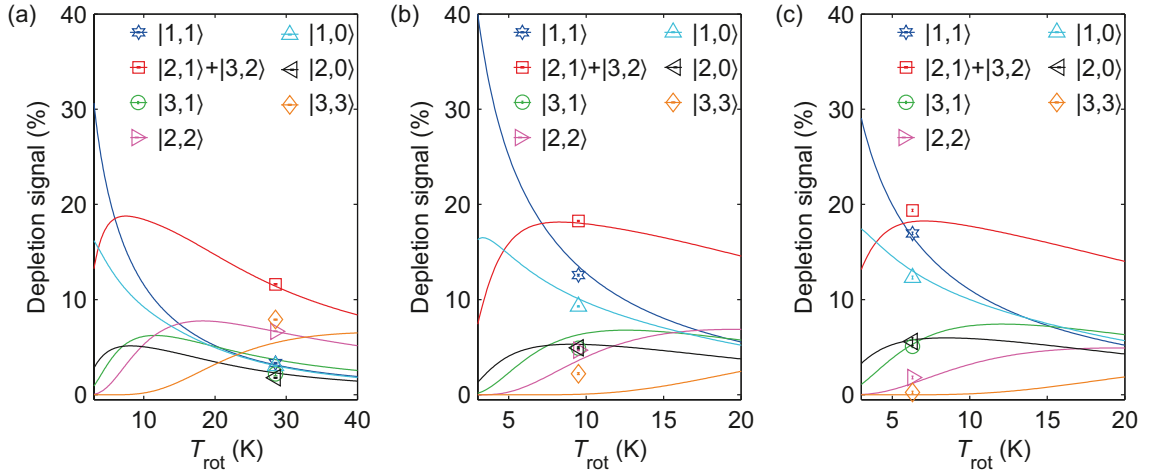
Figure 2.15: *Measured depletion signals (data points) for different rotational states of* CH_3F *and different He densities, (a)* $n_{He} = 2.2 \times 10^{14} cm^{-3}$, *(b)* $n_{He} = 7.8 \times 10^{14} cm^{-3}$, *and (c)* $n_{He} = 1.6 \times 10^{15} cm^{-3}$, *at a fixed cell temperature* $T_{cell} = 6.4\,K$, *and simulated depletion signals for different rotational states and different rotational temperatures (lines) for each of the applied He densities.*

Figure 2.14(a) ($n_{He} = 7.1 \times 10^{15}\,cm^{-3}$) has a width corresponding to $4.7 \pm 0.4\,K$, which is very similar to $T_{rot} = 4.2 \pm 0.1\,K$ found in Section 2.10.2. Presumably, in the high-density limit, T_{tr} and T_{rot} should converge due to the sufficient number of collisions.

2.10.6 Rotational-state-dependent thermalization rates

In Section 2.10.2 we have investigated the dependence of fitted T_{rot} on the He density in the cell. In this Section we take a closer look at the state distribution in the low He density limit. Figure 2.15 shows a comparison between the measured depletion signals and the corresponding theory curves in increasing order of He density, $n_{He} = 2.2 \times 10^{14} cm^{-3}$, $7.8 \times 10^{14} cm^{-3}$, and $1.6 \times 10^{15} cm^{-3}$ and at $T_{cell} = 6.4\,K$, corresponding to the first three points of the CH_3F data in Figure 2.13(a). Similarly to Figure 2.12(a), the data are grouped in columns, and the only fit parameter is the horizontal position of the column, which determines T_{rot}. Here, the data has to be split up into different graphs because the $v_\parallel$-distribution and therefore the theory curves (solid lines) differ for different buffer-gas pressure. The results clearly demonstrate that with increasing He density, the rotational states are better thermalized, and the fitted T_{rot} approaches T_{cell}. Moreover, at lower He density, the larger deviation between the measured depletion signals and the theoretical curves also indicates that the internal states are not fully thermalized. In particular, we would like to point out that the depletion signals for the $|3,3\rangle$ state (orange diamonds in Figure 2.15) appear far above their theoretical curves, and would correspond to a much higher rotational temperature if the $|3,3\rangle$ state were fitted alone. This is

an indication that the $|3, 3\rangle$ state thermalizes more slowly than the other states. Based on nuclear spin statistics, states with K being a multiple of 3 (ortho-CH$_3$F) are not interconvertible with states of K not being a multiple of 3 (para-CH$_3$F) [62] via buffer-gas collisions. Hence, CH$_3$F from the $|3, 3\rangle$ state can only relax to states with $K = 0$. Since the rotational energy scales as K^2, a transition of the type $K = 0 \leftarrow K = 3$ requires 3 times more energy to be taken away than a transition of the type $K = 1 \leftarrow K = 2$ does. Thus we attribute the above-observed effect to the larger energy difference between the initial and the final state, which makes the $|3, 3\rangle$ state thermalize at a lower rate than the other probed states.

2.11   Summary

We have developed a versatile and robust method for internal-state detection and thermometry of cold polyatomic molecules emerging from a cryogenic buffer-gas source. The detection method via resonant radio-frequency depletion is capable of addressing $100\,\%$ of the molecular population, as well as resolving their hyperfine states. The rotational and translational thermometry consists of three independent tools, time-of-flight measurements yielding the longitudinal velocity distribution, the above mentioned rotational-state-selective detection of guided molecules, and a complete Monte-Carlo simulation package resolving the guiding efficiencies for all present states.

The obtained results make possible the full characterization of buffer-gas sources and provide insight into the cooling processes in a cryogenic cell operated in different regimes. Studying those mechanisms, we have established an efficient control over the rotational and translational cooling of guided molecular beams by tuning the buffer-gas-cell temperature and the buffer-gas density. We have demonstrated rotational cooling below the cell temperature for the strongly boosted and supersonic regimes, achieving rotational temperatures more than an order of magnitude lower than the cell temperature. Interesting physical phenomena have also been observed. Comparing the rotational with the translational temperature, we have shown evidence of faster thermalization of the rotational degrees of freedom for the CH$_3$F-He collisions at the limit of low n_{He}. We have also observed manifestations of rotational-state-dependent cooling rates, and we have provided an explanation of this effect.

The presented detection and thermometry method is a very general one, which can be applied to a vast variety of molecules. It is particularly useful for probing cold molecules that are not amenable to other techniques, e.g., LIF or REMPI. Moreover, the thorough understanding of the cooling mechanisms in a cryogenic buffer-gas cell, provided by the new method, is the key to optimizing the production of internally and translationally cold molecules.

Chapter 3

Principle and design of the centrifuge decelerator

In Chapter 2, we have presented a new method for internal-state detection and thermometry of cold polyatomic molecules. It enables a full characterization of buffer-gas-cooled molecular beams, and, on this basis, various aspects of buffer-gas cooling can be studied. To apply the so-produced molecular beams as a source for various experiments, e.g. collision studies, cold chemistry, high precision measurements, or simply as a step to further cooling of molecules [38, 40], however, we still need to slow them down to almost a standstill. In this chapter, we discuss a novel approach for particle deceleration, by employing the centrifugal potential in a rotating frame.

This chapter is organized in the following way. Firstly, the principle of centrifuge deceleration, and the analysis in both the rotating and the laboratory frame are discussed in Sec. 3.1. Secondly, the deceleration effects, including the final velocities, the velocity spreads, and the relation to phase space densities are discussed in Sec. 3.2. The design of the centrifuge decelerator that enables the deceleration of continuous beams is presented in Sec. 3.3. The methodology for optimizing the guiding efficiency of the guide on the rotating disk and the resulting shape of the guide are described in Sec. 3.4. Next, the technical realization of the rotating electric guide and the numerical simulation of the overall efficiency are summarized in Sec. 3.5. Finally, the complete assembly of the centrifuge decelerator is presented in Sec. 3.6.

3.1 Basic principle

A basic idea for decelerating a particle is to make it climb up a potential hill thereby transforming its kinetic energy into potential energy. If the height of the potential hill matches exactly the kinetic energy of the incoming particle, the particle will be brought to a standstill upon arriving at the top of the hill. Following this concept, one could, in principle, employ the gravitational field of the Earth to decelerate

molecules from a cryogenic buffer-gas source. If, for example, a molecule with a velocity of 200 m/s is shot upwards, it will stop at an elevation of 2000 m.

To reconcile this deceleration approach with the length scale of a typical laboratory, one needs much stronger interaction than the one provided by the Earth gravitation. Here, we present an elegant and non-conventional solution, which employs a non-inertial system, in particular, harnesses the centrifugal force in a rotating frame (Fig.3.1) [66]. As this principle is independent of the detailed structure of a particle (be it a molecule, an atom, or even a neutron), the method can be generally applied, as long as the particle can be guided.

The centrifugal potential energy which is responsible for the deceleration in the rotating frame, is given by (details see Section 3.1.1)

$$E_{\text{centrifugal}} = -\frac{m}{2}\left(\vec{\Omega}\times\vec{r}\right)^2, \tag{3.1}$$

where m is the mass of the particle, $\vec{\Omega}$ is the angular velocity of the rotating frame, and $\vec{r}$ is the radial vector pointing from the center of the rotation to the position of the particle (Fig.3.1). A particle traveling from the periphery ($r = R$, the radius of the rotating disk) to the center of a rotating frame ($r = 0$) climbs up a potential hill of $\Delta E = m\Omega^2 R^2/2$. This equals the decrease of particle' s kinetic energy.

3.1.1   Dynamics in the rotating frame

This section summarizes important results from classical mechanics for a particle in a rotating frame.

The Lagrangian of a particle traveling inside a rotating frame (Fig.3.1(a)) is given by

$$L = \frac{m\vec{v}^2}{2} + m\vec{v}\cdot\left(\vec{\Omega}\times\vec{r}\right) + \frac{m}{2}\left(\vec{\Omega}\times\vec{r}\right)^2 - U, \tag{3.2}$$

where $\vec{v}$ is the velocity of the particle in the rotating frame, $\vec{\Omega}$ is the angular velocity, and U is the corresponding confining potential of the particle. For molecules, this is the electrical guiding potential (given by Eq. 2.4 for molecules experiencing linear Stark-shifts in an electric guide). In addition, the second and the third terms in Eq.3.2 represent the Coriolis and the centrifugal energies, respectively.

The momentum of the particle in the rotating frame is given by

$$\vec{p} = \frac{\partial L}{\partial \vec{v}} = m\vec{v} + m\left(\vec{\Omega}\times\vec{r}\right), \tag{3.3}$$

and hence the total energy of the particle in the rotating frame

$$E = \vec{p}\cdot\vec{v} - L \tag{3.4}$$

$$= \frac{m\vec{v}^2}{2} - \frac{m}{2}\left(\vec{\Omega}\times\vec{r}\right)^2 + U. \tag{3.5}$$

The second term in Eq.3.5 is the centrifugal potential in the rotating frame. The conservative potential U is independent of the rotating frame, and only contributes to the confinement and guiding of molecules but not to the deceleration process.
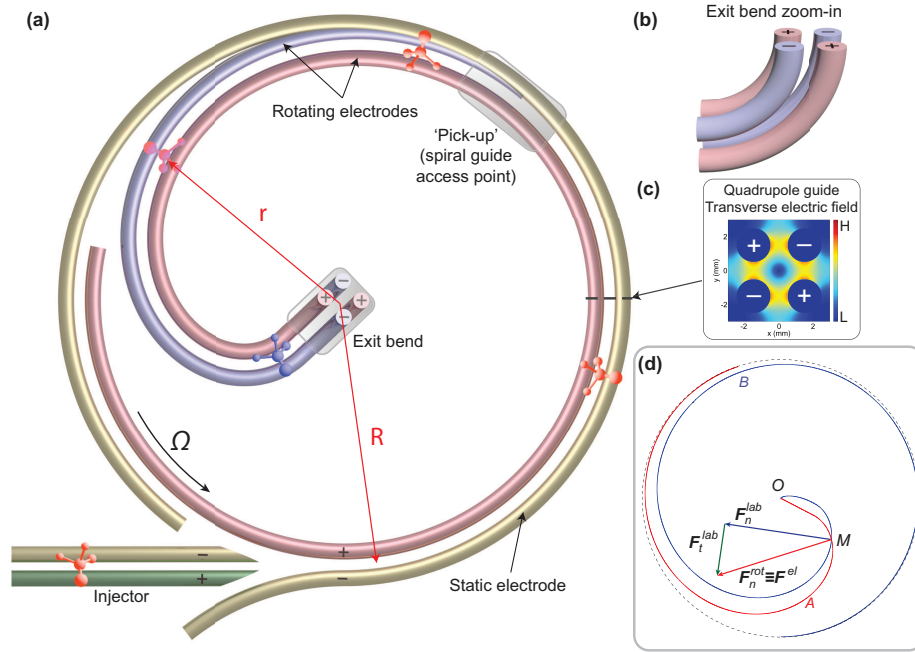
Figure 3.1: *(a) Centrifuge decelerator, top view. Molecules enter from the injector, propagate through the periphery guide and the rotating spiral, before coming out from the exit bend at the center of the rotation. The radius $R = 20cm$. (b) Zoom-in of the exit bend. It bends up by $90°$ from the rotating plane, so that the decelerated molecules leave the decelerator along the axis of rotation. The radius of curvature of the exit-bend is 5 about cm.(c) Transverse E-field distribution of the periphery guide, in a quadrupole configuration. Color bar labels L and H stand for low and high electric field. (d) Force diagram explaining the origin of the deceleration force in the lab frame (for details, see Sec. 3.1.2). Red curve A: spiral-shaped quadrupole guide ('longitudinal' molecular trajectory in the rotating frame) rotating with an angular velocity $\vec{\Omega}$ about the axis O; blue curve B: trajectory in the laboratory frame for a given molecule's input velocity v_{in} and a centrifuge angular velocity $\vec{\Omega}$.*

3.1.2 Dynamics in the laboratory frame

The centrifugal potential brings about the deceleration in the rotating frame, as outlined in Sec. 3.1.1. In the laboratory frame, however, it is the electric confining force from the spiral-shaped guide that does the deceleration. (For decelerating particles other than molecules, it would be the corresponding confining force that guides them.) This is not surprising since the force exerted by the guide is the only physical force experienced by a molecule in the decelerator.

Figure 3.1(d) illustrates the force diagram in the lab frame. The red and the

blue curves represent molecule's 'longitudinal' trajectory[1] in the rotating and in the lab frame, respectively. The former is identical to the central line of the guide by definition. The latter is simply a superposition of the former with a rotation at the constant speed Ω. The intersection of the two curves represents the instantaneous position of the particle. At a point M along the trajectory, the electric trapping force $\mathbf{F}^{el}$ exerted on the molecule is perpendicular to the quadrupole guide, or equivalently to the red curve in the figure, hence also labeled as $\mathbf{F}_n^{rot}$. $\mathbf{F}_n^{rot}$ can be decomposed into $\mathbf{F}_n^{lab}$ and $\mathbf{F}_t^{lab}$, the normal and the tangential components, with respect to the trajectory in the lab frame (the blue curve). $\mathbf{F}_t^{lab}$ is non-zero and anti-parallel to the particle's propagation, since the trajectory is a spiral and not a circular one. Therefore, $\mathbf{F}_t^{lab}$ decelerates the molecule in the lab reference frame. In other words, if there is no external power to drive the rotation of the guide, and if the bearings were frictionless, the molecular beam would push the guide to rotate in the direction of $\vec{\Omega}$.

3.2   Deceleration effects

Our design of the centrifuge decelerator enables a two-fold deceleration. One part is the subtraction of kinetic energy by a centrifugal potential, as discussed in Sec. 3.1. The other part comes from a velocity subtraction when molecules transit from the lab frame onto the rotating frame, given by

$$\vec{v}_{lab} = \vec{v} + \vec{\Omega} \times \vec{R} \tag{3.6}$$

$$= \vec{v} + \vec{v}_{periphery}, \tag{3.7}$$

where $\vec{v}_{lab}$ and $\vec{v}$ are the particle's velocities in the lab and in the rotating frame, respectively. $\vec{v}_{periphery}$ is the peripheral velocity of the rotating electrodes. The latter happens along the circular periphery guide of the decelerator, and is similar to the principle employed in the counter-rotating nozzle experiments [30, 31].

After the particles transit into the rotating frame, they are guided from the periphery to the center, where the centrifugal potential comes into play. The output velocity from the centrifuge decelerator v_{output} is the same in both the lab frame and the rotating frame, since the particles exit along the axis of rotation, as shown in Fig. 3.1(a) and (b). The value of the output velocity can be derived from the conservation of energy, with the energy expression given in Eq.3.5 and velocity transformation given in Eq.3.7,

$$\frac{m\vec{v}_{output}^2}{2} - \frac{m}{2}\left(\vec{\Omega} \times 0\right)^2 = \frac{m(\vec{v}_{lab} - \vec{v}_{periphery})^2}{2} - \frac{m}{2}\left(\vec{\Omega} \times \vec{R}\right)^2 \tag{3.8}$$

$$\Rightarrow \quad v_{output} = \sqrt{v_{lab}^2 - 2v_{lab}v_{periphery}}, \tag{3.9}$$

---

[1] Molecules can certainly oscillate in the transverse direction inside the quadrupole guide while propagating forward. What is shown is only the projection of their trajectories onto the tangential direction of the guide.
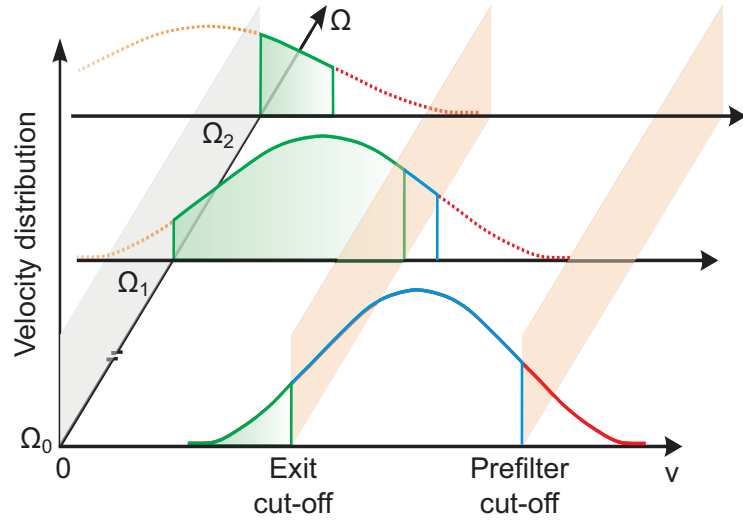
Figure 3.2: *Illustration of the three different regimes of deceleration. The right and left vertical planes indicate the cut-off velocities in the periphery guide ($R = 20$ cm), and in the exit-bend ($R' \approx 5$ cm) at the center of the rotation, respectively.*

or,

$$v_{output} = \sqrt{v_{lab}^2 - 2v_{lab}\Omega R}. \tag{3.10}$$

3.2.1 Three regimes of deceleration

As the angular speed of the rotating frame Ω is tunable, three different regimes can be identified from Eq.3.9, and are illustrated in Fig. 3.2.

- Too slow rotation: If $\Omega_0 R = v_{periphery} \ll v_{lab}/2$, Eq.3.9 gives

$$v_{output} = v_{lab} \left(1 - \frac{2v_{periphery}}{v_{lab}}\right)^{1/2} \approx v_{lab} - v_{periphery} \approx v_{lab} \tag{3.11}$$

This means when the rotation is too slow, the deceleration is negligible. This is illustrated by the Ω_0 curve (the lower one) in Fig. 3.2. The area under the red curve is lost already along the periphery, and the part under the blue curve is not able to make through the exit-bend. Only the part under the green curve reaches the output. Thus, without much rotation, the signal at the centrifuge output is low.

- Optimized rotation: if the rotating frame spins right below half of the particle's velocity in the lab frame

$$\Omega R = v_{periphery} \lesssim v_{lab}/2, \tag{3.12}$$

the particle can be decelerated down to $\approx 0\,\text{m/s}$, as derived from Eq.3.9. This is the optimized rotation speed, as illustrated approximately by the Ω_1 curve (the middle one) in Fig. 3.2.

- Too fast rotation: If $\Omega R = v_{periphery} > v_{lab}/2$. It can be easily verified that the kinetic energy of the particle in the rotating frame $mv^2/2 = m(v_{lab} - v_{periphery})^2/2$ is less than the centrifugal potential hill $\Delta E = \frac{1}{2}m\Omega^2 R^2$. This means particles are repelled back by the centrifugal potential before they can reach the center of the rotating frame, hence gaining negative velocities. As illustrated by the Ω_2 curve (the upper one) in Fig. 3.2, the majority of the velocity distribution is below $0\,\text{m/s}$ (under the orange color dashed curve), and the output signal (the green area) is low.

In summary, to set $\Omega \lessapprox \frac{1}{2}v_{lab}/R$ should be a rule of thumb when operating the centrifuge decelerator.

3.2.2 Phase-space density

Next, we take a look at the influence on the number density, velocity spread, and phase space density. As discussed earlier, the centrifuge decelerator only subtracts the velocity (on the periphery) and the kinetic energy (in the rotating spiral), and both steps conserve the phase space density according to Liouville's theorem. The first step results in a shift of the whole input velocity towards $0\,\text{m/s}$ by an amount equal to the peripheral velocity. Both the width of the velocity distribution and the number density remain the same, while the flux of molecules is not conserved at this transition. In the second step, where kinetic energy (not velocity!) is subtracted and transformed into potential energy, the total flux is conserved, which entails compression of position density with decreasing molecules' velocity. To satisfy Liouville's theorem, the velocity spread must increase. Fig. 3.3 shows clearly this effect.

Figure 3.3 represents a numerical calculation for an example of decelerating molecules with input velocities v_{lab} around $200\,\text{m/s}$. The radius of the rotating disk is $20\,\text{cm}$. As suggested by Eq.3.12, we need $v_{periphery} \lessapprox v_{lab}/2 = 100\,\text{m/s}$ for optimized deceleration. Thus, we operate the rotating disk at $\Omega = 78\,\text{Hz}$. In Fig.3.3, we plot the velocity of the molecules inside the rotating frame as a function of both the input velocity v_{lab} (the vertical axis on the right) and the radial distance to the center of the rotating frame (x-axis). The curves of different colors in Fig.3.3 indicate the velocity decreases of molecules with different input velocities. They have hyperbolic shapes, as expected from Eq.3.9.

3.2.3 Acceptance window

Figure 3.3 also helps us to track the acceptance window of the input velocity distribution for a desired output velocity interval. For example, the depths of most molecular trap is $\sim 1\,\text{K}$. For CH_3F (m=34 u), this corresponding to $v_{output} \sim 20\,\text{m/s}$

Velocity of molecules as a function of both radial distance r and
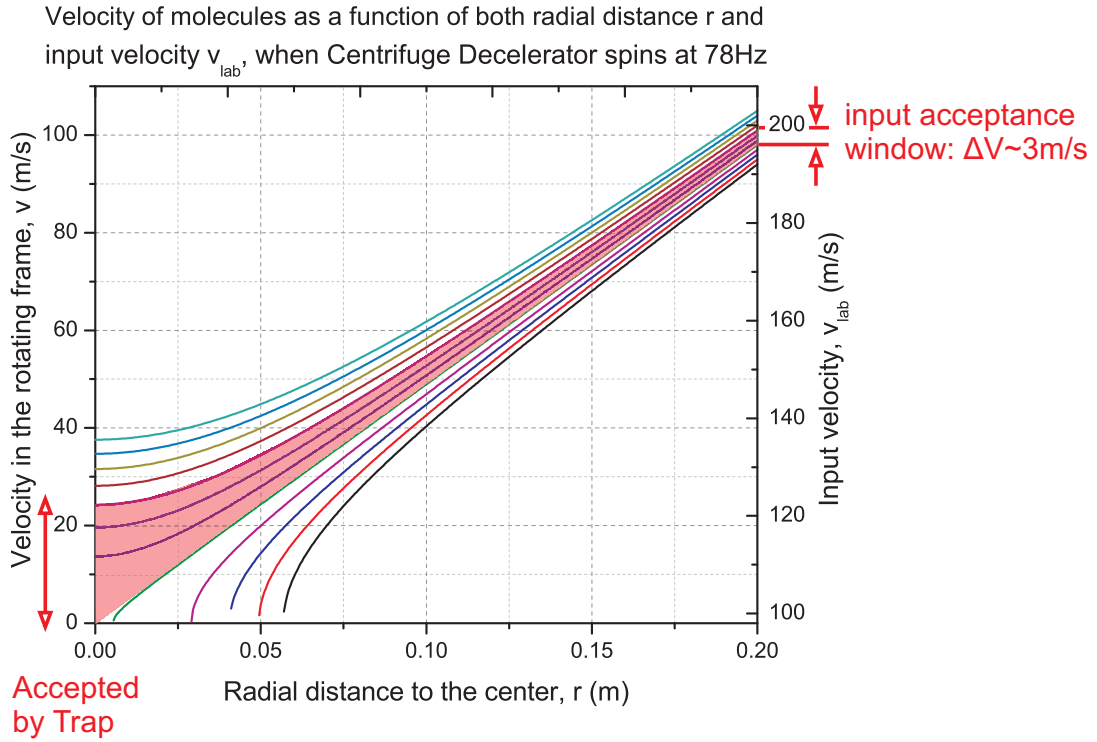input velocity v$_{lab}$, when Centrifuge Decelerator spins at 78Hz

Accepted
by Trap

Figure 3.3: *Molecules' velocity v in the rotating frame (left axis) as a function of both the input velocity v$_{lab}$ (right axis) and the radial distance to the center of the rotating frame r (horizontal axis). Curves of different color show the dependence of v on r for different input velocities. Adjacent curves differ by $1\,m/s$ in input velocity. The red shadow highlights the velocity decrease of all molecules that end up with $v_{output} \lessgtr 24\,m/s$ ($\sim 1\,K$ kinetic energy) upon leaving the decelerator.*

as highlighted by the red shadow in the figure. The input acceptance window is indicated on the right axis of the figure. All molecules at v_{lab} within this window are able to reach the output and fall within the trap depth. All molecules at input velocities outside this acceptance window will be either too slow to reach the output or too fast to be trapped after leaving the centrifuge. The width of the input acceptance can be approximated by differentiating Eq.3.9,

$$\Delta v_{lab} \approx \frac{2v_{out}}{v_{lab}} \Delta v_{out}. \tag{3.13}$$

Eq.3.13 shows that the width of acceptance scales approximately inversely to v_{lab}. Thus, the higher the initial velocity, the narrower the acceptance window at the input. For the numerical example of $v_{lab} = 200\,\text{m/s}$, $\Delta v_{lab} \approx 3\,\text{m/s}$.
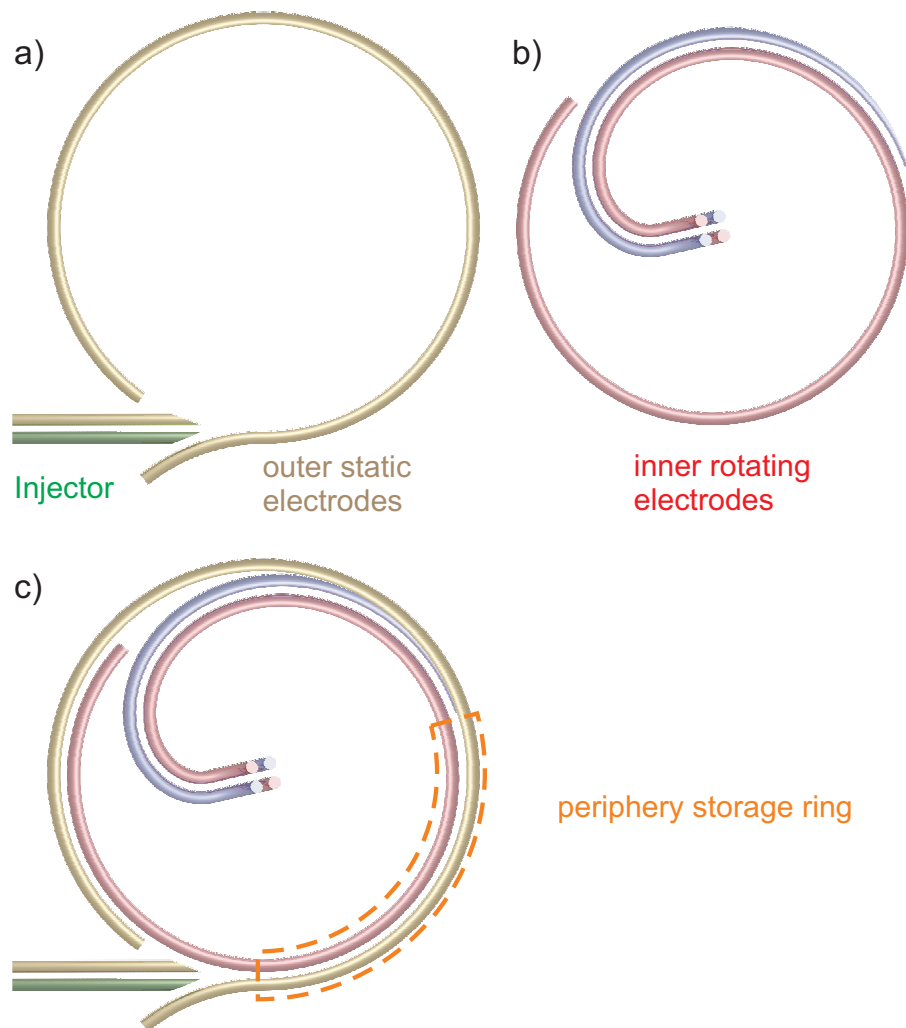
Figure 3.4: *Layout of the centrifuge design (top view). a) Static part of the centrifuge (including the injector). The brown and green curves represent electrodes of opposite polarities. b) Rotary part of the centrifuge. The blue and red curves represent electrodes of opposite polarities. c) Design assembly. The blue rotating electrodes and the brown static electrodes have the same polarity. The periphery storage ring is highlighted.*

3.3   Design concept for a continuous deceleration

After explaining the principle of the centrifuge decelerator in Sec. 3.1 and 3.2, here we present an overview of the design concept, which enables a continuous deceleration of molecular beams.

The centrifuge decelerator consists of two parts: static electrodes along the periphery (Fig.3.4(a)) and rotary electrodes in the inner region (Fig.3.4(b)). The static part comprises two parallel electrodes of opposite polarities, covering almost the entire periphery except at the opening for an injector. The injector is a straight

quadrupole guide, with the tips tapered so that it can be inserted deeply into the decelerator to minimize the loss of molecular flux (details are given later in Sec. 3.5.1). The rotary guide has a spiral shape from the periphery to the center, and consists of four parallel electrodes in a quadrupole configuration. The two inner electrodes of the four rotary ones extend in a circular shape, parallel to the outer static electrodes. This 'sweeping tail' and the two outer static electrodes form a storage ring of molecules around the periphery (Fig.3.4(c)).

This storage ring is an important feature of the design because it enables a quasi-continuous operation of the centrifuge decelerator. Without this structure, molecules could only be collected by the rotating spiral once per cycle, namely when the 'pick-up' point of the spiral guide directly faces the injector. Whereas with the periphery storage ring included in the design, molecules will be temporarily stored along the periphery even if they enter the centrifuge while the 'pick-up' is away from the injector (as sketched in Fig.3.4(c), or Fig. 3.1(a)). These molecules are able to catch up with the rotating guide after propagating along the periphery ring for a while, under the assumption that their velocity in the lab frame v_{lab} is about two times the peripheral velocity of the rotating spiral $v_{periphery}$, as pointed out in Eq. 3.12 for the optimized operation. If $v_{lab} < v_{periphery}$, the centrifuge is simply too fast.

This intake of fast molecules by the 'sweeping' spiral on the periphery is only quasi-continuous. The periphery storage guide opens up at the position of the injector. Thus the continuous intake also breaks down when it has almost completed one full cycle there. This discontinuity looks like a very minor portion on the schematic in Fig.3.4(c), but as will be shown later, this gap is about 30% of the full circle in a real set-up (see the topview in Fig. 3.7) due to practical reasons (e.g. mechanical stability).

3.4 Design of the rotating spiral

The centrifuge potential in the rotating frame is conservative. The amount of energy removed is independent of the exact trajectory taken, but only depends on the initial and final radial distance inside the rotating frame (assuming a constant angular velocity $\vec{\Omega}$). Therefore, the exact trajectory taken up by a molecule inside the rotating frame does not matter for the deceleration. Even a straight line along the radial direction instead of a spiral-shaped trajectory should work in principle.

3.4.1 The 'constant force' constraint

There exists, however, a practical constraint that the polar molecules have to be confined in the electric quadrupole guide so that they follow the rotation. This requires that, for any chosen trajectory, the sum of the centrifugal force and Coriolis forces exerted on the molecule must always remain smaller than the guiding force, which depends on the electric field gradient and the dipole moment of the molecule.

This force has two properties. Firstly, its magnitude is constant along the entire trajectory because the voltage on the electrodes, the inter-electrode spacing, and the electric dipole orientation of a molecule[2] are not expected to change during this process. Secondly, this confining force is always perpendicular to the molecule's 'longitudinal' trajectory since the quadrupole field gradient only exists transversely to the guide.

The above-mentioned constraint can be satisfied by a trajectory of a constant force. More precisely, this force exerted on the molecule is constant in magnitude along the path in the lab frame and perpendicular in direction to the trajectory in the rotating frame. In addition, the trajectory requires three initial conditions, the initial radial distance R (in our centrifuge design $R = 20\,\text{cm}$), the initial velocity of the molecules in the rotating frame $\vec{v}_{initial}$, and the constant angular velocity of the rotating frame $\vec{\Omega}$. For any given set of $(R, \vec{v}_{initial}, \vec{\Omega})$, by varying the magnitude of the constraint force $|\vec{F}|$, one can obtain a family of 'constant-force' curves which only differ from one another in the radius of curvature. With an appropriate value of $|\vec{F}|$, one can pass the curve exactly through the center of the rotating frame.

The so-produced curve for $|\vec{F}|$ works also for all initial velocities below $|\vec{v}_{initial}|$ and for all angular velocities smaller than $|\vec{\Omega}|$, since the confining forces required in these cases are smaller than $|\vec{F}|$.

3.4.2 Exit-bend

Near the center of rotation, the decelerated molecules need to be extracted out of the decelerator. As already pointed out in Fig. 3.1(a) and (b), our solution is to bend the quadrupole guide by 90° away from the rotation plane near the center, so that molecules can leave the centrifuge along the rotation axis. Thus, the whole guiding trajectory is 3-dimensional. To simplify the design and manufacturing, we separate the exit-bend near the center of rotation from the spiral-shaped curve in the outer region. The outer spiral stays in the rotating plane, hence remains 2D. The exit-bend curve is chosen under a co-planar condition, which requires it to stay co-planar with the axis of rotation. Thus, the original 3D trajectory splits into two 2D segments. This considerably reduces the difficulty in manufacturing the electrodes.

3.4.3 Combining the in-plane and exit-bend curves

As discussed in Section 3.4.1 and 3.4.2, we are searching for a spiral segment in the rotating plane and a bend-up segment co-planar with the rotating axis. The former starts from the periphery pointing in the azimuthal direction, and ends when it points towards the rotation center. The latter starts immediately afterwards, and terminates when its tangent overlaps with the rotating axis.

---

[2] This holds as long as there is no ΔM-changing inelastic collision happening in the guide. Such losses due to collisions would not be mended by the trajectory design, hence are irrelevant here.

The equations of motion for the spiral trajectory are derived with the constraints laid out in Section 3.4.1, and are summarized below,

$$a_x = \ddot{x} = \frac{\Omega x - \dot{y}}{\sqrt{\Omega^2 (x^2 + y^2) + \dot{x}^2 + \dot{y}^2 + 2\Omega (y\dot{x} - x\dot{y})}} |\vec{a}|, \qquad (3.14)$$

$$a_y = \ddot{y} = \frac{\Omega y + \dot{x}}{\sqrt{\Omega^2 (x^2 + y^2) + \dot{x}^2 + \dot{y}^2 + 2\Omega (y\dot{x} - x\dot{y})}} |\vec{a}|, \qquad (3.15)$$

and

$$a_z = \ddot{z} = \dot{z} = z = 0, \qquad (3.16)$$

where a_x, a_y, a_z, x, y, and z are the acceleration and coordinates of the molecule in the lab frame, $|\vec{a}| = |\vec{F}|/m$ is the magnitude of acceleration, and Ω is the angular frequency of the rotating frame. The transformation from the lab frame to the rotating frame is given by,

$$\begin{pmatrix} x_R \\ y_R \end{pmatrix} = \begin{pmatrix} \cos\Omega t & \sin\Omega t \\ -\sin\Omega t & \cos\Omega t \end{pmatrix} \cdot \begin{pmatrix} x \\ y \end{pmatrix}, \qquad (3.17)$$

where x_R and y_R are the coordinates in the rotating frame.

The equations of motion for the exit-bend are based on the considerations in Section 3.4.2, and are summarized below,

$$\ddot{\rho} = -\dot{z}\sqrt{\frac{|\vec{a}|^2 - 4\Omega^2\rho^2}{\dot{\rho}^2 + \dot{z}^2}} + \Omega^2\rho, \qquad (3.18)$$

$$\dot{\phi} = \ddot{\phi} = 0, \qquad (3.19)$$

and

$$\ddot{z} = -\dot{\rho}\sqrt{\frac{|\vec{a}|^2 - 4\Omega^2\rho^2}{\dot{\rho}^2 + \dot{z}^2}}, \qquad (3.20)$$

where ρ, ϕ and z are the cylindrical coordinates in the rotating frame. Note that Eq.3.19 stems from the co-planar constraint (Section 3.4.2).

Solving these coupled differential equations numerically yields the 'constant-force' curve (Fig.3.5). The curves in Fig.3.5 (a) and (b) have been obtained for the upper limits of the values for the following set of parameters: constant force $|\vec{F}|/m = |\vec{a}| = 3.5 \times 10^5\,\mathrm{m/s^2}$, input velocity $v_{lab} = 263\,\mathrm{m/s}$, and frequency of the rotating frame $\Omega/2\pi = 90\,\mathrm{Hz}$. The value of $|\vec{a}|$ is within the safety margin, since the force experienced by our polar molecules (dipole moment $d \sim 1\,\mathrm{D}$, mass $M \sim 20\,\mathrm{amu}$) in the quadrupole guide (field gradient $\nabla E \sim 10^{10}\,\mathrm{V/m^2}$) is $\gtrsim 10^6\,\mathrm{m/s^2}$. The chosen value for the input velocity is higher than the typical velocities for molecules which we want to decelerate (see Chapter 4). Therefore, the red curve in Fig.3.5 (the trajectory in the rotating frame) has been chosen as the shape of the rotating electrodes in our centrifuge design.
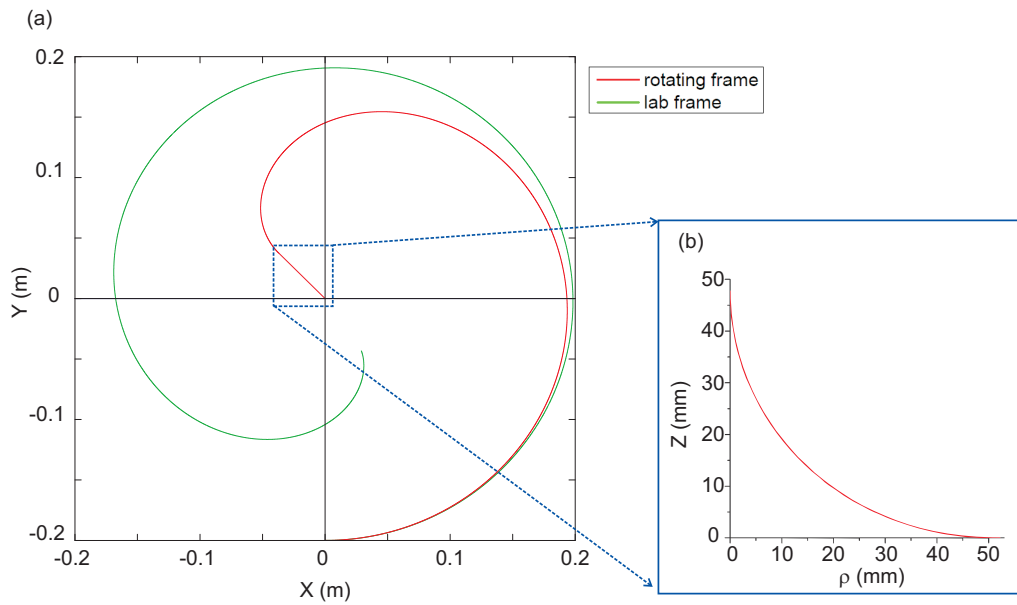
Figure 3.5: *The numerically calculated 'constant-force' curve for molecules launched into the rotating frame at $X = 0\,m$, $Y = -0.2\,m$, along x direction, with $v_{lab} = 263\,m/s$, $\Omega/2\pi = 90\,Hz$, and $|\vec{a}| = 350200\,m/s^2$. (a) The in-plane part of the trajectory. The green curve shows the trajectory in the lab frame, while the red curve shows the trajectory in the rotating frame. The straight segment at the end of the red curve is the projection of the bend-up part in the rotating plane. (b) The bend-up part of the 'constant force' curve, which is planar and contains the axis of rotation.*

3.5 The interior of the centrifuge

After the spiral-shaped trajectory has been thoroughly elaborated based on the 'constant force' constraint in Sec. 3.4, the technical realization of this trajectory and other critical components inside the centrifuge decelerator are presented here.

Figure 3.6(a) shows the interior of the centrifuge from a 3D perspective. All the visible important components are labeled in the figure. For mechanical stability and to facilitate the high-precision manufacturing, the four cylindrical electrodes are replaced by the carved edges of four solid disks which are stacked on top of one another (see Fig. 3.6(b)). These carved edges of the stacked disks give rise to a quadrupole guide, as shown in the zoom-in of Fig. 3.6(b). The disks are separated and insulated from each other by nested ceramic spheres (Si_3N_4), and mechanically clamped together with titanium screws (see Fig. 3.6(c) and its zoom-in). The spacing between the neighbouring disks is 3 mm. The photo of one of the machined centrifuge disks is shown in Fig. 3.6(d). The top view of the already assembled exit-bend plates is shown in Fig. 3.6(e). The disks are made of $AlZnMgCu_x$ alloy, which is as light as Al but more rigid. Holes are drilled in the Al alloy disks to balance them, and as a side benefit, to reduce their mass. The total mass of the four rotating disks is less than 12 kg.
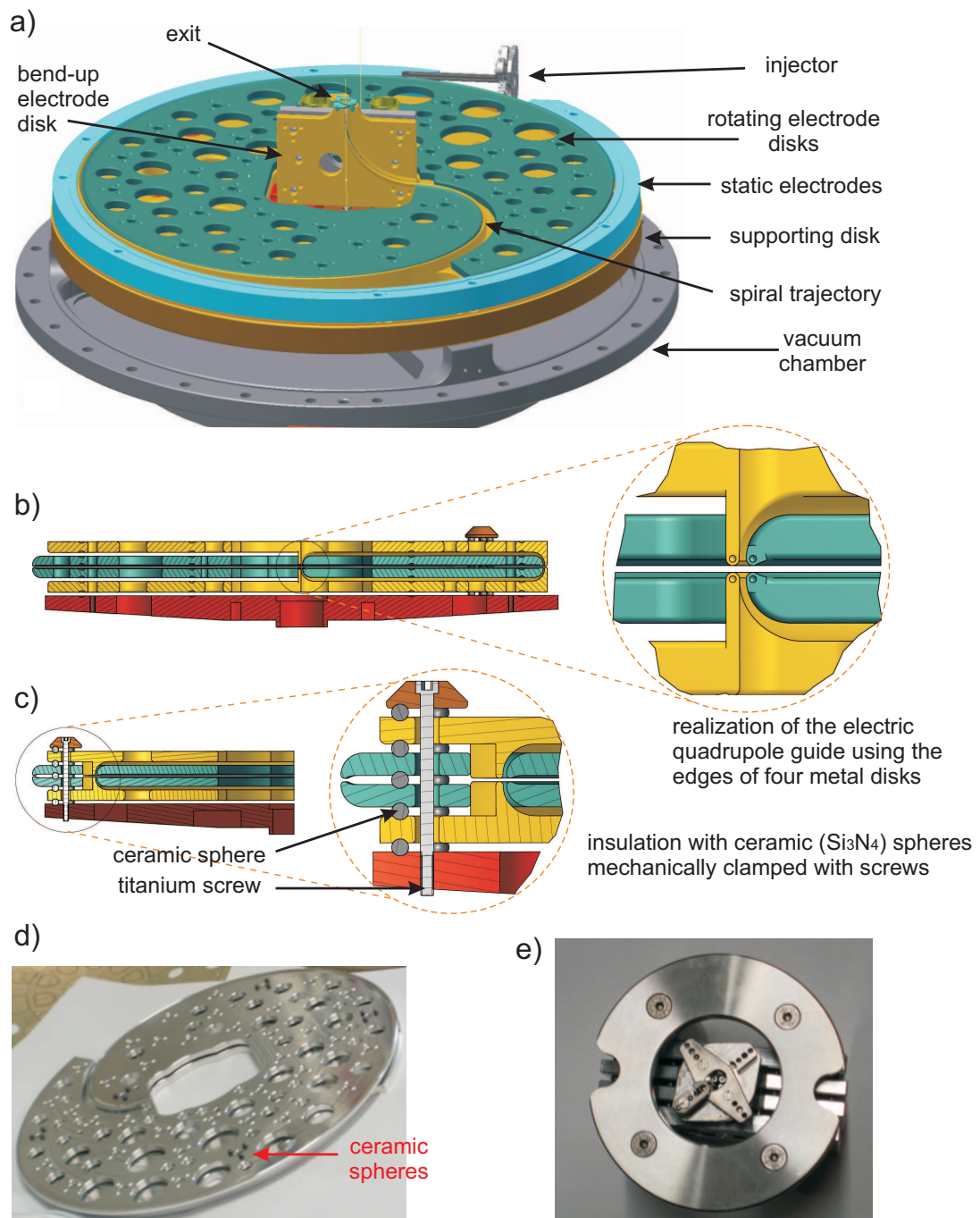
Figure 3.6: *(a) 3D technical drawing of the centrifuge assembly. Two of the rotating disks are not shown deliberately to allow view of the spiral guide. (b) Cross section of the stacked metal disks with a zoom-in of their carved edges. (c) Cross-section of half of the stacked disks showing the ceramic-sphere isolation with a zoom-in of the structure. (d) Photo of the in-plane rotating electrode disk, with some ceramic spheres placed in dimples on the top surface of the disk. (e) Photo of the assembled exit-bend plates (topview).*
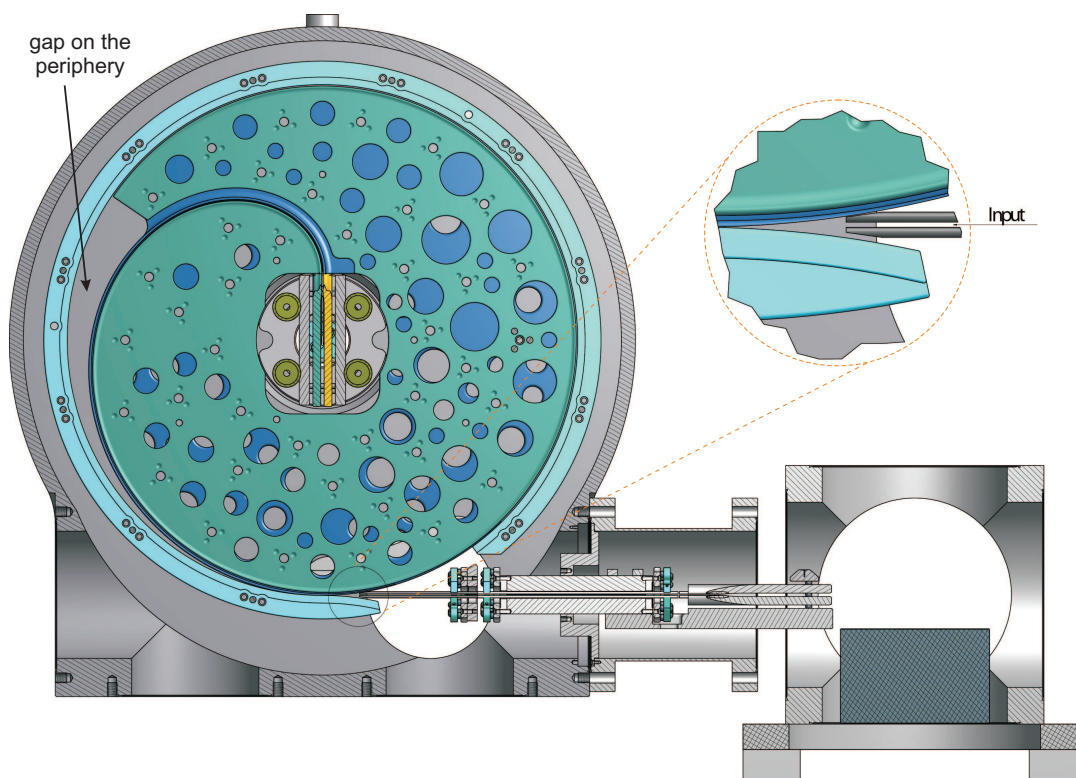
Figure 3.7: *(a) Technical drawing (topview) of the centrifuge decelerator housed in its vacuum chamber, including a zoom-in of the injector region. The two top rotating disks are not sure to keep the spiral trajectory visible.*

Figure 3.7 shows the interior of the centrifuge from a top-view perspective. It can be seen clearly that the edges of the electric disks have the same spiral shape as the 'constant force' curve plotted in Fig. 3.5(a). In addition, over 30% of the periphery guide (on the left side in Fig. 3.7) is open. The rotating disks are not extended into this region to prevent mechanical instability (as discussed at the end of Sec. 3.3). The longer this tail extends, the narrower it gets, and the easier it is to bend it outwards by the centrifugal force. On the top right of Fig. 3.7, a zoom-in of the injector region is shown.

In the remaining of this section, we will take a closer look at the optimized design of the critical components. These include the injector, the 'pick-up' (the entrance into the 'sweeping' spiral guide), and the exit. The optimization of each component is based on Monte-Carlo trajectory simulations which examine the performance of various design geometries. For each simulation, an ensemble of initial trajectories which would otherwise survive the quadrupole guiding is sent into an electric field array corresponding to a given geometry. The efficiency for a given design is defined as the transmission coefficient (ratio of the number of output trajectories and the number of input ones) obtained from the simulation, and it is the figure of merit. The geometry with the best performance in the simulation, or the one with a good balance between the simulated performance and engineering feasibility has been

chosen in the final design. The procedure of the simulation is very similar to the one explained in Sec. 2.9, and for this reason, only the final results are summarized here.

3.5.1   Injector

Figure 3.7 includes structures around the centrifuge input and a zoom-in of the injector region. The injector is a straight quadrupole guide with tapered tips, which allow for a deeper insertion of the injector into the centrifuge to minimize the loss of molecular flux. The open region between the tip of the injector and the peripheral electrodes is characterized by a weak confinement due to the relatively large distance between the electrodes. Molecules with large transverse velocity components can therefore easily escape sideways. This is to the main loss mechanism at the input.

The distance by which the injector can be inserted into the decelerator is critically limited by the spacing required between the upper tip of the injector and the 'sweeping' spiral guide. If the moving electrodes and the injector are too close by, discharges or even physical scratches could happen between the two. The smallest distance can be achieved by applying the same high voltage (HV) configuration (including both the polarity and the amplitude) on both the upper two electrodes of the injector and their neighboring rotating electrodes. This avoids discharges, and relaxes the spacing requirement so that we only need to prevent physical contact. This is much smaller than the distance necessary to avoid discharges if the injector electrodes and the rotating electrodes would have opposite polarities.

The dimensions in the final design are summarized here. The gap between the upper tip of the injector and the rotating spiral-shaped electrodes is $200\,\mu$m. This interspace should be sufficiently safe to avoid a physical contact, taking into account the tolerance for vibration (measured to be of the order of several $10\,\mu$m) and mechanical deformation due to large centrifugal force (estimated to be of the order of $\sim 10\,\mu$m). In addition, the tips of the injector electrodes (with $2\,$mm diameter) are tapered to $1\,$mm thickness, and the edges are rounded. It is difficult to produce even sharper tips mechanically without bending or deforming the straight electrodes.

The efficiency of this design predicted by Monte-Carlo trajectory simulations is given in Fig. 3.8. The prototype molecule used in the simulation is ND_3 at $\sim 10\,$K, this mostly in the $|1, 1, 1\rangle$ state. The plot reveals two features. Firstly, the efficiency of the injector stays well above 60% for most of the input velocities, and goes even beyond 75% for velocities above $200\,$m/s. Secondly, at low input velocities the injection efficiency drastically drops. These two features can be easily understood from the divergence angle of the trajectories. The transverse cut-off velocity in the quadrupole guide is $25\,$m/s in the simulation. This corresponds approximately to the position of the kink in Fig. 3.8. Therefore, trajectories with initial longitudinal velocities below $25\,$m/s are more likely to fly sideways, and escape from the region of weak confinement. On the contrary, trajectories with large longitudinal velocities have smaller divergence angles, and hence can fly almost straight into the peripheral
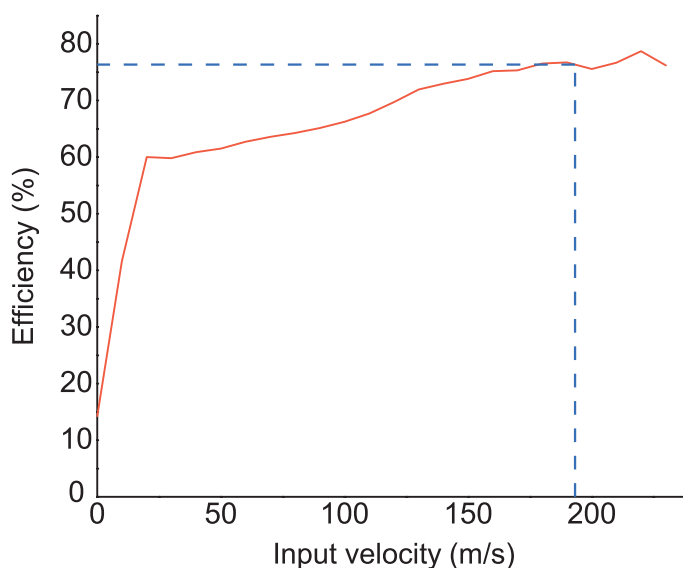
Figure 3.8: *Efficiency of the injector vs. molecular longitudinal input velocity in lab frame predicted by a Monte Carlo simulation.*

guide. It is important to remind that only the efficiency for high input velocities is relevant, since since those are namely the molecules which need to be centrifuge-decelerted.

Many other designs of the injector have also been simulated with the same numerical methods. However, they either reduce the efficiencies or require a more complicated electrode configuration.

3.5.2 'Pick-up'

'Pick-up' refers to the entrance into the rotating spiral-shaped guide (Fig.3.9(a)). It rotates along the periphery of the centrifuge, and accepts molecules almost continuously during each cycle.

The 'pick-up' is another critical component of the centrifuge because its efficiency limits the transfer rate of molecules from the periphery guide into the rotating guide. Moreover, the tips of the rotating electrodes are expected to move at $\approx 100\,\mathrm{m/s}$ relative to its neighboring static electrodes, for slowing down incoming velocities of about $200\,\mathrm{m/s}$ (see Sec. 3.2.1), while the interspace is only tiny (Fig.3.9(a)). Thus, the 'pick-up' needs a careful design for both the efficiency and safety.

The electric field distribution along the longitudinal plane through the center of the guide for the optimized design is shown in Fig.3.9(b), and the cross-section of the optimized electrode configuration is shown in Fig.3.9(c). In this configuration, the tips of the outer rotating electrodes have a thickness of $300\,\mu$m and the gap between the tips and its neighbouring static electrode is $200\,\mu$m. In addition, the tips of the rotating electrodes are grooved on the side facing the static electrodes. It is possible to manufacture a thinner tip here than for the injector (see Sec. 3.5.1)
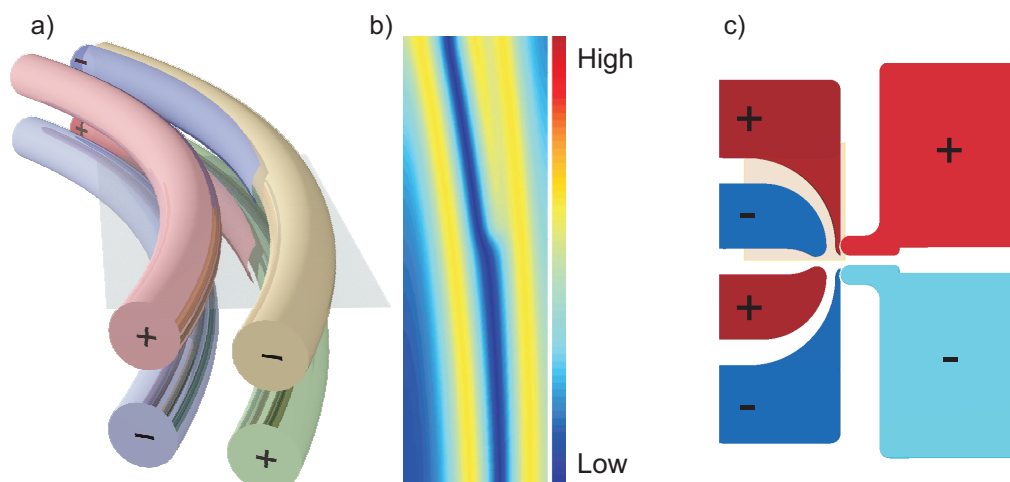
Figure 3.9: *(a) Sketch of the electrode configuration in the 'pick-up' region. The high voltage polarities on the electrodes are labeled. (b) An electric field contour plot in the longitudinal plane containing the center line of the periphery guide, from the optimized design of the 'pick-up'. (c) Cross-section of the optimized electrode configuration at the 'pick-up', from the actual technical design. The polarities are labeled on the electrodes.*
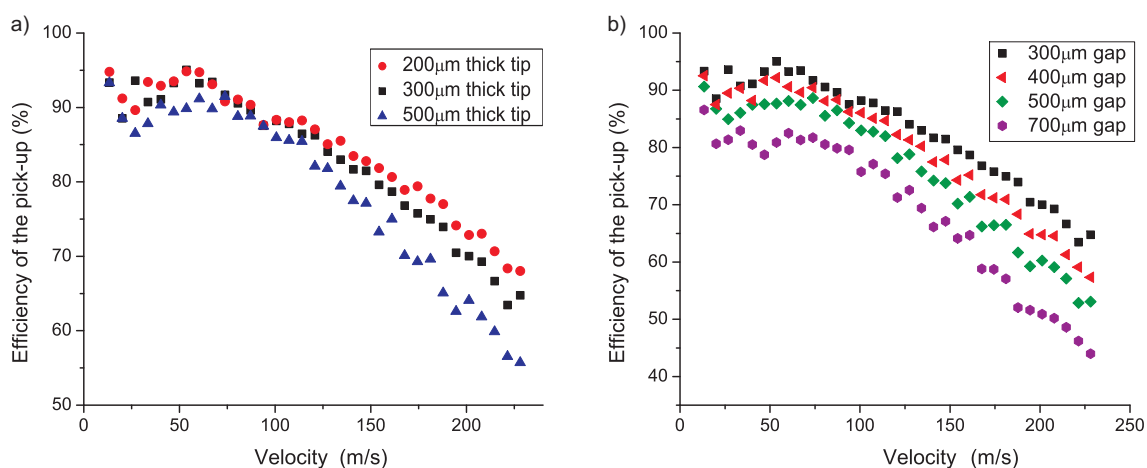

Figure 3.10: *Simulated efficiency of the 'pick-up' for different tip thicknesses and different gap sizes between the moving tips and the static electrodes. (a) Plots of the 'pick-up' efficiency vs. longitudinal velocity of the molecules in the rotating frame, for a 300 μm gap and various tip thicknesses. (b) Same plots for 300 μm tip thickness and various gap sizes.*

because it is made from the edge of a metal disk which is more rigid and stable than a thin metal rod used for the injector. The radius of curvature of the carved edge of the metal disk is 1 mm and the spacing between electrodes of opposite polarities is 1 mm.

The efficiency of the 'pick-up' is simulated via a Monte Carlo method similar to the one used for the injector, except that now the input trajectories are prepared

from the output of the injector simulation, followed by an additional electric filtering through a quadrupole bend of 90° and a radius of 20 cm. This bend is included to mimic the influence of the periphery guide of the centrifuge, which confines the molecules before they arrive at the 'pick-up'. Simulation results for different 'pick-up' designs are presented in Fig.3.10. Fig.3.10 (a) shows the input velocity dependence of the 'pick-up' efficiency for a 300 μm gap and three different tip thicknesses. There is no significant variation in the efficiency when the tip thickness is increased from 200 μm to 300 μm. Thus, the tip thickness of 300 μm has been chosen in the design. Fig.3.10 (b) shows the input velocity dependence of a 300 μm tip thickness and 300 μm, 400 μm, 500 μm, and 700 μm gap size, respectively. A decrease in the efficiency for increasing gap sizes is apparent. The smallest gap size simulated is 300 μm. In the final assembly of the centrifuge, an even smaller gap size of 200 μm has been realized, hence a higher efficiency at the 'pick-up' could in principle be expected. According to the simulation results, over 70% efficiency should be possible at the 'pick-up' for velocities up to 200 m/s.

3.5.3   Centrifuge exit

The exit-bend has already been mentioned in the earlier part of this chapter, with its 3D visualization given in Fig. 3.1(b) and Fig. 3.6(a). Fig. 3.11 illustrates the structures around the exit in the central plane of the exit-bend plates. It can be seen clearly that in the outer region, the rotating disks all lie in the rotating plane. Near the exit region, the guide bends up by 90° and output molecules along the rotating axis. The shape of the exit-bend follows exactly the curve calculated in Sec. 3.4.3 and is plotted in Fig. 3.5(b). It has a radius ≈ 5 cm. It is also apparent that this exit-bend curve is a 2D structure.

The most critical loss channel of the centrifuge happens at the gap between the end of the exit bend which rotates with the centrifuge and the straight quadrupole guide outside the centrifuge which is static in the lab frame collecting the decelerated molecules. As molecules arriving here are longitudinally slow after the deceleration, their divergence is significant, and that is why those molecules are prone to escaping in the gap region, which entail losses. This is especially the case for the slowest molecules. The trajectories of a sample of slow molecules ($v_z \approx 6$ m/s) lost around the gap region at 0° phase angle (explained in Fig. 3.14 later) are simulated, and their projections in the x-z plane and in the y-z plane are plotted in Fig. 3.12 and Fig. 3.13, respectively. The red dashed lines in each plot indicate the guide volume at both sides of the gap. The zoom-in in Fig. 3.11 illustrates the distance at the gap, which has been designed to be 1.2 mm. This gap can not be narrower because a mechanical valve needs to be accommodated here, to separate the centrifuge chamber from the detector chamber. This valve when being closed is capable of maintaining ultra-high vacuum in the detection chamber while the centrifuge chamber is at atmospheric pressure [48]. In order to maximize the transmission efficiency, the alignment of the straight static guide to the rotating guide should be perfect, such that the trap
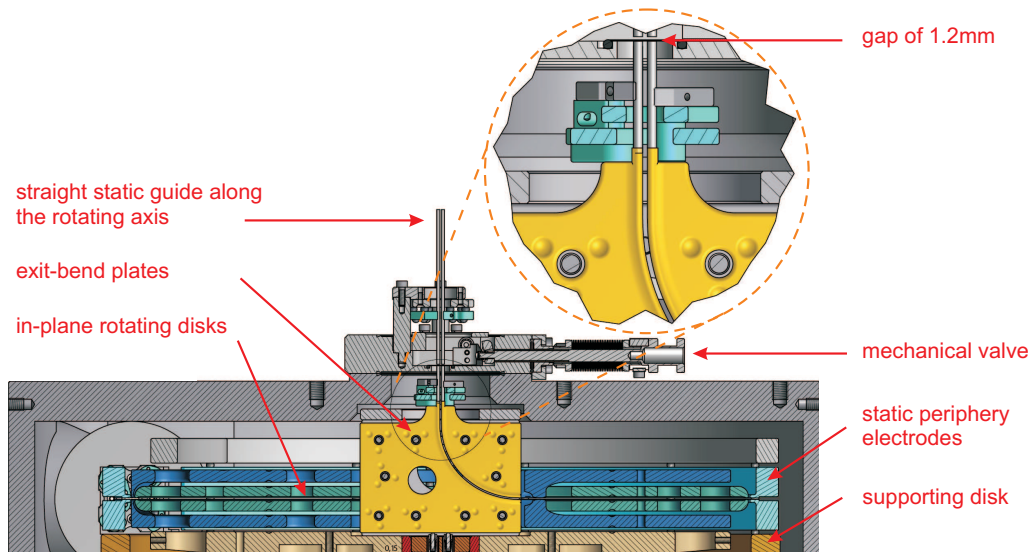
Figure 3.11: *Technical drawing of the cross-section of the centrifuge in the plane containing the exit-bend. The curved groove on the disk forms the molecular guide. The straight static guide outside the centrifuge is aligned along the rotation axis. The zoom-in illustrates the gap between the rotating and the static guide.*

minima of both segments match each other.

An interesting feature is that the relative rotation between the static and rotating guides does not have a significant influence on the passing molecules. The rotation of the centrifuge at even the maximum speed (90 Hz) is too slow to be 'seen' by the molecules. The typical time scales molecules spend in the gap is given by,

$$\tau_{mol} \sim \frac{gap\,size}{\overline{v}} \sim \frac{1\,mm}{10\,m/s} = 10^{-4}\,s, \tag{3.21}$$

whereas the typical time scale for the relative rotation is,

$$\tau_{\Omega} \sim \frac{1}{100\,Hz} = 10^{-2}\,s. \tag{3.22}$$

Thus, the time scale for the relative rotation is at least two orders of magnitude larger than that spent by the molecules in the gap. What the passing molecules see is the instantaneous electric field distribution in the gap. The field distributions for three particular phases of the relative rotation, 0°, 90°, and 180°, are given in Fig. 3.14.

The transmission efficiencies of the rotating-to-static interface for the three relative phase angles are obtained from Monte Carlo simulations. Fig.3.15 shows the simulation results. The transmission efficiency is defined as the ratio of the number of molecules arriving at the end of the static segment and the number launched at the rotating segment. The general trend for all three phases (as shown in Fig.3.15)

Figure 3.12: *Projections in the x-z plane for the individual trajectroies of a sample of slow ($v_z \approx 6\,m/s$) molecules (a-l) that are lost around the $1.2\,mm$-wide gap. The red dashed lines outline the guide volume of the two segments at both sides of the gap.*
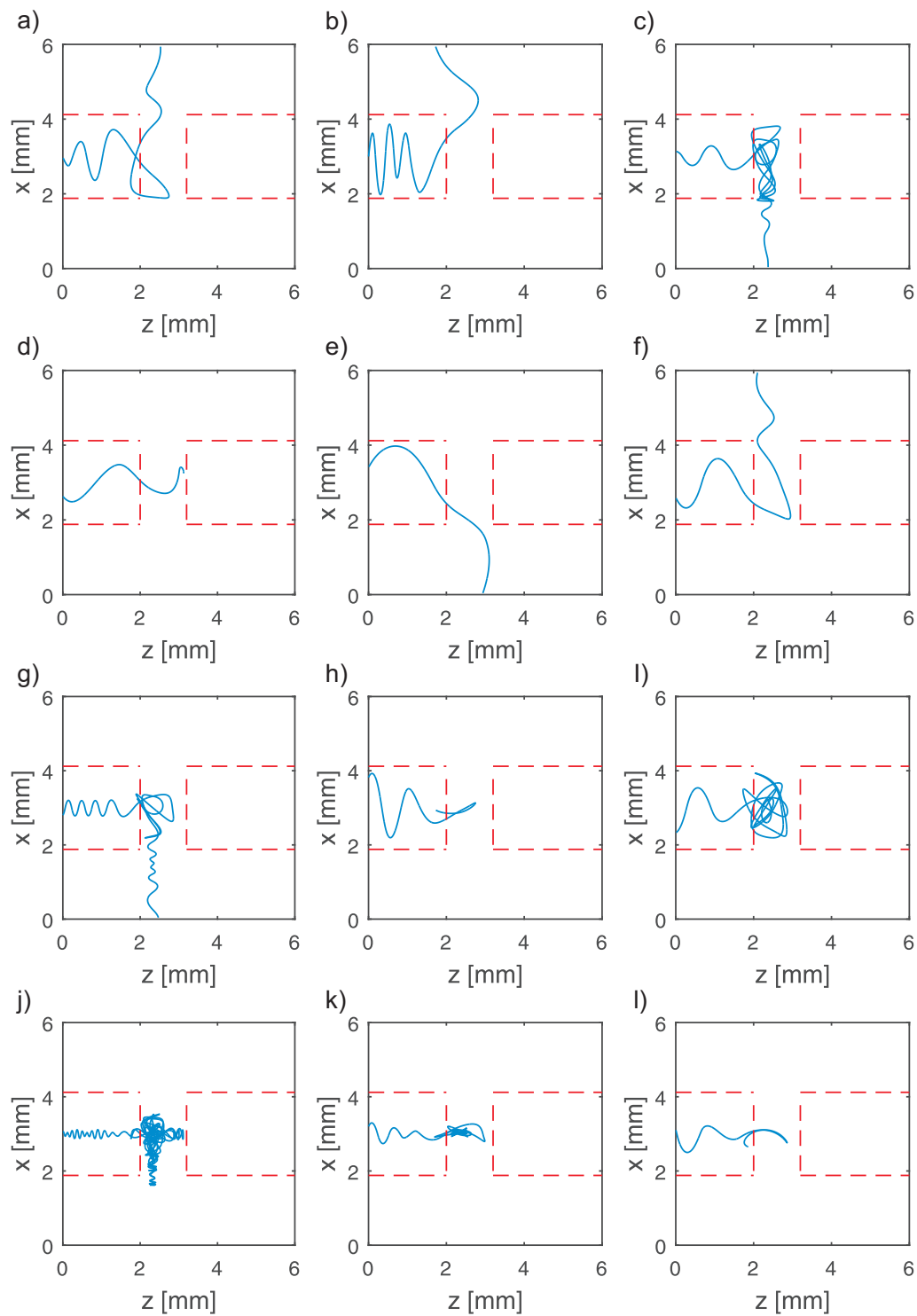
Figure 3.13: *Projections in the y-z plane for the individual trajectroies of a sample of slow ($v_z \approx 6\,m/s$) molecules (a-l) that are lost around the $1.2\,mm$-wide gap. The red dashed lines outline the guide volume of the two segments at both sides of the gap.*
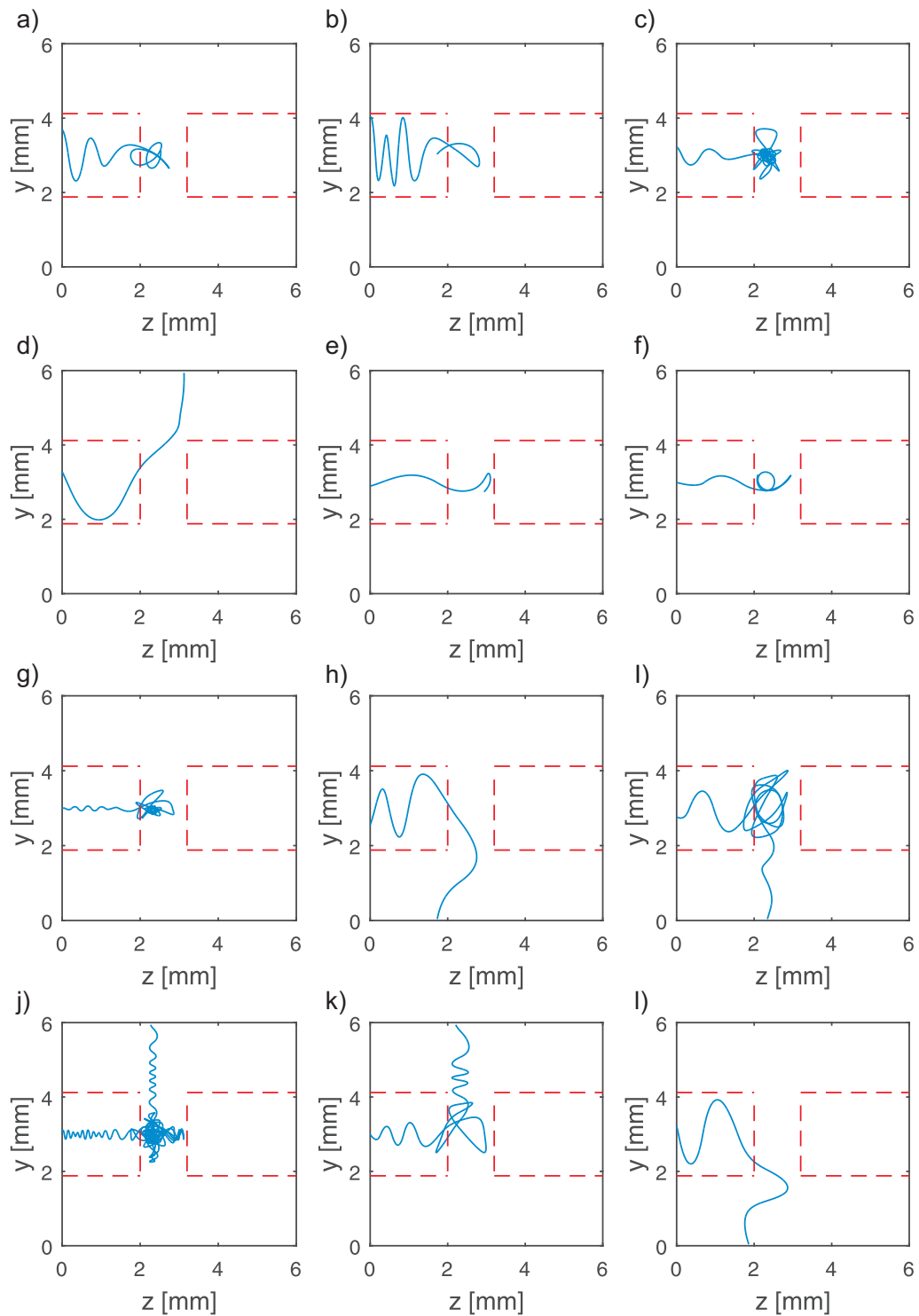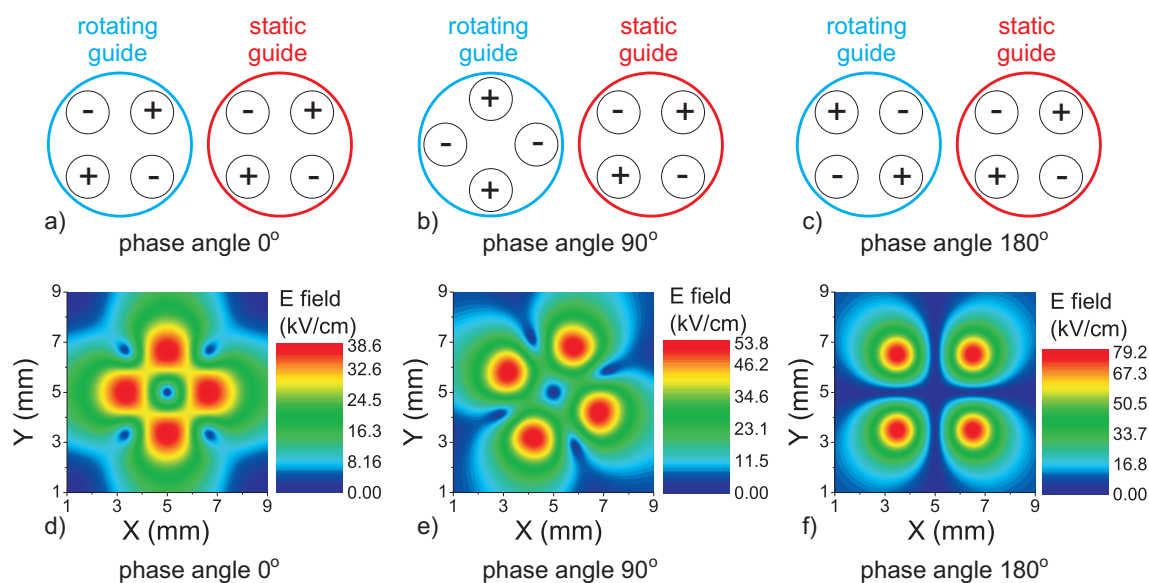
Figure 3.14: *(a)-(c) Electrode configurations of the rotating-to-static guide interface, with the relative phases of 0°, 90°, and 180°, respectively. Each black circle outlines an electrode, with a plus or minus sign at the center indicating the polarity. Note that the polarity configuration recurs after a rotation of 180°, and hence the phase angle equals twice the angle of rotation here. (d)-(f) Contour plots of the electric field strength in a plane perpendicular to the axis of rotation and at the middle of the gap, for the relative phases of 0°, 90°, and 180°, respectively.*
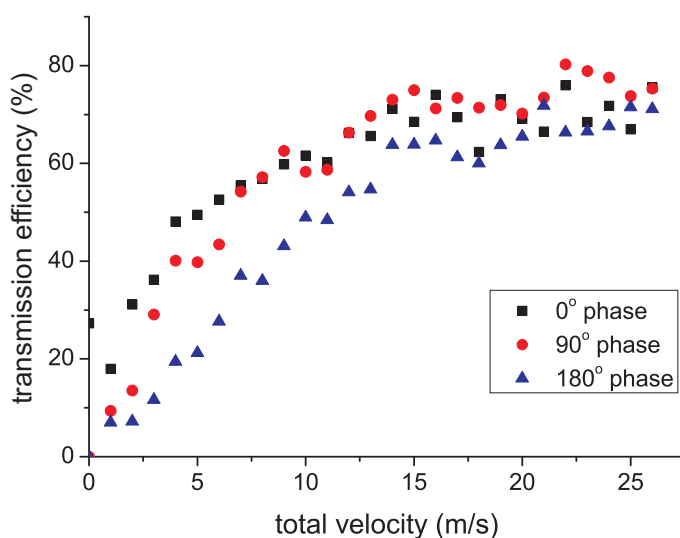

Figure 3.15: *Predicted transmission efficiency of the rotating-to-static interface as a function of the total velocity of the molecules. The simulation results for 0° phase, 90° phase, and 180° phase angles are plotted with black squares, red circles, and blue triangles, respectively.*

is that the coupling efficiency stays above 60% for relatively fast molecules, and decreases for slower velocities. The drop in efficiency at lower velocities is due to the divergence at the gap. As mentioned at the beginning of this section, it is technically more difficult to reduce the gap at the interface and hence extract more slower molecules out of the centrifuge.

In addition, Fig.3.15 shows that the coupling efficiency at 180° phase angle (when the two guiding segments are at the opposite phases) is, in general, lower than for the other phases. It is clear from the electric field contour plots in Fig.3.14(d)-(f) that at 180° phase angle, there are four leak channels along the transverse direction at the gap center.

The overall efficiency of the exit is given by an average over one cycle of rotation. As the three simulated phases 0°, 90°, and 180° occur 2, 4, and 2 times per rotation cycle, respectively, a simply weighted average of their efficiency gives 58% at 10 m/s. The exact efficiency at the exit region depends on the target velocity.

3.5.4   Total efficiency of the centrifuge

The total efficiency of the centrifuge is estimated by the product of the simulated efficiencies of each component, and the input duty cycle. Apart from the above mentioned injector, 'pick-up', and exit region, the guiding efficiency of the periphery guide is also taken into account. Additionally, a factor of 1/2 from the input duty cycle should be included.

The input duty cycle of the 'pick-up' is only 50% at the optimized deceleration condition. As discussed in Sec. 3.2.1, the molecular input velocity is roughly twice the peripheral velocity here. Therefore, the molecules entering the centrifuge when the 'pick-up' is beyond $\approx 180°$ away from the injector (the opposite position of the injector on the periphery) could not catch up with the 'pick-up' before the next rotation cycle starts. This means we lose half of the input cycle.

Moreover, the efficiency of the periphery guide is simulated simply with a 90° quadrupole bend with 20 cm radius, which is identical to the radius of the periphery of the centrifuge. The initial trajectories are prepared from the output of the injector simulation. The result predicts an efficiency of about 45% for 200 m/s input velocity.

Multiplying the efficiencies of all four components and the factor of 1/2 input duty cycle gives a total efficiency of the centrifuge of about 7% for 200 m/s input velocity.

The machined parts of the centrifuge interior are shown in Fig. 3.16.

3.6   Assembly of the centrifuge decelerator

After introducing the principle, design concept, and the interior of the centrifuge decelerator, we present in this section the assembly of the entire device. The focus here is on the engineering realization of the centrifuge. Fig. 3.17 shows the cross-
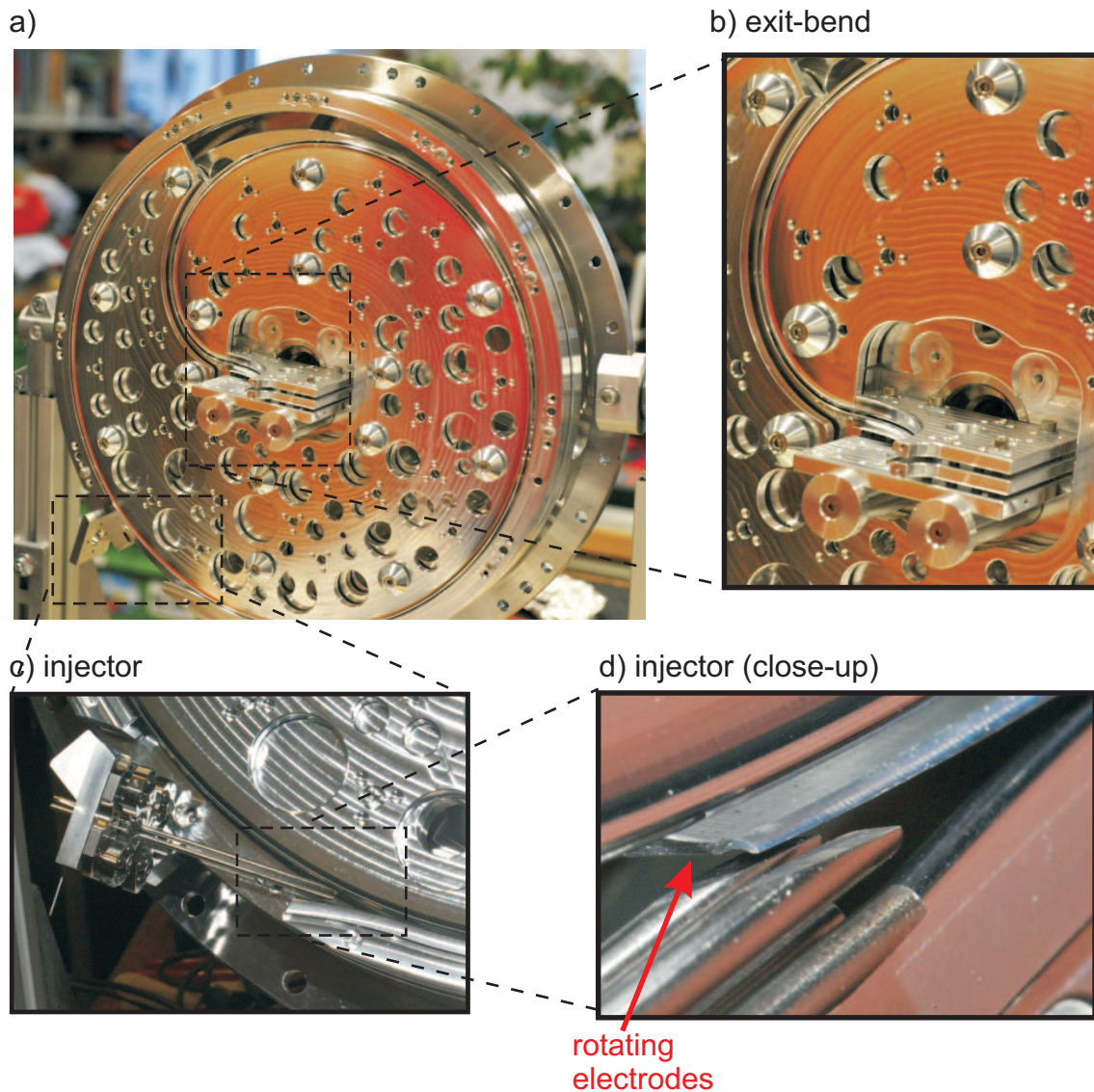
a)

b) exit-bend

c) injector

d) injector (close-up)

rotating
electrodes

Figure 3.16: *Photos of the centrifuge components. (a) The rotating disks. (b) The exit-bend. (c) The injector. (d) A close-up of the the injector, including the blade of one rotating electrodes.*

section of the decelerator, taken in a plane containing the axis of rotation. The important components are labeled inside the figure. The red dashed box highlights the structure for the high-voltage high-vacuum rotary feedthrough, and a zoom-in of this region is given in Fig. 3.18.

3.6.1 Driving motor

The motor chosen to drive the centrifuge disks is a synchronous servomotor from SEW-EURODRIVE (Model No. CMPZ80S/KY/HR1M/SM1). It turns at maximum 6000 rpm (or equivalently, 100 Hz), and output static torque of 13.4 Nm. Here,

a synchronous motor means the rotation of the motor's shaft is synchronized with the frequency of the supply current. A servomotor is one which employs a feedback loop to control the position and speed of the shaft. The error signal is typically provided by a rotary encoder which converts the angular position and speed of the shaft to an analog or digital code. Thus, a servomotor has the advantage of precise position and motion control, compared to a stepper motor. Whereas, a stepper motor relies on built-in output steps to control the motion, without using any feedback encoder. Thus, a stepper motor needs an initialization every time on power up, usually by scanning towards the two ends to recalibrate its position.

3.6.2 Flexible bellows coupling

The driving motor is connected to the shaft via a flexible belows coupling (Smartflex 0/932.333, Mayr). It can rotate at maximally 10000 rpm, with a nominal torque of 16 Nm. This type of connection is necessary to mechanically decouple the motor from the centrifuge decelerator.

3.6.3 High voltage feedthrough

Realizing the high voltage (HV) connection is one of the engineering challenges, since the ± 5 kV HV feedthrough should also be compatible with high vacuum and rotation. The details of the structure are illustrated in Fig. 3.18. The HV contact is made via two bearings, one for each polarity. These two bearings are not for supporting the weight of the rotor, but for using the metal bearing balls and the electroconductive bearing grease (Klüberlectric BE 44-152) inside to make contacts to the rotating part. Two Kapton-insulated wires embedded in the hollow shaft are connected to the bearings' inner cages, and extend to the centrifuge disks. The ends of the wires make HV contact to the exit-bend plates via a spring-loaded metal pins. As the Kapton wires and the spring-loaded contact follow the rotation of the shaft, they have no relative rotation with respect to the centrifuge disks. These structures make the HV rotary connection.

The high-vacuum rotary problem is resolved by the following design. Firstly, between the main vacuum chamber ($\sim 1 \times 10^{-8}$ mbar) housing the centrifuge disks and the motor, there is a fore vacuum chamber ($\sim 10^{-7}$ mbar). Secondly, the shaft is embedded in a magnetic fluid rotary feedthrough (see Sec. 3.6.4) at the interface between the fore vacuum chamber and the atmosphere. In addition, inside the hollow shaft is also atmospheric pressure and it is sealed by rubber O-rings at the end near the spring-loaded contact. The main vacuum chamber is evacuated by a 600 L/s turbo molecular pump (TMP, TURBOVAC 600C, Leybold), and the fore vacuum chamber is pumped by a smaller TMP (60 L/s, TMU 071 P, Pfeiffer Vacuum). Both TMPs are backed by the same pumping station (HiCube 700 Classic, Pfeiffer Vacuum).
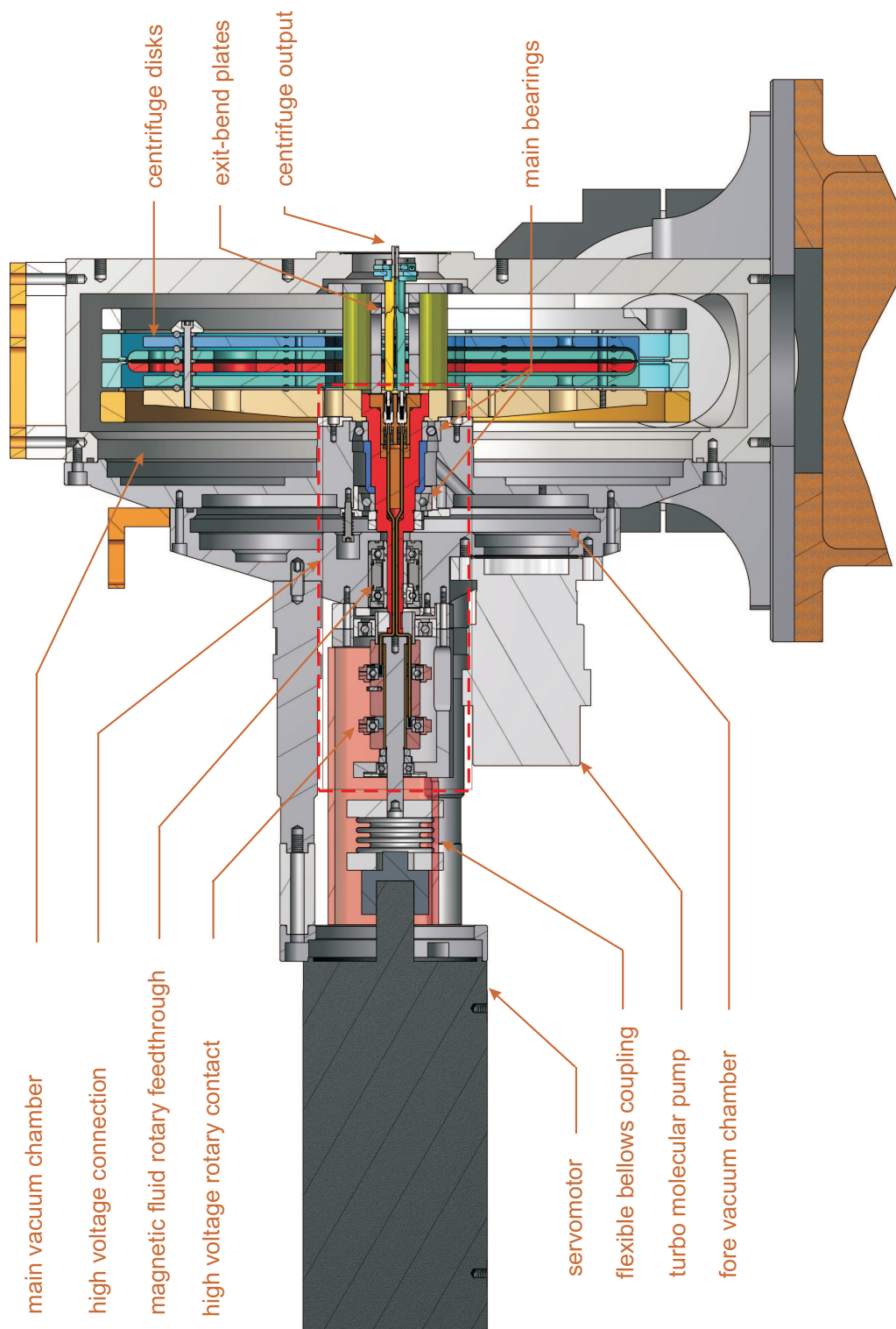
Figure 3.17: *Assembly of the centrifuge. The enlarged version of the high voltage connection region highlighted by the red dashed-line box is shown in Fig. 3.18. For details on the important components, see text.*
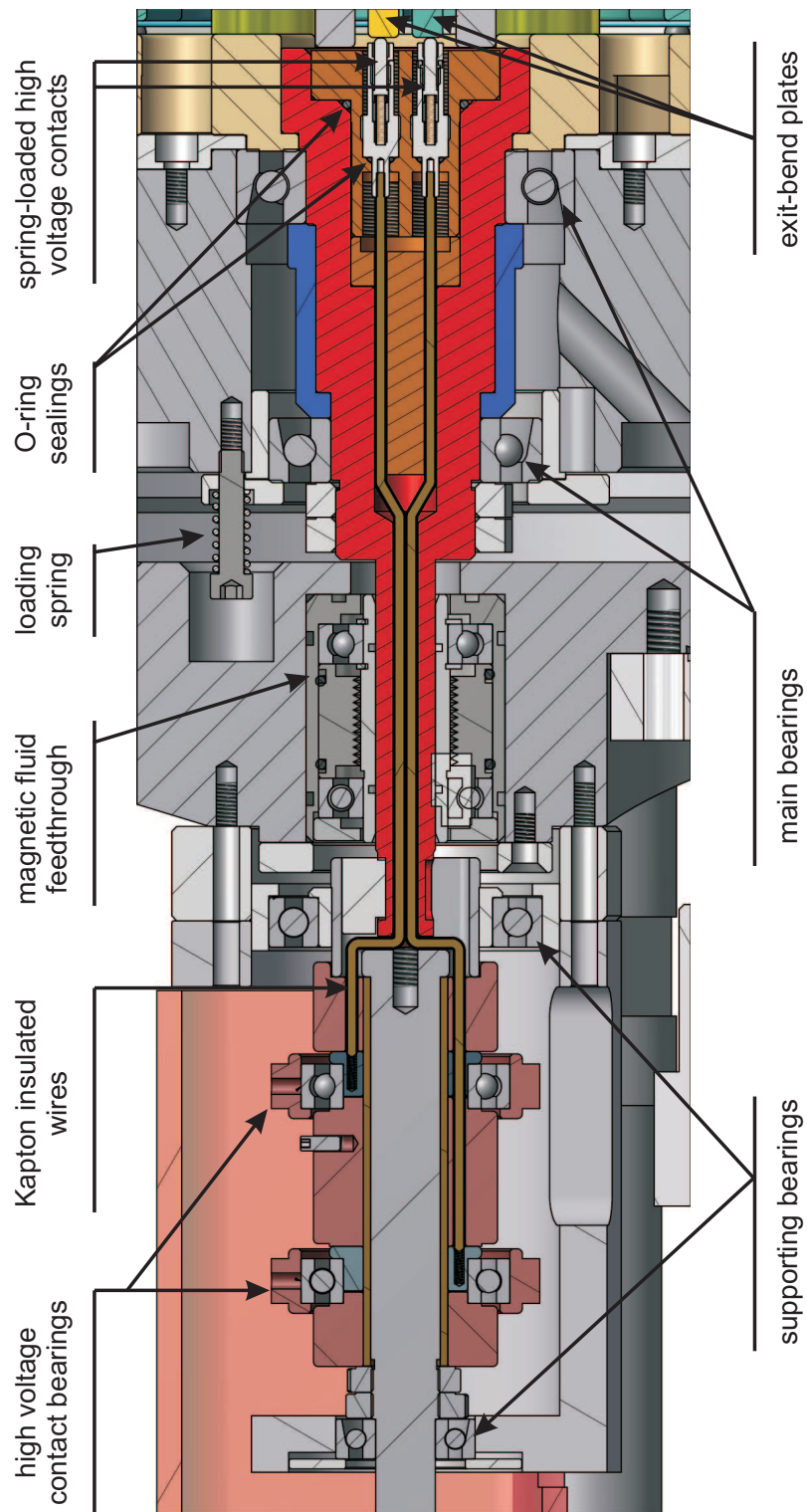
Figure 3.18: *Detailed structure of the high-voltage high-vacuum rotary connections highlighted in Fig. 3.17. For description, see text.*

3.6.4   Magnetic fluid rotary feedthrough

The magnetic fluid feedthrough we installed is a customized unit from Metallicflex. It makes dynamic sealing via oil-based liquid containing magnetic particles, which are held magnetically between the rotor and stator. The design rotation limit is 6000 rpm.

3.6.5   Main bearing

The load of the centrifuge rotating disks is supported by two high precision ball bearings (KH 6006 and 6008, from GMN). The dimensions (bore diameter, outer diameter, and thickness) of the two bearings are slightly different, $30 \times 55 \times 13$ and $40 \times 68 \times 15$, all units in mm. The smaller one has a maximum speed of 25500 rpm, while the larger one can turn maximally at 20000 rpm, well above the intended use. The mounting of the pair of main bearings is also illustrated in Fig. 3.18. From the side of the main chamber, the bigger bearing is rigidly fixed by a ring-shaped stainless steel clamp. The cross-section of the ring is shown in Fig. 3.18 as the two white structures above and below the HV spring-loaded contact. From the side of the fore vacuum chamber, the smaller bearing is embedded in a stainless steel ring, which is then pressed onto the vacuum chamber by three loading springs, exerting ≈ 100 N each on the smaller bearing. The cross-section of one of the springs is shown in Fig. 3.18. Between the two main bearings, there is a ring-shaped stainless steel spacer (its cross-section is shown as the two blue structures between the two bearings in Fig. 3.18).

3.7   Summary

In this chapter, we have developed the idea, and outlined the design of a molecular decelerator employing the centrifugal potential in a rotating frame. The dynamics of the centrifuge deceleration has been analyzed in both the rotating and the laboratory frames. The shifts of the input velocity distribution, the changes of the velocity spread, and the influence to the number density and phase-space density have been discussed. The specific design which enables a continuous deceleration has also been illustrated. Through Monte-Carlo trajectory simulations, an overall efficiency of 7% has been estimated for decelerating molecular beams at ≈ 200 m/s input velocity. In the end, the technical realization of the rotating electric guide and the design of various critical components of the decelerator have been summarized. The ingenious design and the careful assembly of every single piece was critical for the successful operation of the centrifuge decelerator.

Chapter 4

Demonstration of centrifuge deceleration

After having explained the principle, design concept, and assembly of the centrifuge decelerator in Chapter 3, here we present the proof-of-principle demonstration of centrifuge deceleration of polar molecules. After giving an outline of the experimental scheme in Sec. 4.1, the first signal obtained from the centrifuge decelerator is presented in Sec. 4.2. The continuous output of the centrifuge decelerator is illustrated in Sec. 4.3. Sec. 4.4 and Sec. 4.5 demonstrate the deceleration results for CF_3H and CF_3CCH from a liquid-nitrogen-cooled effusive nozzle. Sec. 4.6 presents the measurements of the centrifuge efficiencies for decelerating a supersonic beam and an effusive beam. In the end, Sec. 4.7 discusses important systematic effects in the time-of-flight measurements, which are critical for analyzing the molecular velocity distributions after the centrifuge.

4.1 Experimental scheme

To demonstrate the centrifuge deceleration, the experimental set-up sketched in Fig. 4.1(a) has been used. Molecules from lecture bottles are delivered to a ceramic nozzle, which can operate in the temperature range from $100\,\mathrm{K}$ to $400\,\mathrm{K}$. The nozzle is cooled by liquid nitrogen, and the temperature is controlled by a feedback loop containing an electric heater and a PT100 temperature sensor. Upon leaving the nozzle, the molecules form an effusive beam. They are then guided and pre-filtered by a quadrupole bend in the input chamber, before arriving at the injector of the centrifuge (see Fig. 4.1(a)). The radius of this bend is $20\,\mathrm{cm}$, the same as the radius of the peripheral guide of the centrifuge. Thus, molecules that are initially in non-guidable states or are too fast to be guided around the centrifuge periphery will be filtered out before reaching the centrifuge chamber. After the deceleration, the molecules coming out of the centrifuge, are collected by a $0.5\,\mathrm{m}$ long straight guide which delivers them to the detector, a quadrupole mass spectrometer (QMS). The high voltage (HV) of this straight guide can be toggled on and off to make

time-of-flight (TOF) measurements, to determine the velocity distributions of the centrifuge-decelerated molecules. The QMS ionizes the incoming molecules, and in the ion counting mode, it outputs one TTL pulse for each detected ion. The number of TTL pulses per unit time, i.e. the count rate, corresponds to the molecular density. The QMS signal is read and histogrammed by a multi-channel scalar card (MCS-pci, Ortec) with an adjustable temporal resolution. The MCS card can be synchronized with the switching sequence of the TOF measurement, as illustrated in Fig. 4.1(b). The top row of Fig. 4.1(b) shows an example of the TOF data recorded by the MCS card. By differentiating the TOF signal, the corresponding velocity distribution of the decelerated molecules can be obtained [48]. The middle row of Fig. 4.1(b) indicates the timing of a trigger signal for the starting the MCS card. The bottom row shows the switching of the TOF guide.

Details of the QMS detection, including various systematic effects will be discussed later in Sec. 4.7.

4.2   First signal from the centrifuge

Thanks to the careful design and assembly of the centrifuge, we were able to detect signals at the output on the first run (see Fig. 4.2)! The signals were obtained with CH_3F from a room-temperature nozzle. HV of ± 2.5 kV was applied to all electrodes, including the centrifuge. No switching was applied to the TOF guide, in this particular measurement. The screenshot in Fig. 4.2 shows a temporal dependence of the count rate, which started after we manually turned the centrifuge shaft. The modulation in the signal comes from the gap on the centrifuge periphery, which is about 30% of the full circumference (see the technical drawing in Fig. 3.7 or the photo in Fig. 3.16(a)). The modulation became faster when manually speeding up the centrifuge rotation. The highest rotation speed reached here was about 0.7 Hz. This corresponds to a deceleration of about 1 m/s.

Once the motor was powered up and the HV switching was applied to the TOF guide, velocity distributions after the centrifuge were measured. Fig. 4.3 shows the first velocity distribution obtained from the centrifuge, with 50 Pa CH_3F (measured at the gas line input for all the measurements reported in this chapter) applied to the room temperature nozzle. All guides were at ± 4 kV. The vertical scale in Fig. 4.3, $\Delta R/\Delta v$, represents count rates per velocity interval. The unit is given in [(counts/s)/(m/s)]=[counts/m]. Thus, the area under the curve corresponds to the total signal at the detector. The distributions with the centrifuge at stationary (blue) and at 33 Hz (red) are compared in Fig. 4.3. The area below 22 m/s (≈ 1 K kinetic energy for CH_3F) under the red plot is much larger than the one under the blue plot. This clearly demonstrates the deceleration of CH_3F molecules to below 1 K by spinning the centrifuge. The explanation for the increase in signal for the centrifuge at 33.3 Hz is that the loss of molecules at the sharp exit bend (bend radius 5 cm) is reduced. As a result of the centrifuge deceleration, many initially
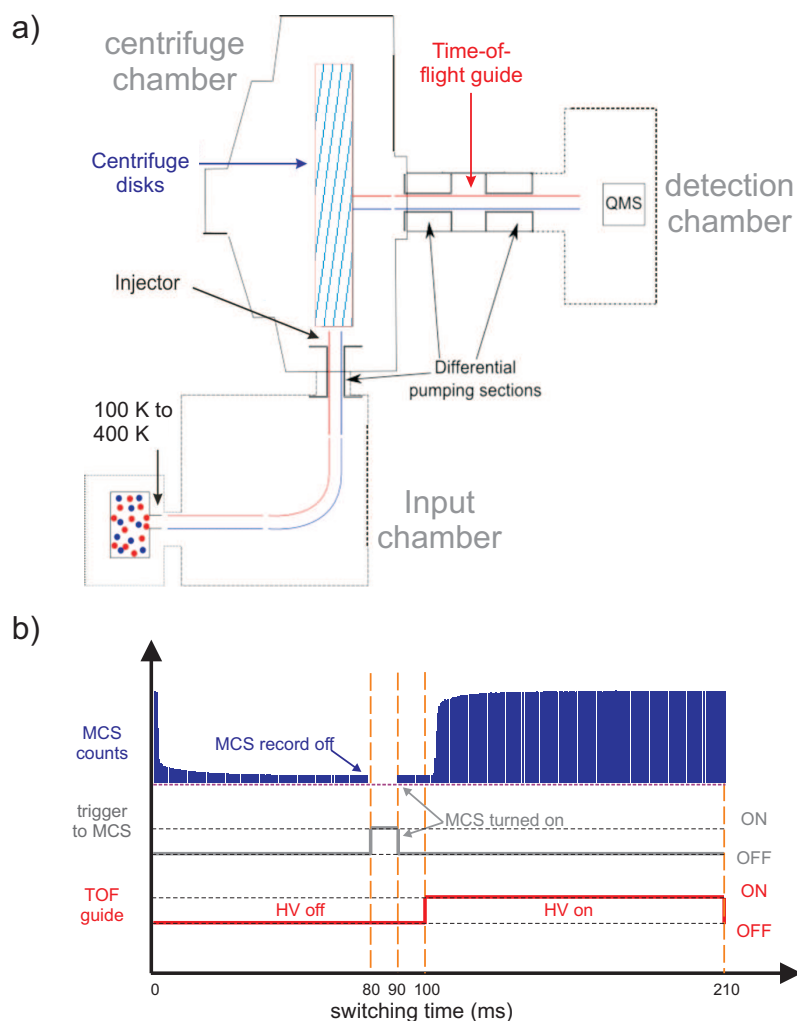
Figure 4.1: *(a) Schematic top view of the experimental apparatus for the centrifuge deceleration. The blue and red curves represent the top two electrodes of the quadrupole guide. For simplicity, the centrifuge disks are represented by a blue hatched rectangular box in the figure. The quadrupole mass spectrometer is represented by the square to the right of the time-of-flight (TOF) guide. (b) Switching protocol for a TOF measurement. Typical TOF data histogrammed by the MCS card are also shown.*

fast molecules now arrive at the bend with smaller velocities and thus can be guided to the exit (as illustrated in Fig. 3.2).

4.3 Continuous deceleration

A unique feature of the centrifuge design is its ability to decelerate continuous beams (Sec. 3.3). In this section, we demonstrate the continuous output of the centrifuge decelerator. Towards this end, all guiding segments were constantly on, and the data
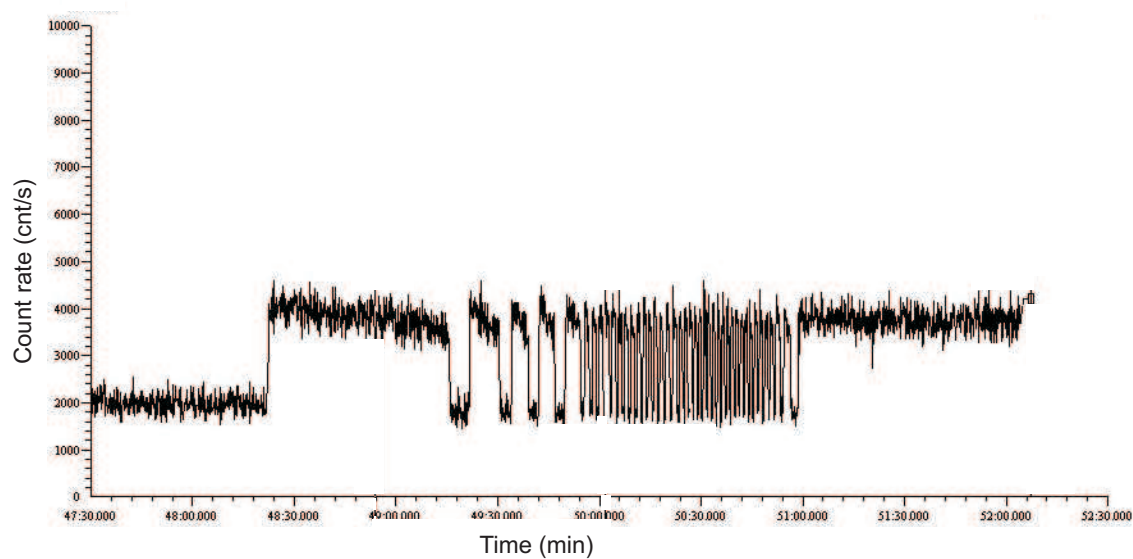
Figure 4.2: *Screenshot of the data-acquisition monitor showing one of the very first signals from the centrifuge. No switching was applied to the guiding, and high voltage was constantly on. The modulation of the signal came from turning the centrifuge shaft manually. The modulation became faster due to an increase in rotation frequency.*

Figure 4.3: *Velocity distributions of CH_3F measured after the decelerator, for a stationary centrifuge (blue) and for a rotating centrifuge at $33.3\,Hz$ (red)*

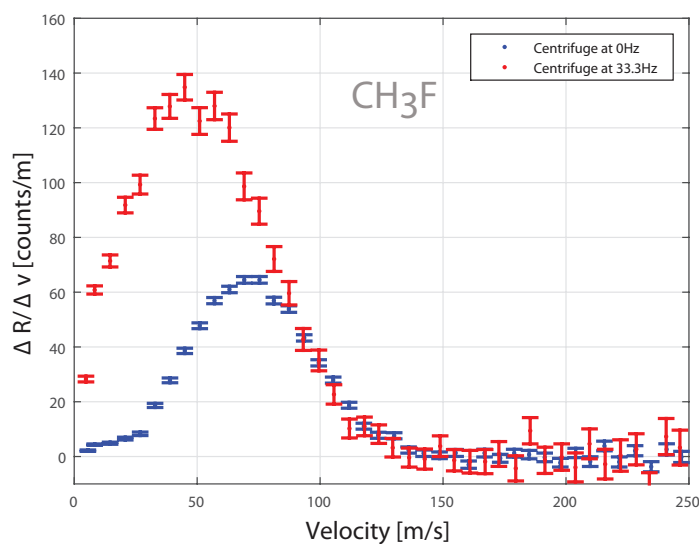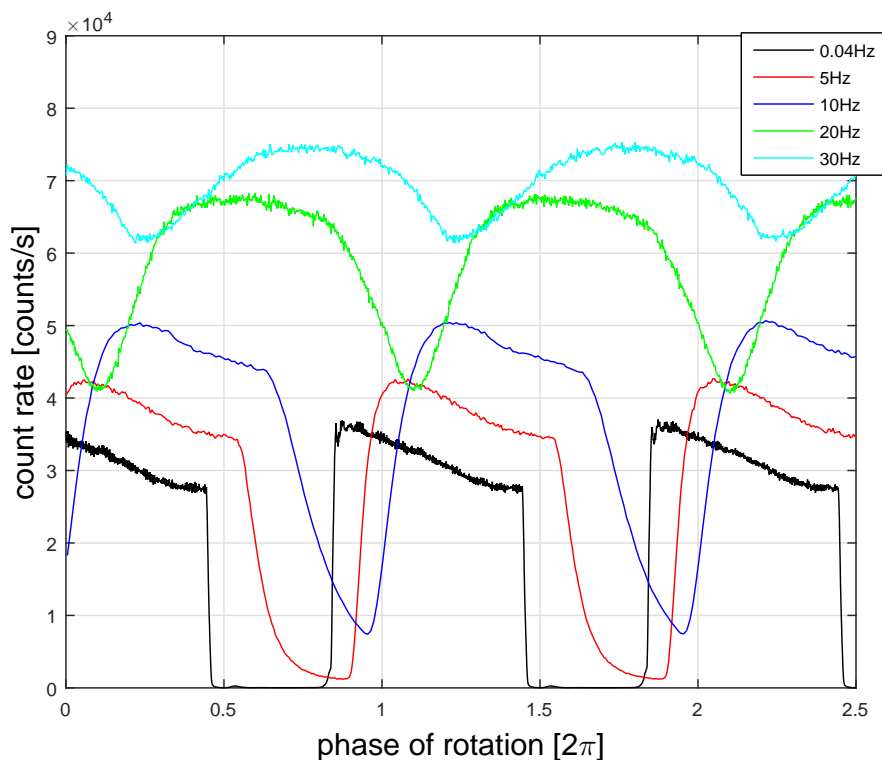Figure 4.4: *Continuous centrifuge output. The dependence of the output count rate on the phase position of the centrifuge is plotted for different rotation speeds. This measurement was conducted with CF_3H molecules produced with a nozzle at $125\,K$. All electric guides were kept constantly on at $\pm 5\,kV$.*

acquisition at the MCS card was synchronized with the phase of the rotation. This was achieved by using the built-in rotary encoder in the synchronous servomotor (Sec. 3.6.1), which returns the position and speed of the rotation precisely. Fig. 4.4 shows the dependence of the centrifuge output on the phase position at various rotation speeds. The vertical scale is the count rate, and the horizontal scale is the phase of the centrifuge rotation.

The continuity of the centrifuge deceleration is demonstrated very clearly in Fig. 4.4. At $0.04\,Hz$ (black curve), there is almost no deceleration, and the output signal is only from electric guiding through the centrifuge. The output signal is on for about 2/3 of the period, and off for the remaining 1/3, as expected from the gap on the peripheral guide (see Fig. 3.7 and Fig. 3.16(a)). As the centrifuge speeds up, three features are observed. Firstly, the output signal goes up with increasing rotational speed. This has been explained with Fig. 4.3. More molecules are decelerated to below the cut-off velocity of the $5\,cm$ radius exit-bend, resulting in an increase of output signal. Secondly, the phase of the signal appears delayed at higher rotation speeds. This is simply due to the shorter rotation period at higher
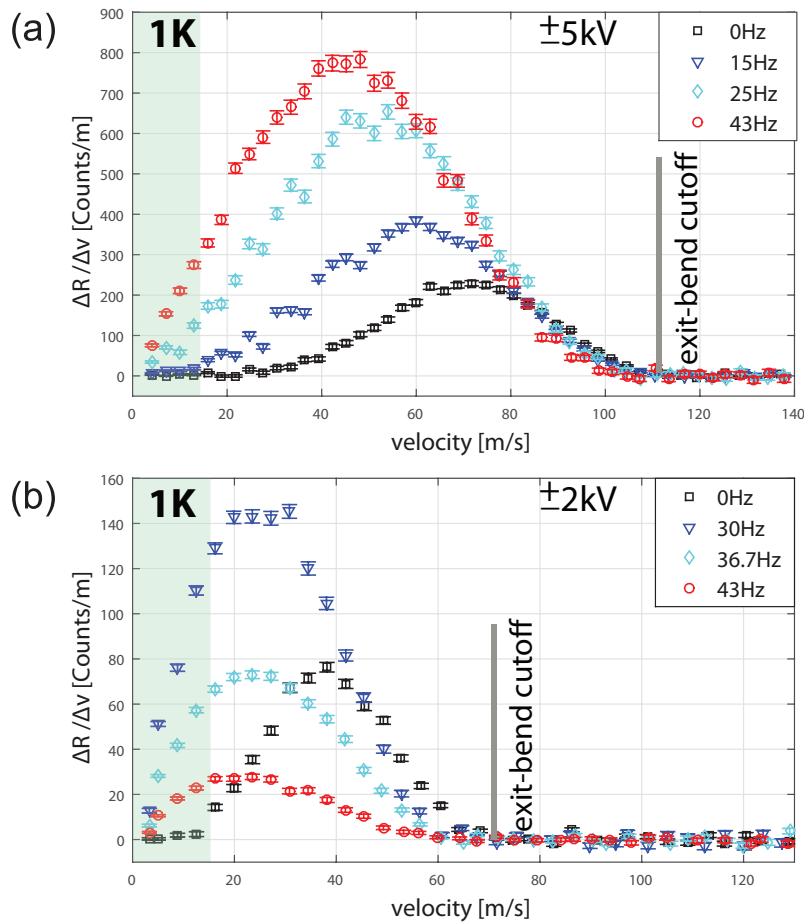
Figure 4.5: *Deceleration of CF₃H from a liquid-nitrogen-cooled source (at 138 K). (a) Longitudinal velocity distribution with 100 Pa nozzle pressure, ±5 kV guiding, for various centrifuge rotation speeds. (b) Longitudinal velocity distribution with 31 Pa nozzle pressure, ±2 kV guiding, for various centrifuge rotation speeds.*

rotation speeds. In fact, the phase delay in Fig. 4.4 is roughly proportional to the rotation speed, hence inversely proportional to the rotation period. Thirdly, the gaps in the output signal smears out at higher rotation speeds. On the one hand, this is due to deceleration. As molecules get slower, it takes them longer time to travel to the detector. This time scale becomes longer than the centrifuge rotation period at higher rotation speed. On the other hand, the velocity distribution gets broader when molecules are slower (see Sec. 3.2.2). Both effects contribute to smearing out of the gap in the output signal. At 30 Hz (cyan curve in Fig. 4.4), the output from the centrifuge is continuous, with a small periodic modulation superimposed on it.

4.4   Deceleration of pre-cooled beams

In this section, we present the deceleration results for CF_3H (mass= 70 u, $d = 1.65$ D), under three different conditions. The first measurement was made with 100 Pa pressure at a 138 K nozzle. HV of ± 5 kV was applied to all guiding segments (maximum electric field strength ~ 90 kVcm^{-1}), corresponding to a guide depth of 1.8 K for the lowest guidable state. The experimental results are shown in Fig. 4.5(a), and confirms the deceleration effects illustrated in Fig. 3.2. The measured velocity distributions correspond to the low-velocity part of the green shaded areas in Fig. 3.2. The lack of sharp fall-offs at the flanks stems from the transverse spatial distribution of the molecules in the guide as well as from the distribution of the input molecules over many guidable states with different Stark shifts [67, 68], and therefore with different cut-off velocities. The lack of slow molecules in the output signal for 0 Hz rotation is due to the boosting effect [69]. Collisions in the vicinity of the nozzle have higher chance to deplete the very slow molecules, as they spend longer time in the region with high densities. In Fig. 4.5(a), we observe very clearly a shift of the peak of the output velocity distribution and a manifold increase of the measured flux with increasing the rotation speed. Taking into account all the factors determining the detection efficiency, we measure a total output flux of molecules with kinetic energies below 1 K (≈ 15 m/s for CF_3H, highlighted in Fig. 4.5a) on the order of $\sim 3 \times 10^8$ s^{-1} for centrifuge rotation speed of 43 Hz.

Next, we demonstrate the effect of over-deceleration when the centrifuge rotates too fast, as illustrated by the upper curve in Fig. 3.2. In order to show this effect without actually spinning the centrifuge at very high speed, we reduced the input velocity by lowering the guiding voltage to ± 2 kV (maximum electric field strength ~ 36 kVcm^{-1}). This corresponds to a guide depth of 0.7 K for the lowest guidable state, leading to a significant decrease in the number of fast molecules at the input of the centrifuge. The experimental results are shown in Fig. 4.5(b). As seen, for rotation speeds above 30 Hz the signal progressively drops down. This result corresponds to the case presented by the upper curve in Fig. 3.2, where the majority of the input molecules have kinetic energies below the centrifugal potential and hence are repelled back before arriving at the output.

In the following, we look at the dependence of slow (< 1 K kinetic energy in the lab frame) flux of CF_3H on the nozzle pressure for a stationary centrifuge and a centrifuge spinning with 33 Hz rotation speed. The slow signal shown in Fig. 4.6 is equivalent to the green shaded area under the curves in Fig. 4.5(a). The signals obtained in the two cases differ significantly in their amplitudes. The increase of the source pressure produces a shift of the input distribution to higher velocities (boosting effect [69]), thus depleting the amount of slow molecules entering the centrifuge (almost no slow molecules at the input of the centrifuge) and consequently decreasing the measured signal of slow molecules for $\Omega = 0$ Hz (no deceleration takes place). For the centrifuge spinning at 33.3 Hz the deceleration overcomes the boosting effect and thus many initially fast molecules injected into the centrifuge exit
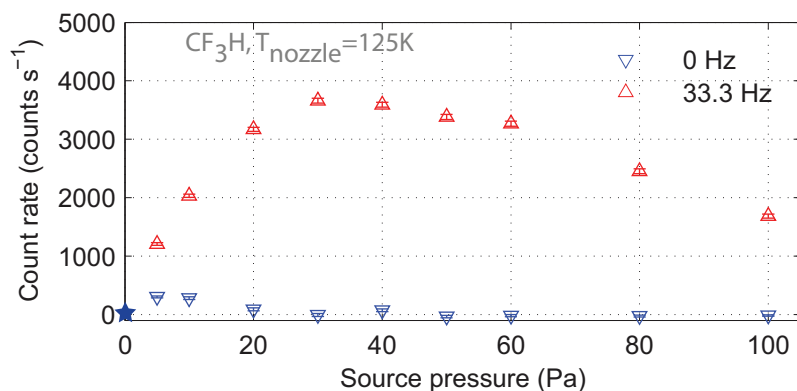
Figure 4.6: *Slow ($< 1\,K$ kinetic energy) signal vs. nozzle pressure of CF_3H at $125\,K$, for two different rotation speeds. $\pm 5\,kV$ was applied to all guiding segments.*
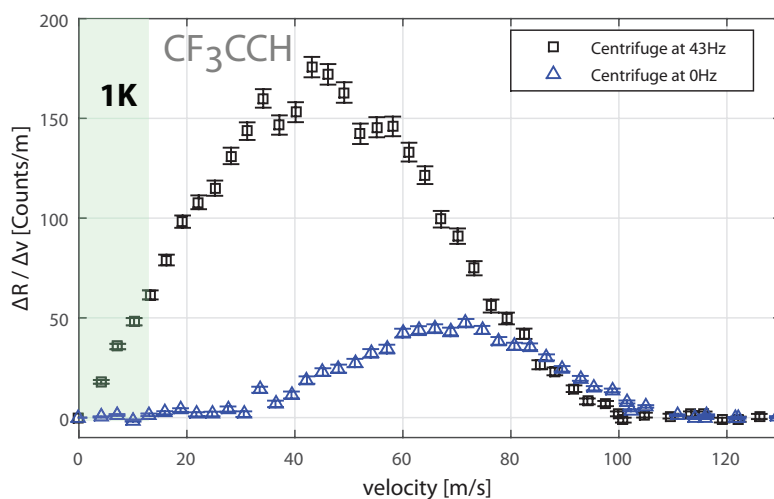
Figure 4.7: *Comparison of velocity distributions for CF_3CCH at $100\,Pa$ nozzle pressure and $219\,K$ nozzle temperature, at $0\,Hz$ and $43\,Hz$ centrifuge rotation speed, respectively.*

with velocities below $15\,\mathrm{ms^{-1}}$, which corresponds to $< 1\,\mathrm{K}$ kinetic energy in the lab frame. At $30\,\mathrm{Pa}$, the obtained count rate corresponds to a density of $\sim 1 \times 10^8\,\mathrm{cm^{-3}}$ and a flux of $6 \times 10^8\,\mathrm{s^{-1}}$ in the guide. Here, values of density and flux at the centrifuge output have a factor of 2 systematic error due to uncertainties in the detector sensitivity calibration.

4.5   Deceleration of larger molecules

To demonstrate the generality of the centrifuge deceleration, we have also performed measurements with a larger species CF_3CCH (mass$= 94\,\mathrm{u}$, $d = 2.36\,\mathrm{D}$). It consists

of 7 atoms and a $C \equiv C$ bond. Due to the relatively low vapor pressure of CF_3CCH, the nozzle needs to be heated up to about $220\,K$ to prevent freezing. All the electric guides were at $\pm 5\,kV$. Fig. 4.7 shows the comparison of the output velocity distributions obtained at a stationary centrifuge and at $43\,Hz$ rotation speed. Clearly, without turning the centrifuge, there is hardly any signal below $30\,m/s$. As already explained in Sec. 4.4, this is due to the boosting effect at the nozzle. When the centrifuge rotates at $43\,Hz$, a significant increase of the amount of slow molecules is observed in Fig. 4.7. The area under the $43\,Hz$ curve between 0 and $13\,m/s$ indicates the density of $CF_3CCH < 1\,K$ kinetic energy in the lab frame.

4.6 Measurement of the centrifuge efficiency

In Sec. 3.5.4, we have estimated from Monte-Carlo trajectory simulations a 7% centrifuge efficiency for decelerating molecules at $200\,m/s$ input velocity. In this section we verify the simulated efficiency with experimental results.

4.6.1 Supersonic input

The beam velocity of $200\,m/s$ can be produced by a supersonic expansion from a $20\,K$ Ne buffer-gas cell (refer to Eq. 2.3 in Sec. 2.1). This requires combining the centrifuge decelerator with the cryogenic buffer-gas cooling set-up. Such a combination has been accomplished during the final stage of this thesis, and will be described in detail in the doctoral thesis by Thomas Gantner. Here, only the result of a centrifuge deceleration of a supersonic beam is presented, which provides a comparison to the simulated centrifuge efficiency.

The result of decelerating a supersonic CH_3F beam is shown in Fig. 4.8. The input distribution was rescaled by a factor of 0.2 in order to be displayed at a similar amplitude with the output distribution. The vertical scale has already been converted to molecular density per velocity interval in the guide. The experimental conditions are summarized in the caption of Fig. 4.8. The peak of the input velocity distribution is at $165\,m/s$, which requires a much faster centrifuge rotation of $62\,Hz$ than the typical speed for decelerating effusive input beams.

The centrifuge efficiency for decelerating molecules at about $165\,m/s$ can be deduced from the data presented in Fig. 4.8. The blue area under the output distribution depicts the density below 1K. The corresponding input window is indicated by the red stripe. The vertical scale $\Delta n / \Delta v$ is proportional to the molecular phase space density, under the reasonable assumption that molecules fill the transverse phase space volume up to the trap depth. Additionally, we have explained in Sec. 3.2.2 that the centrifuge deceleration conserves the molecular phase space density, assuming no loss. Therefore, the ratio of the heights of the two colored area gives the output efficiency of the centrifuge decelerator, which is about 8%. This agrees very well with the prediction from trajectory simulations.
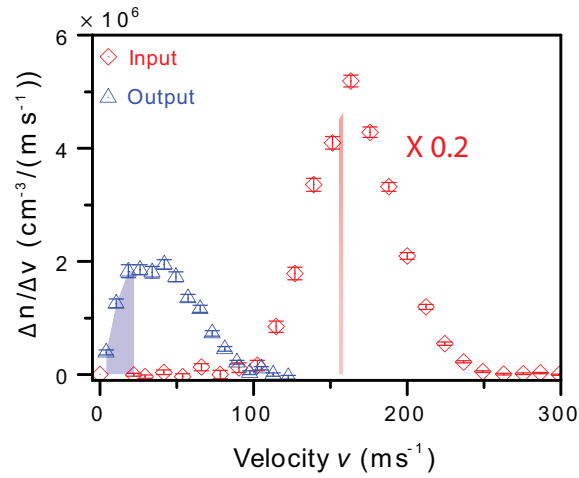
Figure 4.8: *Comparison of the input (rescaled by a factor of 0.2) and output velocity distributions of CH_3F, produced in the supersonic regime and decelerated by the centrifuge. The buffer-gas cell was at $17\,K$, Ne density was about $2 \times 10^{16}\,cm^{-3}$. The centrifuge was rotating at $62\,Hz$. The vertical scale is molecular density per velocity interval. The blue shaded area under the output curve indicates the density below $1\,K$, and the red stripe under the input curve is the corresponding input window for the $< 1\,K$ output.*
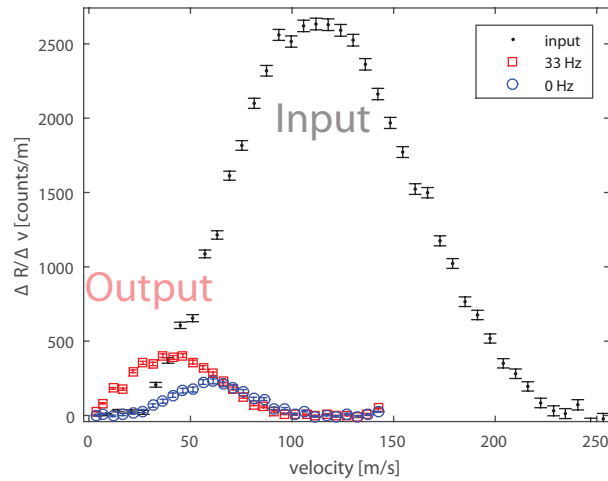
Figure 4.9: *Comparison of the input and the output velocity distributions of a CF_3H effusive beam decelerated by the centrifuge. The molecular beams were produced by a room-temperature nozzle at $60\,Pa$ pressure. The centrifuge was operated in two regimes, stationary (blue) or $33\,Hz$ rotation speed (red). The vertical scale is in count rates per velocity interval, directly obtained from differentiating the time-of-flight signal.*

4.6.2 Effusive input

The efficiency for decelerating an effusive beam can be measured without using a cryogenic buffer-gas cell as a source of molecules. We performed this measurement with a CF_3H beam, produced at room temperature, and $60\,Pa$ nozzle pressure. Fig. 4.9 shows a comparison of the input and two output distributions, obtained at either a stationary centrifuge, or at $33\,Hz$ rotation speed. No rescaling has been applied to the amplitude of the input distribution. As discussed in Sec. 4.6.1, the vertical scale in the plot is proportional to the phase space density of the molecules. Thus, the ratio of the heights of the red and black plots gives a rough estimate of the centrifuge efficiency for the effusive beam, which is $\sim 15\%$. The real efficiency would be somewhat higher than this value because the faster input distribution has a smaller beam divergence to the detector, and this is not included in the plots shown in Fig. 4.9. A more systematic measurement with effusive beams from a buffer-gas cell, and with the beam divergence included, has confirmed a 20% efficiency of our centrifuge. This more recent work will be included in the doctoral thesis by Thomas Gantner.

It is not surprising that the centrifuge guiding efficiency is higher for effusive beams than for supersonic beams. Beams with smaller longitudinal velocities can have better transverse confinement in a bent electric guide, where the transverse confinement is weakened by the centrifugal potential of molecules [48]. Thus, effusive beams can be better guided around the periphery of the centrifuge, as well as in the rotating spiral of the centrifuge.

4.7 Systematics in the TOF measurement

Most of the results shown in this chapter have been obtained from TOF measurements, with the simple scheme outlined in Sec. 4.1. In the actual TOF measurements, however, a number of systematic effects have appeared. These are discussed in this section, including the velocity dependence of the QMS sensitivity, the 'space-charge-effect' in the QMS ionization volume, and the background-pressure pumping effect. Each of the these effects will be treated comprehensively in the subsections below.

4.7.1 Velocity dependence of the QMS sensitivity

It has been confirmed in a measurement by Michael Motsch that the QMS signal is proportional to molecular density [70]. While this conclusion is generally true, it does not hold for the very slow ($< 1\,K$ kinetic energy) molecules from an electric guide. Instead, the QMS signal for these very slow molecules are proportional to their flux. Of course, this effect has not been relevant until the centrifuge decelerator became available.
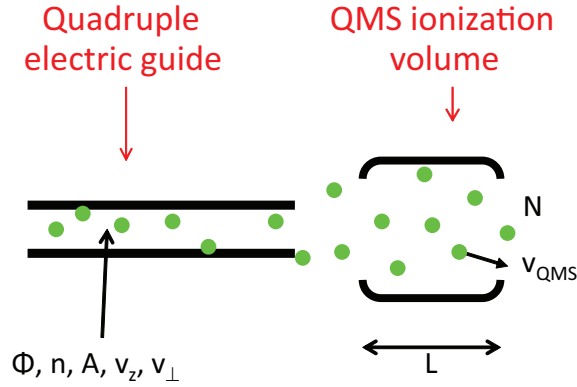
Figure 4.10: *Sketch of the interface between the electric guide and the QMS ionization volume. The green spheres represent molecules. The relevant quantities are labeled in the figure. In the quadrupole electric guide, molecules have a flux Φ, density n, guiding cross section A, longitudinal velocity v_z, and transverse velocity $v_\perp$. In the QMS ionization volume, molecules have a total particle number N and total velocity v_{QMS}. The ionization volume has a dimension L.*

The reason is explained in the following, and Fig. 4.10 helps to visualize this process. The QMS detects the incoming molecules via electron beam impact ionization. As the electrons move much faster than the molecules, the QMS signal S at a given instant of time is proportional to the number of molecules N present in the ionization volume. On the other hand, N is proportional to the product of the molecule flux entering the ionization volume, $\Phi_{QMS} \propto \Phi$ and the time molecules spend inside it $\tau \approx L/v_{QMS}$, where Φ, L, and v_{QMS} are all defined in the caption of Fig. 4.10. Thus, we expect,

$$S \propto N \propto \Phi \cdot \tau = (n \cdot A \cdot v_z) \cdot \frac{L}{v_{QMS}} \propto \frac{n \cdot v_z}{v_{QMS}}. \tag{4.1}$$

When molecules fly from the electric guide towards the QMS, their transverse potential energy in the guide is converted into their kinetic one. Thus, their velocity in the QMS, $v_{QMS} = \sqrt{v_z^2 + v_\perp^2}$, where v_z and $v_\perp$ are defined in the caption of Fig. 4.10, and $v_\perp \sim 1\,\mathrm{K}$, the transverse trap depth. Therefore, we have the following two limiting cases.

- when $v_z \gg v_\perp \sim 1\,\mathrm{K}$, $v_{QMS} = \sqrt{v_z^2 + v_\perp^2} \approx v_z$. Consequently, Eq. 4.1 becomes $S \propto (n \cdot v_z)/v_{QMS} \approx n$, hence the QMS signal is proportional to the molecular density, as confirmed by Michael Motsch [70].

- when $v_z \ll v_\perp \sim 1\,\mathrm{K}$, $v_{QMS} = \sqrt{v_z^2 + v_\perp^2} \approx v_\perp \sim 1\,\mathrm{K}$. Eq. 4.1 reduces to $S \propto (n \cdot v_z)/v_{QMS} \propto (n \cdot v_z) \propto \Phi$. Thus, the QMS signal is approximately proportional to the molecular flux, for molecules below $1\,\mathrm{K}$ kinetic energy.

This velocity dependence of the QMS sensitivity is essentially due to the acceleration of molecules after they leave the electric guide. This acceleration is negligible
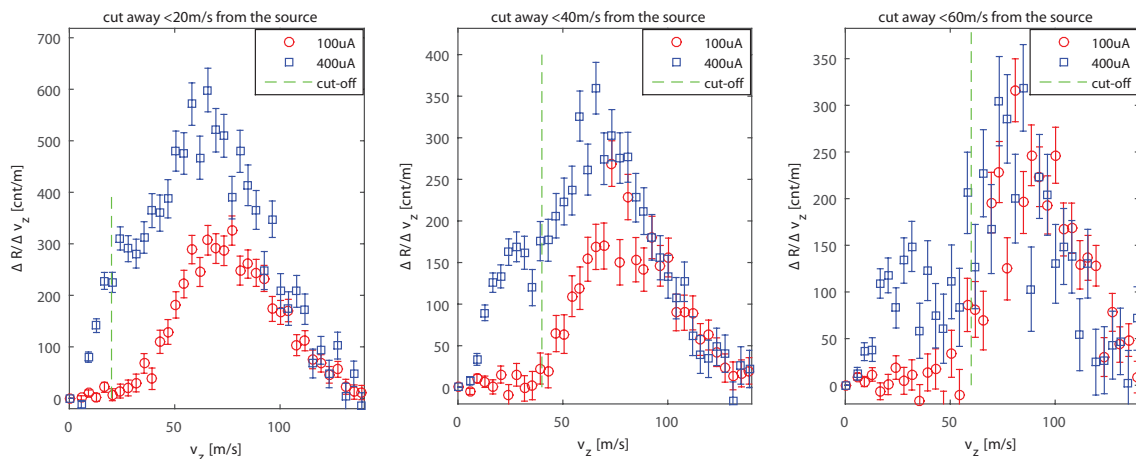
Figure 4.11: *Comparison of velocity distributions, measured with $100\,\mu A$ and with $400\,\mu A$ emission current on the QMS. From left to right, the three figures show the measured distributions from a source with no molecules below $20\,m/s$, $40\,m/s$, and $60\,m/s$, respectively.*

if molecules are originally much faster than $1\,K$. However, it makes the detection sensitivity velocity dependent, if molecules are slower than $1\,K$ in the guide, e.g. after the centrifuge deceleration.

4.7.2 'Space-charge-effect'

The electron beam in the detection volume is responsible for ionizing the incoming molecules, but it can also alter the temporal response if the electron current is too high. This is known as the 'space-charge-effect' in literature [71]. When the electron cloud in the detection volume is dense enough, it disturbs the extraction of the produced ions via electrostatic interaction, and subsequently causes a delay in the arriving time at the ion-counter [72]. As a result, the measured v_z-distribution would appear slower than the actual one.

This is very clearly demonstrated in Fig. 4.11, which shows velocity distributions measured with $100\,\mu A$ and with $400\,\mu A$ emission current on the QMS. The higher the emission current, the denser the electron cloud in the ionization volume. In these measurements, no centrifuge deceleration was applied, and the signals were produced from electrostatic guiding from a room temperature source. In addition, to verify the temporal response, we applied the segmented guiding technique [73], which deplete molecules slower than $20\,m/s$, $40\,m/s$, and $60\,m/s$, respectively, from the source. Thus, in Fig. 4.11, signals below the corresponding cut-off velocities (the green dashed lines) should be absent. In all three tests, the $400\,\mu A$ measurements gave 'fake' signals below the cut-off velocities, while the $100\,\mu A$ measurements consistently follow the minimum velocities of the inputs.

Moreover, to verify whether the emission current was sufficiently low to avoid the 'space-charge-effect', we compared the velocity distribution measured at $100\,\mu A$ with
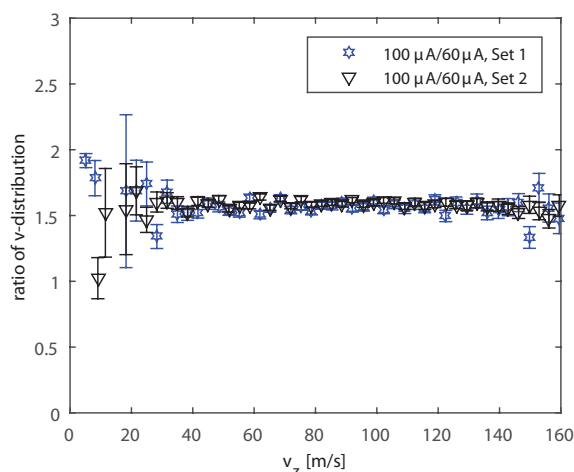
Figure 4.12: *Ratio of velocity distributions taken at* $100\,\mu A$ *and at* $60\,\mu A$
*QMS emission current, respectively. The two sets correspond to measure-
ments carried out on two different days.*

the one measured at $60\,\mu A$, and checked whether the detector responded linearly
in this range. The ratio between these two velocity distributions at $100\,\mu A$ and
at $60\,\mu A$ is shown in Fig. 4.12. Two sets of comparisons were measured on two
different days. The ratios of the two sets overlap and are flat. This confirms that
the distribution measured at $100\,\mu A$ has the same shape as the one measured at
$60\,\mu A$, and hence our QMS behaves linearly in this range of electron current. The
large error bars at velocities below $30\,m/s$ were due to the lack of slow signals, as
molecules were not decelerated in these measurements.

Thus, in all the measurements, we were forced to reduce the electron emission
current to $100\,\mu A$, instead of the typical range of 400 to $600\,\mu A$ for a general appli-
cation of the QMS recommended by the manufacturer.

4.7.3   Background-pressure pumping effect

Last but not least, we will discuss the influence of background pressure pumping
on the TOF signal. We noticed a small rising-slope in the TOF signal when HV
is turned on, even after the TOF signal is expected to reach a steady-state value.
This can be seen on the raw TOF data in Fig. 4.13(a) (black data points). Taking
a time-derivative of such TOF data would result in artificial signals of very slow
molecules, as shown by the velocity distribution derived from the raw TOF data in
Fig. 4.13(b). To avoid such a systematic effect, all the data above a given threshold,
typically 99%, of the TOF steady-state value, were excluded in the evaluation of the
velocity distribution in the past [69].

For the output of the centrifuge deceleration, however, this is no longer applica-
ble, since we are interested in precisely these very slow molecules. Instead, we have
found out the cause for this artifact, the background pressure pumping effect in the
detection chamber. In the following, we show how it can be removed from the data
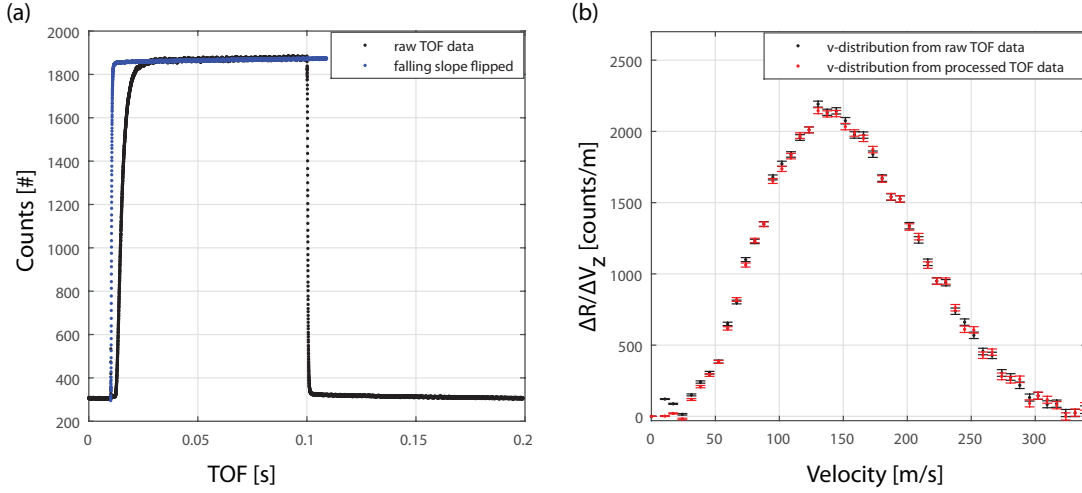
Figure 4.13: *(a) Time-of-flight signal and (b) the derived velocity distribution without and with canceling the background-pressure pumping effect. The measurement was made with molecule beams from a room temperature nozzle, before the centrifuge input, i.e. no deceleration was applied.*

analysis.

Pumping rate

The ultra high vacuum in a detection chamber is typically produced by an ion getter pump, with an approximately constant pumping speed S_p for a given pressure range. S_p is conventionally defined as the volume evacuated per unit time (in the unit of e.g. [L/s]). Assuming the pressure, temperature, and volume of the detection chamber are p, T, and V, respectively, the rate at which molecule density is pumped out from the detection chamber, $\dot{n}_{pump}$ is given by

$$pS = \dot{n}_{pump}kT, \tag{4.2}$$

where k is the Boltzmann factor. Under the assumption of the ideal gas law $p = nkT/V$, we get from Eq. 4.2,

$$\dot{n}_{pump} = \frac{S}{V}n, \tag{4.3}$$

Input rate

When the TOF guide is turned on, molecules enter into the detection chamber. Once the input reaches the steady-state, i.e. molecules at all velocity classes have arrived at the detector, the incoming flux becomes constant.

$$\dot{n}_{input} = \frac{\Phi_{input}}{V} = \frac{\bar{v}A_{input}}{V}n_{input} = const., \tag{4.4}$$

where Φ_{input} is the input flux, $\bar{v}$, A, and n are the average velocity, the area of the guide cross section (see Fig. 1.1(c)), and density, respectively, of the incoming molecules in the guide. The density or pressure equilibrium of the detection chamber requires the total density in the detection chamber to satisfy $\dot{n} = 0$.

Rate equation

The rate equation for molecular density inside the detection chamber is given by

$$\dot{n} = \dot{n}_{input} - \dot{n}_{pump} = \frac{\bar{v}A_{input}}{V}n_{input} - \frac{S}{V}n. \tag{4.5}$$

The equilibrium condition is obtained when $\dot{n} = 0$, i.e.

$$\frac{S}{V}n_{eq} = \frac{\bar{v}A_{input}}{V}n_{input} = const., \tag{4.6}$$

where n_{eq} is the density at equilibrium. The solution of Eq. 4.5 with the boundary condition Eq. 4.6 is then

$$n = n_{eq} - n_0 exp(-\frac{t}{\tau_{on}}), \tag{4.7}$$

where the amplitude of the exponential n_0 needs an additional condition to determine, and the time constant for the rising slope $\tau_{on} = V/S$. For our QMS chamber, $V \sim 5\,\text{L}$, $S \sim 50\,\text{L/s}$, and $\tau_{on} \sim 100\,\text{ms}$.

Rate equation with the guide turned off

When the TOF guide is turned off, $\dot{n}_{input} = 0$, and the rate equation reduces to,

$$\dot{n} = -\dot{n}_{pump} = -\frac{S}{V}n. \tag{4.8}$$

The solution is simply,

$$n = n_0' exp(-\frac{t}{\tau_{off}}), \tag{4.9}$$

where the time constant for the falling slope $\tau_{off} = V/S$.

From the above results, it is clear that the slow rising-slope and the falling-slope in Fig. 4.13(a) share an identical time constant, which is the time scale for pumping the detection chamber. Thus, these two slopes should be identical to each other except the sign. That is why overlapping the slow falling slope when the guide turns off with the slow rising slope when the guide turns on (see Fig. 4.13(a)) is justified. Hence we can subtract this background pumping effect in the rising slope and obtain a clean velocity distribution for small velocities (see Fig. 4.13(b))

4.8   Summary

In this chapter, we have presented the first proof-of-principle demonstration of the centrifuge deceleration of polar molecules. The first signal and deceleration was obtained with CH_3F molecules from a room-temperature nozzle. The continuity of the centrifuge output was demonstrated with the signal versus rotation phase measurement. We have shown that at about 30 Hz rotation speed, which is typically required for slowing down molecules from an effusive source, the centrifuge output is continuous. With a liquid-nitrogen-cooled CF_3H effusive source, we have obtained slow (< 1 K kinetic energy in the lab frame) molecules with a flux and density of $6 \times 10^8 \, \mathrm{s^{-1}}$ and $\sim 10^8 \, \mathrm{cm^{-3}}$, respectively. The deceleration of a larger species, CF_3CCH has also been demonstrated.

We have verified the centrifuge guiding efficiency for decelerating a supersonic beam generated from a cryogenic buffer-gas cell. The measurement has shown about 8% efficiency for an input velocity of about 165 m/s, in a very good agreement with the results from Monte-Carlo trajectory simulations in Sec. 3.5.4. For deceleration of an effusive beam, the centrifuge efficiency has been estimated to be about 15% to 20%.

In addition, we have explained and accounted for the three most significant systematic effects in the TOF measurement in our system. They include the velocity dependence of the QMS sensitivity, the 'space-charge-effect' in the ionization volume, and the artificial slow signals due to background pressure pumping in the detection chamber.

The centrifuge decelerator demonstrated here employs solely an inertial force, a universal means for deceleration. Thus it can be applied to any guidable molecule, and in principle also to atoms and even neutrons [74]. Once assembled, the decelerator does not require a sophisticated control, it is robust and easy to operate.

Chapter 5

Outlook

This thesis has covered two main topics. Firstly, a simple but extremely robust internal-state detection technique for cold polyatomic molecules has been presented. It is based on a resonant radio-frequency depletion spectroscopy, which is capable of resolving both the rotational and hyperfine states of polyatomic molecules. In combination with a full Monte-Carlo trajectory simulation, the above technique is extended into a thermometry method, which enables a comprehensive characterization of buffer-gas cooling of polyatomic molecules. Secondly, a novel molecular deceleration method, which employs only a centrifugal force in a rotating frame, has been demonstrated. As the basic principle of the deceleration is independent of any specific internal structure of the molecules, it is a very generic method, which could be applied even to slowing down atoms and neutrons. The design concept of the centrifuge decelerator enables continuous deceleration, which tremendously improves the duty cycle and the efficiency of the production of slow molecules, compared to all of the existing molecular deceleration methods.

Both the buffer-gas cooling and the centrifuge deceleration have exhibited great performance when operated separately. A natural further step is the combination of the two techniques, which is expected to deliver cold molecules below $k_B \cdot 1\,\mathrm{K}$ at unprecedented rates.

Cryofuge

The combination of the cryogenic buffer-gas-cooling technique and the centrifuge deceleration gives rise to a new method for the production of cold and slow molecules named *Cryofuge* to emphasize the two components it consists of. The cryofuge has just been realized during the final stage of this thesis, and the results from it will be covered in great detail in the doctoral thesis of Thomas Gantner, as well as in a dedicated publication [75]. We have demonstrated the capabilities of the cryofuge by showing internal-state cooling and deceleration of the test molecule fluoromethane (CH_3F). The generality of the method is demonstrated by an extension to several other cold species, including ammonia (ND_3), methanol (CH_3OH), tri-

fluoromethylacetylene (CF_3CCH), and isopropanol (C_3H_8O). Fluxes and densities of over $10^{10}\,s^{-1}$ and $10^9\,cm^{-3}$, respectively, have been achieved at kinetic energies below $\sim k_B \cdot 1\,K$ at the output of the cryofuge. This outperforms all existing sources by several orders of magnitude. The high density of the decelerated molecules also enables the observation of cold dipolar collisions.

Cold dipolar collisions

At the output of the cryofuge, we have measured a collision rate of $\sim 10\,Hz$ between polar molecules [75]. This corresponds to a collision cross section of $\sim 10^{-12}\,cm^2$, at collision energy of $\sim k_B \cdot 1\,K$ and density of $\sim 10^9\,cm^{-3}$. Thus, even at $\sim 1\,K$ temperature, we have already achieved an interaction length $a \sim 200\,a_0$, where a_0 is the Bohr radius, greater than the s-wave scattering length of ultra cold rubidium atoms. Such a large interaction length results from the strong electric dipolar interaction. Moreover, as the temperature decreases, the dipolar scattering cross section $\sigma \propto d^2/\sqrt{T}$ [14], where d is the dipole moment of the molecules, will increase until entering the quantum limit when the collision becomes a single-partial-wave process. In the quantum limit, the value of a can be as large as $\sim 1\,\mu m$ (Sec. 1.1.1). The explorations of these collisions with such gigantic interaction strengths are of great interest for quantum chemistry [76] as well as for evaporative cooling of molecules to quantum degeneracy [77, 78]. The long-range dipole-dipole interaction also facilitates novel strongly correlated [79, 80] and dipole blockaded [81, 82, 83] systems that, in contrast to short-lived atomic Rydberg systems, promise a practically infinite lifetime.

High-precision measurements and further cooling

In addition to enabling the observation of cold dipolar collisions, the versatility of the centrifuge could drastically extend the scope of the current cold-molecule research, e.g., the cold beams of methanol we have produced could be well-suited for measuring the proton-to-electron mass ratio, as introduced in Sec. 1.1.2. The production of intense beams of cold and slow YbF molecules would also boost the eEDM measurement [84], in terms of providing much longer interaction length due to the slow velocity and a short measurement time from the enhanced signal level. Moreover, the centrifuge could serve as an ideal source for ongoing experiments with laser cooling of diatomic molecules [36, 39] and the optoelectrical Sisyphus cooling of polyatomic molecules [42], as many of the species considered in both approaches possess rotational states with very favourable Stark shifts for applying the centrifuge technique.

Bibliography

[1] M. W. Zemansky and R. H. Dittman. *Heat and Thermodynamics*. THE McGRAW-HILL COMPANIES, INC, 1997.

[2] Ben Spaun, P. Bryan Changala, David Patterson, Bryce J. Bjork, Oliver H. Heckl, John M. Doyle, and Jun Ye. Continuous probing of cold complex molecules with infrared frequency comb spectroscopy. *Nature*, 533(7604):517, Sept 2016.

[3] Andreas Reiserer, Stephan Ritter, and Gerhard Rempe. Nondestructive detection of an optical photon. *Science*, 342(6164):1349–1351, 2013.

[4] Martin T Bell and Timothy P Softley. Ultracold molecules and ultracold chemistry. *Mol. Phys.*, 107(2):99–132, 2009.

[5] W. Ketterle. Nobel lecture: When atoms behave as waves: Bose-Einstein condensation and the atom laser. *Rev. Mod. Phys.*, 74:1131, 2002.

[6] Sebastiaan Y. T. van de Meerakker, Hendrick L. Bethlem, Nicolas Vanhaecke, and Gerard Meijer. Manipulation and control of molecular beams. *Chem. Rev.*, 112(9):4828–4878, Sep 2012.

[7] Lincoln D. Carr, David DeMille, Roman V. Krems, and Jun Ye. Cold and ultracold molecules: science, technology and applications. *New J. Phys.*, 11:055049, 2009.

[8] P. Dietiker, E. Miloglyadov, M. Quack, A. Schneider, and G. Seyfang. Infrared laser induced population transfer and parity selection in 14nh3: A proof of principle experiment towards detecting parity violation in chiral molecules. *The Journal of Chemical Physics*, 143(24), 2015.

[9] Paul Jansen, Li-Hong Xu, Isabelle Kleiner, Wim Ubachs, and Hendrick L. Bethlem. Methanol as a sensitive probe for spatial and temporal variations of the proton-to-electron mass ratio. *Phys. Rev. Lett.*, 106:100801, Mar 2011.

[10] J. J. Hudson, D. M. Kara, I. J. Smallman, B. E. Sauer, M. R. Tarbutt, and E. A. Hinds. Improved measurement of the shape of the electron. *Nature*, 473:493–496, 2011.

[11] H. J. Metcalf and P. van der Straten. *Laser Cooling and Trapping.* Springer, New York, 1999.

[12] J. Loreau and A. van der Avoird. Scattering of nh3 and nd3 with rare gas atoms at low collision energy. *The Journal of Chemical Physics*, 143(18), 2015.

[13] A. B. Henson, S. Gersten, Y. Shagam, J. Narevicius, and E. Narevicius. Observation of resonances in penning ionization reactions at sub-kelvin temperatures in merged beams. *Science*, 338(6104):234–238, 2012.

[14] J L Bohn, M Cavagnero, and C Ticknor. Quasi-universal dipolar scattering in cold and ultracold gases. *New Journal of Physics*, 11(5):055039, 2009.

[15] D. DeMille. Quantum computation with trapped polar molecules. *Physical Review Letters*, 88(6):067901/1–4, 2002.

[16] E. A. Hinds. Testing time reversal symmetry using molecules. *Phys. Scr.*, T70(34), 1997.

[17] A. C. Vutha, B. Spaun, Y. V. Gurevich, N. R. Hutzler, E. Kirilov, J. M. Doyle, G. Gabrielse, and D. DeMille. Magnetic and electric dipole moments of the h $^3\Delta_1$ state in tho. *Phys. Rev. A*, 84:034502, Sep 2011.

[18] S. Eckel, P. Hamilton, E. Kirilov, H. W. Smith, and D. DeMille. Search for the electron electric dipole moment using Ω-doublet levels in pbo. *Phys. Rev. A*, 87:052130, May 2013.

[19] , J. Baron, W. C. Campbell, D. DeMille, J. M. Doyle, G. Gabrielse, Y. V. Gurevich, P. W. Hess, N. R. Hutzler, E. Kirilov, I. Kozyryev, B. R. O'Leary, C. D. Panda, M. F. Parsons, E. S. Petrik, B. Spaun, A. C. Vutha, and A. D. West. Order of magnitude smaller limit on the electric dipole moment of the electron. *Science*, 343(6168):269–272, 2014.

[20] Jean-Philippe Uzan. The fundamental constants and their variation: observational and theoretical status. *Rev. Mod. Phys.*, 75:403–455, Apr 2003.

[21] Julija Bagdonaite, Paul Jansen, Christian Henkel, Hendrick L. Bethlem, Karl M. Menten, and Wim Ubachs. A stringent limit on a drifting proton-to-electron mass ratio from alcohol in the early universe. *Science*, 339(6115):46–48, 2013.

[22] Marcelino Agúndez and Valentine Wakelam. Chemistry of dark clouds: Databases, networks, and models. *Chemical Reviews*, 113(12):8710–8737, 2013. PMID: 24099569.

[23] Edwin Bergin and Mario Tafalla. Cold dark clouds: The initial conditions for star formation. *Annu. Rev. Astron. Astrophys.*, 45:339–396, 2007.

[24] Oskar Asvany, Koichi M. T. Yamada, Sandra Brünken, Alexey Potapov, and Stephan Schlemmer. Experimental ground-state combination differences of ch5+. *Science*, 347(6228):1346–1349, 2015.

[25] Sandra Brünken, Lars Kluge, Alexander Stoffels, Oskar Asvany, and Stephan Schlemmer. Laboratory rotational spectrum of l-c3h+ and confirmation of its astronomical detection. *The Astrophysical Journal Letters*, 783(1):L4, 2014.

[26] K.-K. Ni, S. Ospelkaus, M. H. G. de Miranda, A. Pe'er, B. Neyenhuis, J. J. Zirbel, S. Kotochigova, P. S. Julienne, D. S. Jin, and J. Ye. A High Phase-Space-Density Gas of Polar Molecules. *Science*, 322:231, 2008.

[27] Johann G. Danzl, Elmar Haller, Mattias Gustavsson, Manfred J. Mark, Russell Hart, Nadia Bouloufa, Olivier Dulieu, Helmut Ritsch, and Hanns-Christoph Nägerl. Quantum Gas of Deeply Bound Ground State Molecules. *Science*, 321:1062–1066, 2008.

[28] H. L. Bethlem, G. Berden, and G. Meijer. Decelerating neutral dipolar molecules. *Physical Review Letters*, 83(8):1558–1561, 1999.

[29] E. Narevicius, A. Libson, C. G. Parthey, I. Chavez, J. Narevicius, U. Even, and M. G. Raizen. Stopping supersonic beams with a series of pulsed electromagnetic coils: An atomic coilgun. *Phys. Rev. Lett.*, 100:93003, 2008.

[30] M. Gupta and D. Herschbach. Slowing and speeding molecular beams by means of a rapidly rotating source. *Journal of Physical Chemistry A*, 105(9):1626–1637, 2001.

[31] M. Strebel, F. Stienkemeier, and M. Mudrich. Improved setup for producing slow beams of cold molecules using a rotating nozzle. *Phys. Rev. A*, 81(3):033409, Mar 2010.

[32] D. H. Levy. Laser spectroscopy of cold gas-phase molecules. *Ann. Rev. Phys. Chem.*, 31:197–225, 1980.

[33] M. D. Di Rosa. Laser-cooling molecules - concept, candidates, and supporting hyperfine-resolved measurements of rotational lines in the a-x(0,0) band of cah. *European Physical Journal D*, 31(2):395–402, 2004.

[34] E. S. Shuman, J. F. Barry, and D. DeMille. Laser cooling of a diatomic molecule. *Nature*, 467(7317), 2010.

[35] Matthew T. Hummon, Mark Yeo, Benjamin K. Stuhl, Alejandra L. Collopy, Yong Xia, and Jun Ye. 2d magneto-optical trapping of diatomic molecules. *Phys. Rev. Lett.*, 110:143001, Apr 2013.

[36] V. Zhelyazkova, A. Cournol, T. E. Wall, A. Matsushima, J. J. Hudson, E. A. Hinds, M. R. Tarbutt, and B. E. Sauer. Laser cooling and slowing of caf molecules. *Phys. Rev. A*, 89:053416, May 2014.

[37] Boerge Hemmerling, Eunmi Chae, Aakash Ravi, Loic Anderegg, Garrett K Drayna, Nicholas R Hutzler, Alejandra L Collopy, Jun Ye, Wolfgang Ketterle, and John M Doyle. Laser slowing of caf molecules to near the capture velocity of a molecular mot. *Journal of Physics B: Atomic, Molecular and Optical Physics*, 49(17):174001, 2016.

[38] J. F. Barry, D. J. McCarron, E. B. Norrgard, M. H. Steinecker, and D. DeMille. Magneto-optical trapping of a diatomic molecule. *Nature*, 512(7514):286–289, August 2014.

[39] E. B. Norrgard, D. J. McCarron, M. H. Steinecker, M. R. Tarbutt, and D. DeMille. Submillikelvin dipolar molecules in a radio-frequency magneto-optical trap. *Phys. Rev. Lett.*, 116:063004, Feb 2016.

[40] Martin Zeppenfeld, Barbara G. U. Englert, Rosa Glöckner, Alexander Prehn, Manuel Mielenz, Christian Sommer, Laurens D. van Buuren, Michael Motsch, and Gerhard Rempe. Sisyphus cooling of electrically trapped polyatomic molecules. *Nature*, 491(7425):570–573, November 2012.

[41] M. Zeppenfeld, M. Motsch, P. W. H. Pinkse, and G. Rempe. Optoelectrical cooling of polar molecules. *Phys. Rev. A*, 80(4):041401, Oct 2009.

[42] Alexander Prehn, Martin Ibrügger, Rosa Glöckner, Gerhard Rempe, and Martin Zeppenfeld. Optoelectrical cooling of polar molecules to submillikelvin temperatures. *Phys. Rev. Lett.*, 116:063005, Feb 2016.

[43] J.D. Weinstein, R. DeCarvalho, T. Guillet, B. Friedrich, and J.M. Doyle. Magnetic trapping of calcium monohydride molecules at millikelvin temperatures. *Nature*, 395(6698):148–50, 1998.

[44] B. G. U. Englert, M. Mielenz, C. Sommer, J. Bayerl, M. Motsch, P. W. H. Pinkse, G. Rempe, and M. Zeppenfeld. Storage and adiabatic cooling of polar molecules in a microstructured trap. *Phys. Rev. Lett.*, 107:263003, Dec 2011.

[45] S.A. Rangwala, T. Junglen, T. Rieger, P.W.H. Pinkse, and G. Rempe. Continuous source of translationally cold dipolar molecules. *Physical Review A (Atomic, Molecular, and Optical Physics)*, 67(4):43406–1–4, 2003.

[46] L. D. van Buuren, C. Sommer, M. Motsch, S. Pohle, M. Schenk, J. Bayerl, P. W. H. Pinkse, and G. Rempe. Electrostatic extraction of cold molecules from a cryogenic reservoir. *Phys. Rev. Lett.*, 102(3):033001, Jan 2009.

[47] D. Patterson and J. M. Doyle. Bright, guided molecular beam with hydrodynamic enhancement. *Journal of Chemical Physics*, 126(15), 2007.

[48] C. Sommer. *Construction and Operation of a Source for Cold Polar Molecules.* PhD thesis, Technische Universität München, Garching bei München, Germany, February 2011.

[49] M. Motsch, C. Sommer, M. Zeppenfeld, L D van Buuren, G. Rempe, and P W H Pinkse. Collisional effects in the formation of cold guided beams of polar molecules. *New J. Phys.*, 11:055030, 2009.

[50] S. E. Maxwell, N. Brahms, R. deCarvalho, D. R. Glenn, J. S. Helton, S. V. Nguyen, D. Patterson, J. Petricka, D. DeMille, and J. M. Doyle. High-flux beam source for cold, slow atoms or molecules. *Physical Review Letters*, 95(17):173201, 2005.

[51] David Patterson and John M. Doyle. Cooling molecules in a cell for ftmw spectroscopy. *Molecular Physics*, 110(15-16):1757–1766, 2012.

[52] David Patterson and John M. Doyle. A slow, continuous beam of cold benzonitrile. *Phys. Chem. Chem. Phys.*, 17:5372–5375, 2015.

[53] William D. Phillips and Harold Metcalf. Laser deceleration of an atomic beam. *Phys. Rev. Lett.*, 48:596–599, Mar 1982.

[54] Xing Wu, Thomas Gantner, Martin Zeppenfeld, Sotir Chervenkov, and Gerhard Rempe. Thermometry of guided molecular beams from a cryogenic buffer-gas cell. *ChemPhysChem*, 17(22):3631–3640, 2016.

[55] Christian Sommer, Laurens D. van Buuren, Michael Motsch, Sebastian Pohle, Josef Bayerl, Pepijn W. H. Pinkse, and Gerhard Rempe. Continuous guided beams of slow and internally cold polar molecules. *Faraday Discuss.*, 142:203–220, 2009.

[56] Nicholas R. Hutzler, Maxwell F. Parsons, Yulia V. Gurevich, Paul W. Hess, Elizabeth Petrik, Ben Spaun, Amar C. Vutha, David DeMille, Gerald Gabrielse, and John M. Doyle. A cryogenic beam of refractory, chemically reactive molecules with expansion cooling. *Phys. Chem. Chem. Phys.*, 13:18976–18985, 2011.

[57] D. Patterson. *Buffer Gas Cooled Beams and Cold Molecular Collisions.* PhD thesis, Harvard University, Cambridge, MA, USA, March 2010.

[58] R. Krems, B. Friedrich, and W. C. Stwalley. *Cold Molecules: Theory, Experiment, Applications.* CRC Press, 2009.

[59] N. E. Bulleid, S. M. Skoff, R. J. Hendricks, B. E. Sauer, E. A. Hinds, and M. R. Tarbutt. Characterization of a cryogenic beam source for atoms and molecules. *Phys. Chem. Chem. Phys.*, 15:12299–12307, 2013.

[60] J. P. Toennies and K. Winkelmann. Theoretical studies of highly expanded free jets: influence of quantum effects and a realistic intermolecular potential. *J. Chem. Phys.*, 66(9):3965–3979, May 1977.

[61] C. H. Townes and A. L. Schawlow. *Microwave Spectroscopy*. Dover Publications, New York, 1975.

[62] James E. Wollrab. *Rotational Spectra and Molecular Structure*. Physical Chemistry. A Series of Monographs. Bd. 13. Academic Press, New York-London, 1967.

[63] J. van Veldhoven, R. T. Jongma, B. Sartakov, W. A. Bongers, and G. Meijer. Hyperfine structure of nd3. *Physical Review A*, 66(3), 2002.

[64] J. F. Barry, E. S. Shuman, and D. DeMille. A bright, slow cryogenic molecular beam source for free radicals. *Phys. Chem. Chem. Phys.*, 13:18936–18947, 2011.

[65] D. R. Willey, R. L. Crownover, D. N. Bittner, and F. C. De Lucia. Very low temperature spectroscopy: the pressure broadening coefficients for co-he between 4.3 and 1.7 k. *Journal of Chemical Physics*, 89(4):1923–8, 1988.

[66] S. Chervenkov, X. Wu, J. Bayerl, A. Rohlfes, T. Gantner, M. Zeppenfeld, and G. Rempe. Continuous centrifuge decelerator for polar molecules. *Phys. Rev. Lett.*, 112:013001, Jan 2014.

[67] M. Motsch, M. Schenk, L. D. van Buuren, M. Zeppenfeld, P. W. H. Pinkse, and G. Rempe. Internal-state thermometry by depletion spectroscopy in a cold guided beam of formaldehyde. *Phys. Rev. A*, 76:061402(R), 2007.

[68] Benjamin Bertsche and Andreas Osterwalder. State-selective detection of velocity-filtered nd_3 molecules. *Phys. Rev. A*, 82:033418, Sep 2010.

[69] M. Motsch, C. Sommer, M. Zeppenfeld, L. D. van Buuren, P. W. H. Pinkse, and G. Rempe. Collisional effects in the formation of cold guided beams of polar molecules. *New J. Phys.*, 11:055030, May 2009.

[70] M. Motsch. *Cold Guided Beams of Polar Molecules*. PhD thesis, Technische Universität München, Garching bei München, Germany, December 2009.

[71] H C W Beijerinck, R G J M Moonen, and N F Verster. Calibration of a time-of-flight machine for molecular beam studies. *Journal of Physics E: Scientific Instruments*, 7(1):31, 1974.

[72] R. Braun and P. Hess. Optimization of a commercial quadrupole mass spectrometer for time-of-flight measurements of laser desorption. *International Journal of Mass Spectrometry and Ion Processes*, 125(2):229 – 239, 1993.

[73] C. Sommer, M. Motsch, S. Chervenkov, L. D. van Buuren, M. Zeppenfeld, P. W. H. Pinkse, and G. Rempe. Velocity-selected molecular pulses produced by an electric guide. *Phys. Rev. A*, 82(1):013410, Jul 2010.

[74] C. M. Lavelle, C.-Y. Liu, W. Fox, G. Manus, P. M. McChesney, D. J. Salvat, Y. Shin, M. Makela, C. Morris, A. Saunders, A. Couture, and A. R. Young. Ultracold-neutron production in a pulsed-neutron beam line. *Phys. Rev. C*, 82:015502, Jul 2010.

[75] Xing Wu, Thomas Gantner, Manuel Koller, Martin Zeppenfeld, Sotir Chervenkov, and Gerhard Rempe. A cryofuge for collision experiments with cold molecules. *in preparation*, 2017.

[76] R. V. Krems. Cold controlled chemistry. *Phys. Chem. Chem. Phys.*, 10:4079–4092, 2008.

[77] B. K. Stuhl, M. T. Hummon, M Yeo, G Quéméner, J. L. Bohn, and J. Ye. Evaporative cooling of the dipolar hydroxyl radical. *Nature*, 492(7514):396, Dec 2012.

[78] M. H. Anderson, Ensher J. R., M. R. Matthews, C. E. Wieman, and Cornell E. A. Observation of bose-einstein condensation in a dilute atomic vapor. *Science*, 269:198–201, 1995.

[79] G. Pupillo, A. Micheli, M. Boninsegni, I. Lesanovsky, and P. Zoller. Strongly correlated gases of rydberg-dressed atoms: Quantum and classical dynamics. *Phys. Rev. Lett.*, 104:223002, Jun 2010.

[80] Y. O. Dudin and A. Kuzmich. Strongly interacting rydberg excitations of a cold atomic gas. *Science*, 336(6083):887–889, 2012.

[81] Alpha Gaetan, Yevhen Miroshnychenko, Tatjana Wilk, Amodsen Chotia, Matthieu Viteau, Daniel Comparat, Pierre Pillet, Antoine Browaeys, and Philippe Grangier. Observation of collective excitation of two individual atoms in the rydberg blockade regime. *Nature Physics*, 5(2):115–118, 2009.

[82] E. Urban, T. A. Johnson, T. Henage, L. Isenhower, D. D. Yavuz, T. G. Walker, and M. Saffman. Observation of rydberg blockade between two atoms. *Nature Physics*, 5(2):110–114, 2009.

[83] M. D. Lukin, M. Fleischhauer, R. Cote, L. M. Duan, D. Jaksch, J. I. Cirac, and P. Zoller. Dipole blockade and quantum information processing in mesoscopic atomic ensembles. *Phys. Rev. Lett.*, 87:037901, Jun 2001.

[84] M R Tarbutt, B E Sauer, J J Hudson, and E A Hinds. Design for a fountain of ybf molecules to measure the electron's electric dipole moment. *New Journal of Physics*, 15(5):053034, 2013.

List of Publications

- **A cryofuge for collision experiments with cold molecules**
  X. Wu, T. Gantner, M. Koller, M. Zeppenfeld, S. Chervenkov, and G. Rempe.
  in preparation, (2017).

- **An experimental toolbox for the generation of cold and ultracold polar molecules**
  M. Zeppenfeld, T. Gantner, R. Glöckner, M. Ibrügger, M. Koller, A. Prehn, X. Wu, S. Chervenkov, and G. Rempe.
  Journal of Physics: Conference Series **793** 012035 (2017).

- **Thermometry of guided molecular beams from a cryogenic buffer-gas cell**
  X. Wu, T. Gantner, M. Zeppenfeld, S. Chervenkov, and G. Rempe.
  ChemPhysChem **17** (22), 3631-3640 (2016).

- **Continuous centrifuge decelerator for polar molecules**
  S. Chervenkov, X. Wu, J. Bayerl, A. Rohlfes, T. Gantner, M. Zeppenfeld, and G. Rempe.
  Phys. Rev. Lett. **112**, 013001 (2014).

Danksagung

I would like to thank everyone who has supported me along the way. Without their helps, certainly I would not be able to successfully complete this thesis.

First of all, I would like to thank my supervisor Prof. Dr. Gerhard Rempe for having offered me the opportunity of trying out the *centrifuge* deceleration of polar molecules. I was fascinated by this idea the first time I heard it before joining the group, even though there existed back then almost nothing more than just the idea. Gerhard has provided me with all sorts of support since my first month here. He has also enabled a great working atmosphere, which has allowed us to eventually build up the centrifuge decelerator and to successfully demonstrate its extraordinary performance. Gerhard's many questions out of his curiosity have also inspired me to think deeper into science, which I believe will benefit myself for years to come.

Certainly, I would like to thank Dr. Sotir Chervenkov for his helps and guidance all these years. He has not only been very patient in discussions, but also kept an amazingly neat archive of what have happened on almost a daily basis. It ranges from all the steps he worked out in molecular theory, to the crazy thoughts we came up with in the lab, and to the content of each group meeting.

I would also like to thank Dr. Martin Zeppenfeld for his new ideas every second afternoon. More importantly, I am very grateful for having learnt from him on many different topics, ranging from how to give a clear presentation to how to tackle unfamiliar problems. He was able to make me feel the methodology of doing research simply through everyday discussions.

I am also very grateful to Dr. Christian Sommer and Dr. Laurens van Buuren, from whom I inherited the cryogenic source. They have provided me with many helps during my first one or two years in the group, including chill-out after work every now and then.

For the current members in the *Cryofuge* project, I would like to first thank Thomas Gantner who has been working with me for the last several years. Without his effort in the lab, we would not be able to perform many of these measurements described here, and a lot more which have not yet been summarized in this thesis. I also appreciate the time we spent together after work, from football match to hiking in the Alps. I would also like to thank Manuel Koller for the fruitful discussion and work in the lab during the last one year.

For the ex-members of the *Cryofuge* project as well as members of the whole cold molecule team Andreas Rohlfes, Alexander Prehn, Martin Ibrügger, Rosa Glöckner, Barbara Englert, Michael Motsch, Ferdinand Jarisch, Erich Dobler, Markus Krottenmüller, and Michael Wismer, I would like to thank all of you for you supports in the lab and for the great atmosphere created in the group.

For our retired and current technicians Josef Bayerl, Franz Denk, Helmuth Stehbeck, Thomas Wiesmeier, Tobias Urban, Florian Furchtsam, and Johannes Siegl, I